Design and Development of closed-loop AO system for 2-m class telescope at IIA

A Thesis

Submitted for the Degree of

Doctor of Philosophy (Technology)

Submitted by

SATYA RANJAN BEHERA

Department of Applied Optics & Photonics

University College of Technology

University of Calcutta

Acknowledgements

I would like to express my sincere gratitude to my thesis supervisor Prof. B. Raghavendra Prasad for introducing me to the field of adaptive optics, which has proven its place in the field of imaging in various applications. I would like to thank the Director, IIA for his support. I am thankful to the administrative staff of IIA for their constant support and making my stay in IIA comfortable. I thank the librarian and the library staff for extending their help when approached. I am grateful to the Head of the Department of Applied Optics and Photonics, University of Calcutta for his support. I would like to express my appreciation to administrative staff of University of Calcutta for their assistance during my visits to Calcutta.

I am grateful to Board of Graduate Studies, IIA for supporting me to attend a number of national conferences and giving me an opportunity to present my work and interact with many researchers in my field. I thank Dr. B. C. Bhatt and Dr. D. K. Sahu for making my stay memorable at CREST campus of IIA. I thank to other staffs of CREST campus who always supported during my stay.

I express my sincere thanks to my colleague Mr. Avinash Surendran for giving me moral strength and support during my PhD career. I would also like to thank Mr. N. Rajkumar, Mr. N.V Suresh and Mr. Madhur Juneja for helping me in laboratory experimens.

Finally, none of this would have been possible if it wasn't for the inspiration, vision and greatness of my family members.

Abstract

Adaptive Optics (AO) is a real time wave-front correction technique, through which the light coming from the stars can be corrected for the effects of atmospheric turbulence. This enables the ground based telescope to reach diffraction limited image quality and thereby improving its resolution. The main objective of the work is to develop a laboratory model of closed loop Adaptive Optics system for Indian Astronomical Observatory (IAO) Hanle telescope (having a primary aperture diameter of 2m). The mean value of Fried Parameter at IAO Hanle is 15 cm at a wavelength 500 nm. So, $\frac{D}{r_0}$ value of Hanle telescope is 12. In order to achieve the same value in the laboratory with deformable mirror actuator size of 450 μm the beam size be 5 mm approximately. Strehl ratio is another important parameter defined as ratio of measured point spread function (PSF) to theoretical PSF. It is calculated theoretically at 1.1μm. Since AO system design in IR band gives better Strehl ratio compared to visible band.

In order to understand the performance of Adaptive Optics system, a laboratory model has been proposed which is scaled down version of 2-m class. Components including Shack-Hartmann wave-front sensor (SHWFS), continues membrane deformable mirror (CDM) have been studied experimentally. A control algorithm converts the local slope measurements in the wave-front sensor caused by random phases into command values that can be addressed by the correcting element. This step called wave-front reconstruction is considered as the heart of an AO system since it

controls the accuracy of wave-front sensing. An algorithm for wave-front reconstruction is developed by using Fried's geometry with vector multiplication method and it is tested for various light intensity levels for different Zernike polynomials. sCMOS which is a low noise and high speed camera, is calibrated. For a CDM, slope influence function is developed for assessment of CDM performance by giving a specific voltage to an actuator and bias voltages to all other actuators. The performance of slope influence function is tested for various higher order Zernike polynomials. The purpose of the real-time closed-loop control system is to interpret the WFS data to produce a set of meaningful control signals to position elements of the WFC, usually by reconstructing the wave-front. The wave-front is measured and data electronically processed by the RTCS, which calculates and generates signals used to apply the phase conjugate to the corrector.

List of Tables

List of Figures

Table of Contents

Chapter 1

INTRODUCTION

1.1 MOTIVATION

Adaptive optics (AO) is a technology used to compensate in real time the aberrations that occur when light propagates through an inhomogeneous medium. Currently its most important applications are in astronomy and in military applications [1], although also medical uses are becoming more common [2].

Designing and building an AO system requires expertise from many fields besides astronomy optics, electrical and mechanical engineering, computer science and control theory. The idea of AO was first mentioned in 1950s [3]. However, it was not until 1970s before sufficiently sophisticated technologies became available at military fields [4]. The first successful AO systems were applied in the major astronomical telescopes at the beginning of the 1990s [5].

The celestial light coming from a very distant object forms a plane wave-front. When it propagates through the atmosphere, differences in the refractive index of air cause the shape of the wave-front to change. The device measuring these deformations is called a wave-front sensor (WFS).

Currently the main AO solutions are based on a closed-loop operation. The celestial light is reflected from a deformable mirror (DM). One part of this reflected light is directed to a scientific camera and other part to the WFS. The sensor measures the wave-front distortions and the measurements are fed to a control system that computes new commands to be sent to the DM. The DM then adapts to further reduce the residual distortions. This process thus iteratively compensates the atmospheric effects.

In order to study these problems, a laboratory model has been proposed which is scaled down version of 2-m class in AO Lab of CREST campus of Indian Institute of Astrophysics, Bangalore. This thesis focuses on the development of closed loop adaptive optics system techniques to reduce structural disturbances.

1.2 THESIS OBJECTIVES

The focus of this thesis is to investigate the adaptive optics control techniques and demonstrate them experimentally. The ultimate goal of the experimental portion is to simulate a dynamic disturbance on a deformable mirror and remove the disturbances imparted onto an incoming laser light source by removing aberrations in the wave-front using deformable mirrors and a wave-front sensor.

1.3 THESIS OVERVIEW

Chapter 2 provides a background on adaptive optics and adaptive optics controls. An adaptive optics system is described using a discrete time state space model.

Chapter 3 presents the experimental setup and the equipment used including deformable mirrors and wave-front sensors. The experimental layout is explained in detail.

Chapter 4 discusses wave-front estimation and the principles of a Shack Hartmann wave-front sensor. This chapter investigates wave-front reconstruction techniques that are required for wave-front control. This includes both indirect wave-front representation and direct wave-front representation using modal and zonal wave-front estimation techniques.

Chapter 5 discusses about wave-front control technique by evaluating Slope influence matrix. Its performance is tested for various Zernike polynomials.

Chapter 6 discusses about atmospheric turbulence by simulating of Kolmogorov turbulence l and using phase plate.

A traditional iterative closed loop feedback control technique is developed using direct wave-front estimation methods is discussed in chapter 7. In this chapter, the AO system theory examines the main components, the wave-front sensor, the wave-front corrector and the controller.

Bibliography

[1] F. Roddier, “Imaging through the atmosphere,” in *Adaptive Optics in Astronomy*, Cambridbe university press, 1999, pp. 9-22.

[2] D. C. Chen, S. M. Jones, D. A. Silva and S. S. Olivier, “High-resolution adaptive optics scanning laser opthalmoscope with dual deformable mirrors,” *Journal of the Optical Society of America,* vol. 24, pp. 1305-1312, May 2007.

[3] H. W. Babcock, “The possibility of compensating astronomical seeing,” *Astron. Soc. Pac.,* vol. 65, pp. 229-234, Oct 1953.

[4] B. L. Ellerbroek and G. Cochran, “Wave optics propagation code for multiconjugate adaptive optics,” in *Proc. SPIE,* 104-120, Feb. 2002.

[5] G. Rousset and N. N. Hubin, “Advancement in Adaptive Optics,” in *Society of Photo-Optical Instrumentation Engineerig (SPIE) conference*, Oct 2004.

Chapter 2

INTRODUCTION

The basics of optical telescopes and principles behind imaging with a telescope are discussed. A brief introduction to Kolmogorov turbulence and its various parameters to measure turbulence is described. Astronomical imaging in presence of turbulence and different methods to eliminate the effects of atmospheric turbulence is discussed. An introduction to Adaptive Optics is presented here with all of its components are briefly explained.

2.1 Optical Telescopes

Optical telescopes became the most important instrument in astronomy during the 17^{th} century [1] [2], when Galileo started using them for astronomical observations. Telescopes collect light from far away objects using lenses and mirrors. The light is focused onto a small area. The light is magnified with an eyepiece to see the object [3]. There are two types of optical telescopes: Refractor telescopes and Reflector telescopes. Refractor telescopes use lenses to focus objects while reflector telescopes use lenses and mirrors to focus objects.

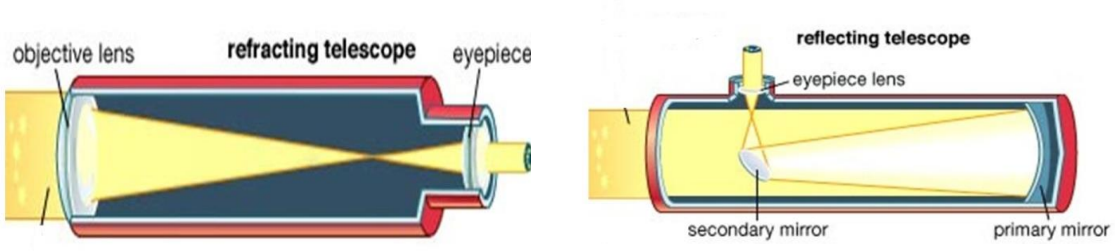

(a) (b)

Figure 2. 1: (a) Refracting type telescope, (b) Reflecting type telescope

Generally, refracting telescopes are very long with heavy lenses. The biggest problem with refracting telescopes is chromatic aberration. Chromatic aberration occurs because different colours of light focus at different points [4]. Unlike the refractor telescope used by Galileo, most modern telescopes are reflector type. Reflecting telescopes use large mirrors to focus light. Modern telescopes generally contain a number of scientific instruments, each one giving the telescope increased scientific capability [5]. Instruments are placed at various focal points. Telescopes differ from each other in how the focused light reflected by the primary is collected. The focal point of the primary mirror is called prime focus [6]. It is commonly used for imaging of very faint objects and for wide-field spectroscopy. Four types of focal points of the reflecting telescopes are shown in Figure 2.2. They are (a) Prime focus, (b) Newtonian focus, (c) Cassegrain focus and (d) Nasmyth focus.

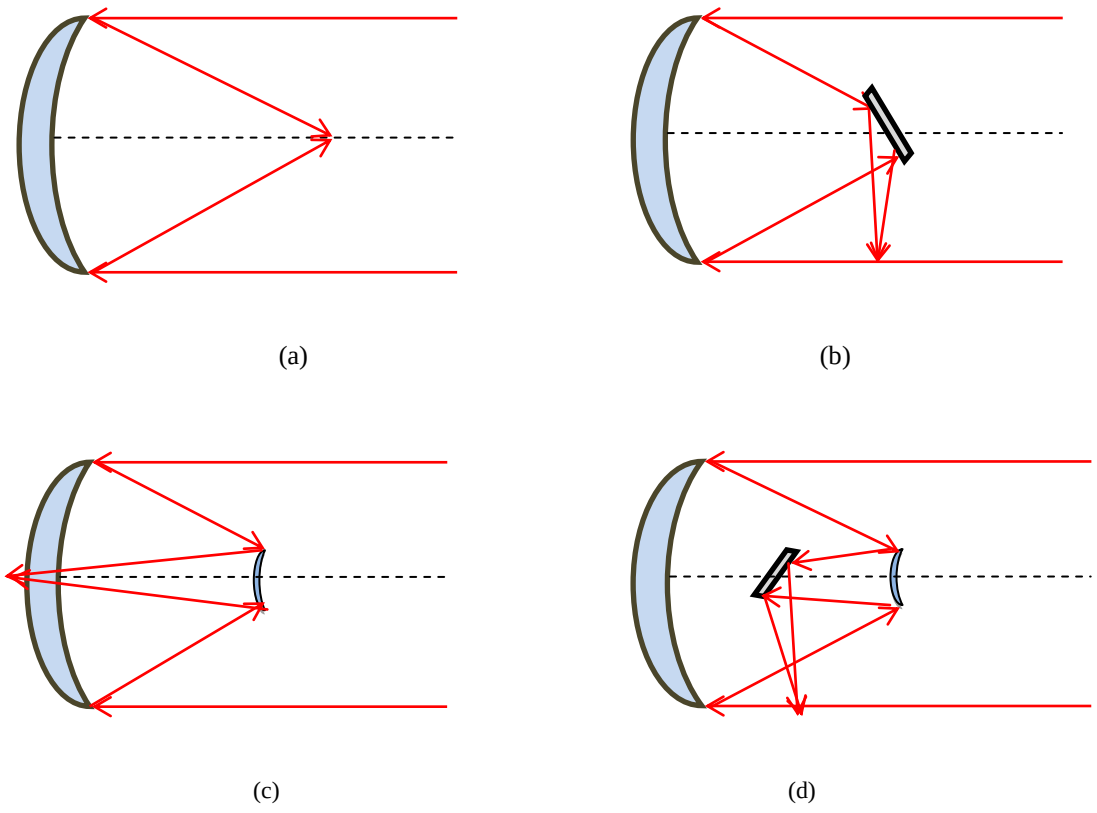

Figure 2. 2: Different types of focal points of reflecting telescopes. (a) Prime focus, (b) Newtonian focus, (c) Cassegrain focus, (d) Nasmyth focus

For large telescopes the most common focus is the Cassegrain. The focal plane is located below the parabolic primary mirror, which provides a convenient place for attaching and changing multiple instruments. Another popular focus is called Nasmyth. The beam, after being reflected by the secondary, is bent at 90° with a flat mirror to converge to a point on the side of the primary. Telescopes commonly have two Nasmyth platforms, one either side of the primary mirror [7].

Another important element in the characterisation of reflecting telescopes is their mounting. There are two main types of telescope mounting: equatorial and alt-azimuthal. The alt-azimuthal mounting contains two axes of rotation (vertical and horizontal); since the introduction of computerised telescope control and auto guider systems it has been the preferred choice of mounting for large telescopes [8]. Tracking a star requires a combination of the two rotations; thus tracking requires constant changes to the velocity and acceleration of the axis's motors. Due to technological advancement its become easy for building 8-10 m telescope now a days. The next generation telescopes are under way to collect more light to study distant universe.

2.2 Imaging with telescope

The image of a point source (star) in an ideal telescope without atmosphere is shaped by the diffraction and is described by an Airy function [9]. The size of this pattern determines the angular resolution of optical system [10].

$$P_0(u) = \frac{1}{\left(1-\varepsilon^2\right)^2}\left[\frac{2J_1(u)}{u} - \varepsilon^2\frac{2J_1(\varepsilon u)}{\varepsilon u}\right] \tag{1}$$

Where, u = is a dimensionless distance from the optical axis in the focal plane and is related to the angular radius θ (as measured from the primary aperture) and the diameter D of the primary aperture as follows:

$$u = \frac{\pi D \theta}{\lambda} \tag{2}$$

$P_0(u)$ is the light intensity in the focal plane, called point spread function (PSF) of a telescope, as a function of angular coordinate θ; PSF is the impulse response of a imaging system to a point source .

- ε is the fractional radius of central obstruction of the primary aperture .
- λ is the wavelength of light
- D is the diameter of the telescope aperture
- J_1 is first order Bessel function

When there is no central obstruction i.e. ε is zero, PSF reduces to

$$P_0(u) = \left[\frac{2J_1(u)}{u} \right]^2 \tag{3}$$

The image at the telescope focus is not a point, but a circular diffraction pattern with a central bright spot containing approximately 84% of the light, known as the Airy disc. The first dark ring is at an angular distance of 1.22 $\frac{\lambda}{D}$ from the centre. The rest of the light will be in the concentric rings surrounding the spot. This is often taken as a measure of resolution in an ideal telescope. The resolution of any imaging system is limited by the quality of optics within the system. Even with 'perfect' optics however (if only there was such a thing!), there is an upper limit on resolution for any imaging system due to intrinsic diffraction effects. In this diffraction limited regime, the highest resolution obtainable i.e. the angular separation θ (in radians), is given by the *Rayleigh criterion* [11].

$$\theta = 1.22 \frac{\lambda}{D} \tag{4}$$

Where λ is the optical wavelength and *D* is the diameter of the aperture in the system (for telescopes, the diameter of the primary mirror). To obtain higher resolution images of a scientific source, this means either a shorter wavelength of light or a telescope with a larger diameter must be used. Figure 2.3 shows simulated Airy disc.

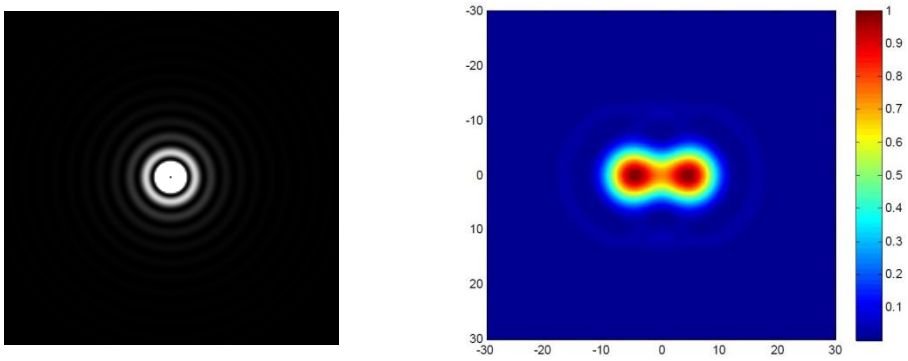

Figure 2. 3: (a) Example simulated images of a diffraction limited system (for ideal telescope Airy pattern), (b) Rayleigh criterion for two point source (simulated)

The theoretical angular resolution of the telescope is limited by the size of the Airy disc. It is only possible to resolve two point sources if their Airy discs are sufficiently separated to be seen as distinct. The Rayleigh Criterion states that for two sources to be distinguishable, the central maximum of the diffraction pattern of one source coincides with the first minimum of the other. When the angular resolution of a telescope, at a given wavelength, is determined by the radius of the Airy disc, it is said to be "diffraction-limited" [12].

Before looking at atmospheric turbulence in section 2.3, for modern large telescopes, angular resolution at optical and near infra-red wavelengths is almost always limited by the broadening of stellar images by atmospheric turbulence, commonly referred to as the *Seeing***.**

As the parallel plane WF from a distant object enters our atmosphere and passes through different layers, phase changes due to changing refraction index, differential atmospheric refraction and diffraction can lead to broadening the apparent angular size

of the source. It is possible to define a seeing disc as the angular size of this broadened stellar image. For a point source, the time-integrated angular distribution of light intensity is called the *seeing profile* [13]**.**

The diameter of the seeing disc as can then be defined as the full width at the half maximum (FWHM) of the Gaussian distribution, obtaining: Figure 2.4 shows the Gaussian seeing distribution.

$$\alpha = 1.665\,\sigma \tag{5}$$

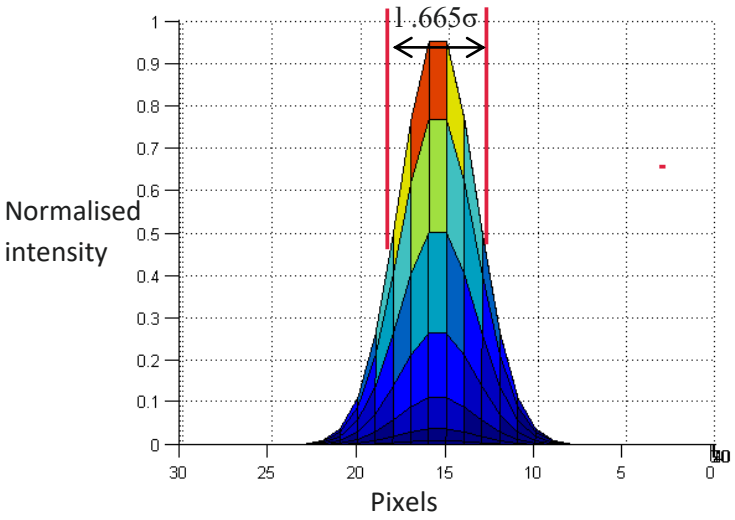

Figure 2. 4: Gaussian seeing distribution (PSF)

The FWHM is often used in determining the quality of the seeing and it may be used as a measure of correction in an AOS.

If an astronomical object is denoted as *O(u)* then Image *I(u)* of an can be considered as a multitude of points, each point spread into an Airy function. This is written as convolution of object with telescope PSF.

$$I(u) = \int O(u)P(u-v)\,dv \tag{6}$$

In spatial frequency domain, it is expressed as,

$$I(f) = O(f) * P(f) \tag{7}$$

Here, f is the spatial frequency. $P(f)$ is called Optical Transfer function (OTF). It is the true measure of resolution that a system is capable. In other words how effectively the spatial frequencies in the object space are transferred to the image space through an optical system. OTF and PSF are related via Fourier transform.

$$OTF \Leftrightarrow PSF$$

$$OTF_{effective} = OTF_{telescope} * OTF_{atmosphere} \tag{8}$$

Strehl Ratio : The *Strehl Ratio* (*S*), also known as the normalised intensity, is the ratio between the intensity on-axis of an aberrated point spread function (PSF) and the intensity on-axis of an unaberrated (diffraction limited) PSF. The *S* is a measurement used in AO to quantify the quality of the beam:

$$S = \frac{P(0)}{P_0(0)} \tag{9}$$

The higher is Strehl ratio, the better is resolution. Diffraction-limited image is the best, hence $S \leq 1$ always. The Strehl ratio lies between 0 and 1, with values greater than 0.8 corresponding to essentially diffraction-limited images.

Encircled energy : By definition, the integral of PSF is equal to 1. The PSF integral over the circle of radius is called encircle energy [14].

For astronomical imaging, OTF is $|I(f)| \leq 1$ always. For any optical system $|I(f)| = 0$ for $|f| \geq f_C$, Where $f_C = \frac{D}{\lambda}$ is called cut-off frequency.

2.3 Atmospheric turbulence

Light from an astronomical object travels for undisturbed, until encounters the atmosphere of the earth. It has a perfect plane wave-front at the outer layer of atmosphere. Light travels a little more slowly in air than it does in a vacuum, with the change in velocity related to the density of the air. Since the air in the atmosphere is turbulent and moves randomly in all directions, the density of air called as refractive index of atmosphere is unevenly distributed. The refractive index of the turbulent atmosphere will introduce time and space varying optical path differences on the plane wave-front [15]. The refractive index of the atmosphere is dependent upon temperature, pressure and density, all of which fluctuate on scales ranging from the largest eddy called "outer scale" (above which isotropic behaviour is violated) to small pockets of air called "inner scale" (below which energy is dissipated as heat). When an image of an object taken with a short exposure time is taken through a telescope [16], the resulting images are both blurred and randomly displaced. When seen with the naked eye, the stars appear to twinkle. This distortion affects the ability to "resolve", or distinguish, two objects close to each other.

In the absence of turbulence, the resolution of an optical system is inversely proportional to the diameter of the aperture: the smaller the telescope, the coarser the resolution. When viewing through the atmosphere, there is an additional limit to the resolution that can be attained due to the turbulence. Fried's parameter r_o describes strength of the turbulence in terms of the diameter of the telescope that gives the same limiting resolution as an image taken with a long exposure time through the atmosphere. The value of r_o is of the order of 10 to 20 cm at a good viewing site. The resolution of the images is limited by the atmosphere rather by the optics of the telescope. Hence at a good astronomical viewing site, the largest existing telescope, with a primary mirror 10 meters in diameter, has a similar resolution to that of a good backyard telescope. Overcoming the effects of turbulence presents a problem to astronomers, who wish to obtain the sharpest possible images. It is even more vital in the design of the next generation of telescopes, like the 30-meter California Extremely

Large Telescope (TMT) and the ESO's 100 metre Overwhelmingly Large Telescope [17].

2.3.1 Kolmogorov turbulence

Atmospheric turbulence is a random process. Kolmogorov used structure functions to describe non-stationery random functions associated with turbulence and its related parameters of temperature, humidity and velocity [18]. Since these aberrations are random, they can only be described statistically, using statistical estimates such as variances, covariance or correlation function. However, for pure Kolmogorov turbulence with an infinite outer scale, the correlation function tends towards infinity as the separation between two points goes to zero. For this reason structure function has been used. Kolmogorov model assumes that energy injected into turbulent medium on large spatial scales (outer scale, L_0) and forms eddies [19]. These large eddies cascade the energy into small scale eddies until it become small enough (small scale, l_0) that the energy is dissipated by the viscous properties of the medium. The inertial range between inner and outer scales Kolmogorov predicted a power law distribution of the turbulent power with spatial frequency.

Air refractive index fluctuations : Fluctuations in the air refractive index are essentially proportional to fluctuations in the air temperature [20]. These are found at the interface between different air layers. Wind shears produce turbulence which mixes layers at different temperature, and therefore produces temperature inhomogeneities. The statistics of refractive index inhomogeneities follows that of temperature inhomogeneities, which are governed by the Kolmogorov law of turbulence. We are not interested in the absolute value of the refractive index, but mainly in the difference between its value $\eta(\boldsymbol{r})$ at a point $\boldsymbol{r}$, and its value $\eta(\boldsymbol{r} + \rho)$ at a nearby point some distance $\rho = |\boldsymbol{\rho}|$ apart. Vectors $\boldsymbol{r}$ and $\boldsymbol{\rho}$ represent three- dimensional positions and separations. The variance of the difference between the two values of the refractive index is given by

$$D_n(\rho) = \left\langle \left[\eta(r+\rho) - \eta(r)\right]^2 \right\rangle$$
$$D_n(\rho) = C_n^2 \rho^{2/3} \tag{10}$$

Where the brackets < > represent an ensemble average. $D_n(\rho)$ is called the index structure function. To a first approximation, it depends only upon the separation ρ but not the position *r*, that is the random process is considered as homogeneous (at least locally). Moreover, it depends only on the modulus of the vector ***r*** independently of its direction, that is the process is isotropic. The quantity C_n^2 is called the index structure coefficient. It is a measure of the local amount of inhomogeneity. Its integral along the light propagation path gives the total amount of wave-front degradation or 'seeing'.

Equation (10) statistically describes the spatial distribution of the inhomogeneity at a given time t. It is also need to be known how fast the index fluctuates with time, at a fixed point r along the line of sight. The temporal evolution can be similarly described by a temporal structure function defined as the variance of the difference between the index at time t and the index at a later time t + τ.

$$D_n(\tau) = \left\langle \left[\eta(r,t) - \eta(r,t+\tau)\right]^2 \right\rangle \tag{11}$$

If *v* is the wind velocity, then

$$\eta(r,t+\tau) = \eta(r - v\tau, t) \tag{12}$$

This approximation is called the Taylor approximation. Putting Equation (12) into Equation (11) gives the following expression for the temporal structure function

$$D_n(\tau) = \left\langle \left[\eta(r,t) - \eta(r - v\tau, t)\right]^2 \right\rangle \tag{13}$$

$$D_n(\tau) = C_n^2 \left|v\tau\right|^{2/3} \tag{14}$$

Hence, the temporal structure function is simply obtained by substituting $v\tau$ for ρ in the spatial structure function.

Wave-front phase distortions : Waves are best described by means of a complex number ψ, called the wave complex amplitude. It is defined as

$$\psi = A\exp(i\phi) \tag{16}$$

where A and ϕ are real numbers representing respectively the amplitude and the phase of the field fluctuation. A surface over which ϕ takes the same value is called a wave-front surface. Before entering the atmosphere, light from very far away sources such as stars forms plane waves (flat wave-front surfaces). However, inside the atmosphere the speed of light will vary as the inverse of the refractive index. Light propagating through regions of high index will be delayed compared to light propagating through other regions. The resulting wave-front surface is no longer flat but corrugated. The deformation of the wave-front surface is given by the optical path fluctuation [21].

$$\delta = \int n(z) \tag{17}$$

where *n(z)* is the refractive index fluctuation along the beam. It is important to note that, since *n(z)* is fairly independent of wavelength, the deformation of the wave-front surface (generally expressed in microns, or nanometres) is also a wavelength independent quantity. Hence, it can be compensated at all wavelengths. The wave-front phase fluctuation is related to the wave-front surface deformation by the following relation:

$$\phi = k\int n(z)dz \tag{18}$$

where k is the wave number. It varies as the inverse of the wavelength λ. $k = \frac{2\pi}{\lambda}$

Hence, the wave-front phase fluctuation is not achromatic. At long wavelengths, fluctuations are smaller. The difference between the phase $\phi(x)$ at a point x on the telescope entrance aperture and the phase

$\phi(x+r)$ at a nearby point a distance r apart. The variance of the difference is the structure function of the phase

$$D_{\phi}(r) = \left\langle \left[\phi(x+r) - \phi(x)\right]^2 \right\rangle \tag{19}$$

Where $\phi(x) = \frac{2\pi}{\lambda} l(x)$ phase of optical wave. $l(x)$ optical path length.

Tatarski showed the three dimensional power spectrums, $\phi_n(k)$ of the refractive index variations is

$$\phi_n(k) = 0.033 C_n^2 k^{-11/3} \tag{20}$$

Where k is wave number

The outer scale is an important parameter in turbulence statistics and its range of values are much debated in astronomical databases. The standard spectrum of Kolmogorov turbulence is usually written with infinite outer scale and the effect of infinite outer scales is to reduce the lower spatial frequency contributions. This effect is more pronounced as the telescope diameter exceeds the size of outer scale. Given that the outer scale is usually 10m to 100m, many of the future extremely large telescopes will have larger diameter than the outer scale. This power spectrum is only valid within the inertial range between the inner and outer scale as it tends to infinity at larger spatial separations. There are other modified models for the atmospheric power spectral density, like the Tatarski, Von Karman, and modified Von Karman which are commonly used [22]. These models are much more sophisticated and include various inner-scale and outer-scale factors that improve the agreement between theory and experimental measurements. So in order to accommodate the

finite inner and outer scales, the Kolmogorov power spectrum [23] [24] was modified by Von Karman power spectrum which is given by.

$$\phi_N^k = 0.023C_n^2(k^2 + k_0^2)^{-11/6}\exp(-\frac{k^2}{k_i^2}) \tag{21}$$

Where $k_0 = \frac{2\pi}{L_0}$, $k_i = \frac{2\pi}{l_0}$

It can be expressed in another form with Fried's parameter r_0

$$\phi_N^k = 0.023(\frac{D}{r_0})^{5/3}(k^2 + k_0^2)^{-11/6}\exp(-\frac{k^2}{k_i^2}) \tag{22}$$

For infinite outer scale k_0 and zero inner scale k_i above equation reduces to

$$\phi_N^k = 0.023(\frac{D}{r_0})^{5/3}(k)^{-11/3} \tag{23}$$

The Power spectral density (PSD) and phase screen *f(r)* are related as

$$\phi_n(k) = \left|\int_{\infty}^{\infty} f(r)e^{-ikr}dr\right|^2 \tag{24}$$

From the above equation phase screen is given by

$$f(r) = \int_{\infty}^{\infty}\sqrt{\phi_n(k)}e^{ikr}dk \tag{25}$$

Where, *f(r)* is 2D - Kolmogorov phase screen, can be obtained from inverse Fourier Transform of square root of Von Karman power spectrum of turbulent atmosphere [25] .

2.3.2 Imaging with atmospheric turbulence

The phase distortions that arrive at the telescope entrance are the cumulative effect of refractive index variations through a vertical through a vertical path in the atmosphere. The refractive index structure function is given by from Equation 26 [26].

$$D_n(r) = C_n^2(h) r^{2/3} \tag{26}$$

The Kolmogorov model of turbulence distortions prescribes the specific form the phase structure function

$$D_n(r) = 6.88\left(\frac{r}{r_0}\right)^{5/3} \tag{27}$$

r_0 called Fried's parameter is given by Equation 25

$$r_0 = 0.185\lambda^{6/5}\cos(\xi)^{3/5}(C_N^2 dh)^{(-3/5)} \tag{28}$$

Where ζ is the zenith angle and λ is wavelength of observation.

Atmospheric turbulence changes temporally and spatially. For long exposure times, averaged PSF we observe with imaging object [27].

$$OTF_{effective} = OTF_{telescope} * OTF_{atmosphere} \tag{29}$$

The atmospheric Optical Transfer Function (OTF) is related to the statistics of the atmospheric phase aberrations

$$OTF(f) = \exp -(0.5 D_{\phi}(\lambda f)) \tag{30}$$

Now we put this model into long-exposure atmospheric OTF, and we get in the form:

$$OTF_{atmosphere}(f) = \exp\left[-3.44\left(\frac{\lambda f}{r_0}\right)^{5/3} \right] \tag{31}$$

From Eq.(27), one can obtain long exposure PSF of atmosphere by taking the Fourier transform of OTF .The FWHM of the atmospheric PSF called as seeing, it is related to Fried's parameter r_0 Seeing =$0.98\frac{\lambda}{r_0}$

Hence the Fried's parameter with wavelength is given by [28]

$$r(\lambda) = \left(\frac{\lambda}{\lambda_0}\right)^{6/5} r_0 \tag{32}$$

2.3.3 Astronomical imaging

Consider the task of imaging a distant star, which is sufficiently far away that it appears to be a point. A wave-front is the surface describing the position of the wave at a fixed time after leaving the source. The wave-fronts from a point source are circular, because the emitted light travels at the same speed in all directions. After a long time, the radius of the wave-fronts is so great that the wave-fronts are essentially planar over the aperture of a telescope, as shown in Figure 5. The planar wave- fronts arrive at the earth's atmosphere, where some light paths are slowed more than others, so the wave-front becomes aberrated. Parallel light rays no longer travel in parallel lines. When these aberrated wave-fronts are focused onto the focal plane of a telescope, the images are blurred. Figure 2.5 shows the imaging of a telescope in an ideal condition and in presence of turbulence.

A secondary effect of atmospheric turbulence is that the light intensity over a small area of the aperture varies randomly. This is manifestation of a phenomenon called

scintillation, and it is why stars appear to twinkle when viewed with the naked eye [29].

2.3.4 Solutions

Currently, there are four solutions to eliminate or mitigate the effects of atmospheric turbulence: space telescopes, adaptive optics, deconvolution from wave-front sensing and speckle interferometry. The choice is a trade-off between cost and performance, with the solutions [30].

Space Telescopes : The most obvious solution to the problem of atmospheric turbulence is to operate a telescope in space, such as the Hubble Space Telescope run by NASA. The telescope with a 2.4-meter diameter was deployed in 1990 and has taken images with previously unattainable clarity. The 6- metre Next Generation Space Telescope is due to be launched. As well as overcoming the turbulent effects of the atmosphere, space telescopes surmount the inconvenience of rain, clouds and the absorption of certain wavelengths of light, such as the ultra-violet band, by atmospheric gases [31].

The disadvantages of space telescopes are the huge financial cost and the difficulty in making changes to the optical equipment. In addition, the weight of the payload for a space telescope is constrained, limiting the size of the telescope and the scientific equipment. Consequently, telescopes on earth are more numerous, collect more light and can have a superior resolution if the effect of the atmosphere are corrected. While space telescopes are a good tool for astronomy, there is still a place for ground –based telescopes [32].

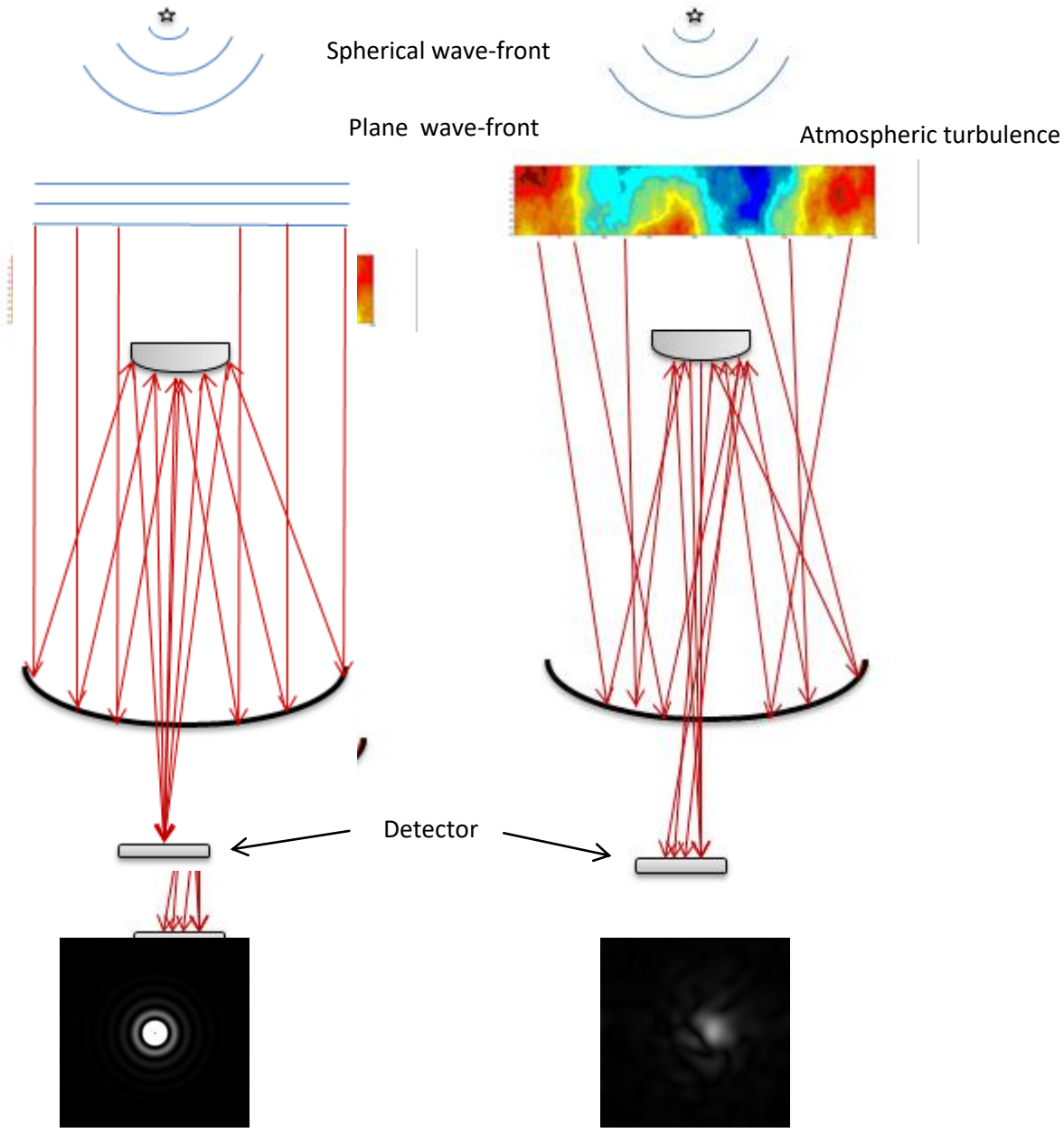

Figure 2. 5: (a) Imaging of a telescope in the absence of turbulence is perfect airy pattern, (b) in the presence of turbulence is speckle pattern.

Speckle interferometry and blind deconvolution : The first techniques to overcome the effects of turbulence relied on computer processing of speckle images. Classical speckle interferometry takes hundreds of images of the astronomical objects and of a nearby bright star. The exposure time is sufficiently short that the atmosphere is effectively "frozen" over that time scale. By processing the images, it is possible to obtain an estimate of the object of a higher resolution than the captured images. A popular post-processing techniques that does not require a reference star takes the triple correlation of the images [33].

Blind deconvolution estimates both the images and the blurring function for each of the captured images. The measured data and additional constraints, such as the statistics of the noise and of the turbulence, and the fact that the intensity of the true image must be positive, are used to obtain the most probable image [34].

Deconvolution from wave– front sensing : An alternative method is to take short-exposure images and the output of a wave-front sensor simultaneously. Wave-front sensors are used to estimate the wave-front aberration at the aperture. The atmosphere acts as a filter on the images. This filtering operation, which is continually changing, is obtained by applying the corresponding inverse filter to each of the blurred images, a process known as deconvolution. The resolution of the corrected images depends on the accuracy of the wave-front estimate [35].

Adaptive optics : This solution to the problem of imaging through turbulence, first suggested by Babcock in 1953 is to cancel the effect of the turbulence by introducing an optical element which performs the inverse operation on the wave front. Very good scientific results have already been obtained using adaptive optics. Figure 2.6 shows images of a binary star (two stars close together). From the image without adaptive optics, it is difficult to say how many stars there are. With adaptive optics, the separation and relative brightness of the two stars can be calculated [36].

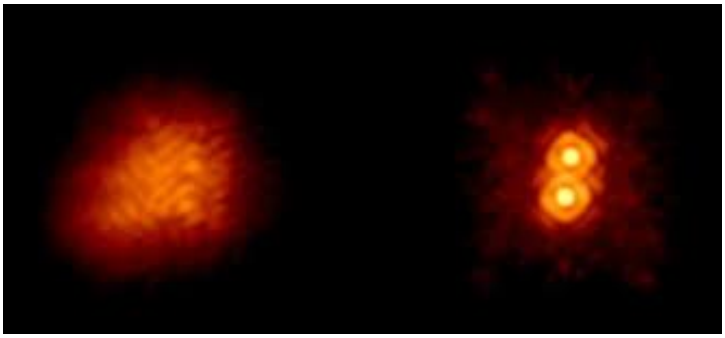

Figure 2. 6: Shows gain of angular resolution by using AO of a binary star

2.4 Adaptive Optics :

A schematic diagram of an adaptive optics system is drawn in Figure 2.7.

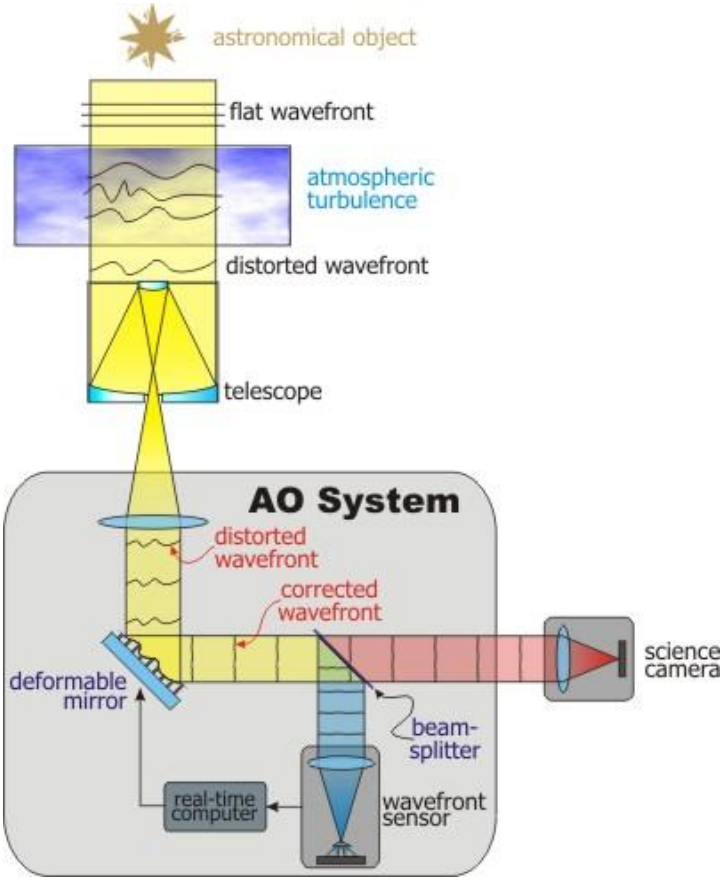

Figure 2. 1: Schematic representation of AO system and its component

The system relies on having a bright guide star available near the object of interest to measure the wave-front aberration. A portion of light received by the telescope is diverted to the wave-front sensor using a beam splitter. The light is usually split according to its wavelength. Some amount of light is used for imaging and rest would be used for wave-front sensor. The difficulty in wave-front sensing is that the wave-front must be estimated indirectly, because it is the intensity of light rather than its phase that interacts with matter. In any case, the frequency of light is of the order of 10^{14} Hertz. So the phase changes too quickly to measure. Hence, the main computational difficulty in an adaptive optics system is to estimate the wave-front.

The indirect wave-front estimate is fed to the corrector, an optical element employed to remove the distortions in the wave-front. The corrector normally a deformable mirror takes the shape of the wave-front. The controller takes the indirect wave-front measurements and deduces the electrical signals required to drive the deformable mirror. The process of driving the deformable mirror from the wave-front sensor measurements must be executed faster than the rate of change of the atmosphere, typically between 100 and 1000 Hz. The applied voltages cause the surface of the mirror to warp like a potato chip.

The natural stars need to be positioned close to the celestial patch of interest and to be sufficiently bright. But, natural guide star can't found everywhere on the sky and it should be sufficient luminosity for AO systems. Hence, to eliminate the need for a bright star, AO systems are increasingly being equipped with laser guide stars. Laser guide stars are the reflection in the atmosphere of powerful lasers pointed in the direction of the astronomical objects. There are difficulties associated with laser guide stars. Because of their relatively low height, the path through the turbulence of light from a laser guide star differs from that of the object of interest. In addition, the laser guide star's rays are also bent on the upward trajectory, making it difficult to determine what the apparent motion of the laser guide star.

Because AO systems are not perfect, the wave-front is only partially compensated. The degree of compensation depends on the accuracy of the wave-front estimate, the spacing of the actuators in the mirror and many other factors. It is possible to improve images obtained using AO further by computer post processing. Post processing is also useful to evaluate the degree of correction afforded by the adaptive optics system [37].

AO systems are closed-loop systems, which means that the wave-front is sensed after correction. Post processing methods, on the other hand are open loop, because the uncorrected wave-front is estimated. There are several advantages to having closed-loop operation. In closed-loop, if the wave-front sensing model is non-linear or not accurately known, a linear approximation to the model will still drive the correctors in the right direction and the estimate will converge on the true wave-front. Furthermore, some wave-front sensors permit the sensitivity of the wave-front measurement to be adjusted and this can be exploited in closed loop by increasing the sensitivity of the sensor when the wave-front is well compensated.

2.4.1 Adaptive Optics components

Conventionally, most astronomical adaptive optics systems (AO) contain the required three key components, the wave-front sensors (WFS), the wave-front corrector (WFC) and the real time control system (RTCS).

2.4.1.1 Wave-front Sensor: The WFS needs to sense the wave-front with sufficient spatial resolution and speed for the WFC to apply a real-time correction to compensate for wave-front aberrations. With today's technological limitations, no detector is capable of directly measuring the wave-front phase at optical wavelengths due to the temporal frequencies required. The optical detectors that are available are used to measure the intensity of light and indirect methods are used to determine the phase. There are two ways of deriving the phase of a wave-front from its intensity distribution both at the focal and pupil planes. Focal plane techniques eliminate the need for phase reconstruction, as it allows direct access to the wave-front phase from the intensity distribution. Pupil plane techniques are either based on interferometry or optical testing. Interferometry techniques use light beam superposition to form interference fringes that contain phase differences between the two beams of light [38].

The Shack-Hartmann WFS (SHWFS) is most common wave-front sensor for wave-front measurements. It consists of array of lens. This lenslet array is placed at a conjugate pupil plane in order to sample the incoming wave-front. The position of each spot directly provides information of the local wave-front tilt at each lens.

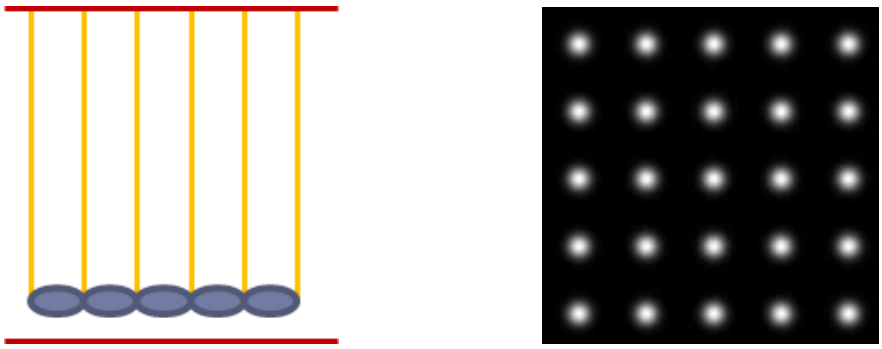

Figure 2. 2: (a) Wave-front sensing for plane wavefront and its corrsponding SH-spots

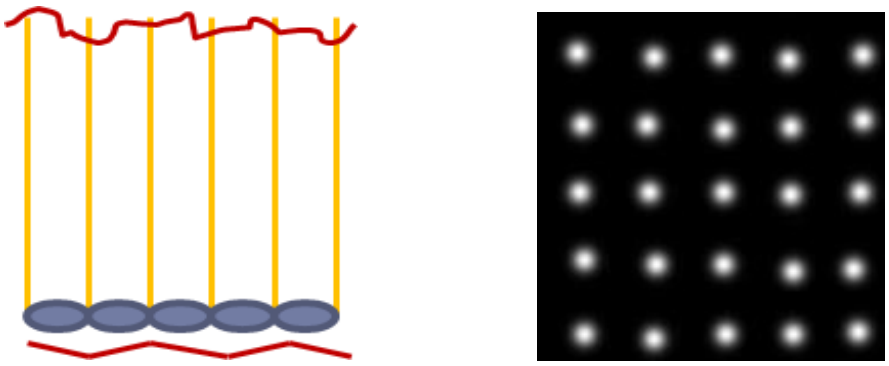

Figure 2. 3: Wave-front sensing for aberrated wavefront and its corrsponding SH-spots

2.4.1.2 Wave-front Correctors: A correction device must be added to the optical path to conjugate the beam to correct for phase fluctuations indirectly measured by the WFS. This device is commonly known in AO as the Wave-front Corrector (WFC). The WFC introduces into the system an optical phase shift ϕ by producing an optical path difference (OPD) δ. The phase shift is given by [39]

$$\phi = \frac{2\pi}{\lambda}\Delta(\eta e) \tag{33}$$

Where η is the refractive index,

e is the geometrical path spatial distribution of the corrector.

The most common WFC is Deformable Mirror. It consists of array of actuators which can deform according to WFS.

2.4.1.3 Real-time Control system: The purpose of the real-time control system (RTCS) is to interpret the WFS data to produce a set of meaningful control signals to position elements of the WFC, usually by reconstructing the wave-front. Each system component, including the RTCS, has a finite temporal response. The typical AO closed-loop system consists of a large number of highly coupled feedback loops working in parallel [40].

2.5 Conclusions

This chapter started with imaging with telescope. Fundamentals of atmospheric turbulence along with its effects on the propagation of optical beam are discussed. Basic turbulence parameters which are used to characterize the atmospheric turbulence are explained in detail. A brief introduction to AO system is described. Three major components wave-front sensor, wave-front corrector and control system are discussed.

Bibliography

[1] W. j. Smith, Modern Optical Engineering, McGraw-Hill, 2000.

[2] D. Jacobs, Fundamentals of Optical Engineering, New york: McGraw-Hill, 1943.

[3] A. M. Martin, . G. Harrie. and J. Rutten, Telescope Optics : A Comprehensive Manual for Amateur Astronomers, 1988: Willmann-Bell.

[4] W. j. Smith, "Chromatic aberration," in *Modern Optical Engineering*, New-York, McGraw-Hill, p. 61.

[5] S. Tonkin, Amateur Telescope Making (The Patrick Moore Practical Astronomy Series), London: Springer, 1998.

[6] S. J. Goodshell, "Astronomical Adaptive Optics Image Correction Theory," in *Optimis~ing the NAOMI Adaptive Optics Real-Time Contro:l System*, University of Durham, 2008, p. 7.

[7] S. F. Tonkin, Practical Amateur Spectroscopy, The Patrick Moore Practical Astronomy Series, 2002.

[8] S. Tonkin, Amateur Telescope Making, The Patrick Moore Practical Astronomy Series, 2004.

[9] S. K. Saha, Aperture Synthesis: Methods and Applications to Optical Astronomy, Spinger, 2011.

[10] H. Karttunen, P. Kröger, K. J. Donner and M. Poutanen, Fundamental Astronomy, New York: Spinger, 2003.

[11] S. K. Saha, Diffraction Limitted Imaging with Large and Moderate Telescopes, World Scientific, 2007.

[12] H. W. Babcock, "The possibility of compensating astronomical seeing," *Publications of the Astronomical Society of the Pacific,* vol. 65, no. 386, p. 229, 1953.

[13] D. M. Alloin and J. M. Marriotti, Adaptive Optics for Astronomy, London: Kluwer Academic publisher, 1993.

[14] S. J. Goodsell, Optimis~ing the NAOMI Adaptive Optics Real-Time Contro:l System, University of Durham: Durham, 2008.

[15] J. w. Hardey, Adaptive Optics for Astronomcial Telescope, New york: Oxford university press, 1998.

[16] R. Tyson, "Sources of Aberrations," in *Priniciples of Adaptive Optics*, New york, CRC press, 2011.

[17] S. J. Goodsell, "Astronomical Adaptive Optics Image Correction Theory," in *Optimis~ing the NAOMI Adaptive Optics Real-Time Contro:l System*, Durham Univerisity, 2008.

[18] R. Tyson, "Sources of Aberrations," in *Principles of Adaptive Optics*, New york, CRC press, 2006.

[19] K. Henjalic and B. Launder, "Characterization of flux and dynamic," in *Modelling Turbulence in Engineering and the Environment*, Cambridge University press, 2011, p. 33.

[20] F. RODDIER, ADAPTIVE OPTICS IN ASTRONOMY, Cambridge University press, 1999.

[21] F. Roddier, ADAPTIVE OPTICS IN ASTRONOMY, Cambridge University Press, 1999.

[22] V. I. Tatarski, Wave Propagation in a Turbulent Medium, Mcgraw Hill, 1961.

[23] A. N. Kolmogorov, "The local structure of turbulence in incompressible viscous fluid for very large Reynolds," in *Proceedings of the Royal Society of London*, 1991.

[24] D. L. Fried's, "Statistics for a geometric representation of wavefront distortion," *J.Opt. Soc. America*, vol. 55, pp. 1427-1435, 1965.

[25] F. Roddier, "The effects of atmospheric turbulence in optical astronomy," *Progress in Optics*, vol. 19, p. 281–376, 1981.

[26] D. L. Fried's, "Atmospheric turbulence optical effects: understanding the adaptive-optics implications," in *Adaptive Optics for Astronomy*, Kluwer Academic publisher, 1994, p. 25±57.

[27] "Optical propagation and image formation through the turbulent atmoshphere," in *Diffraction-Limited Imaging with Very Large Telescopes*, Kluwer Academic Publ, 1989, pp. 33-52.

[28] S. K. Saha, Diffraction Limitted Imaging with Large and Moderate Telescopes, World Scientific, 2007.

[29] M. A. Vandom, Wavefront sensing for Adaptive optics in astronomy, University of Canterbury, 2002.

[30] M. C. Roggemann, Imaging through turbulence, CRC press, 1996.

[31] H. W. Babcock, "The possibilities of compensating astronomcial seeing," *Publ. Asrton. Soc. Pac.*, vol. 65, pp. 229-235, 1953.

[32] R. Irwan, Wavefront estimation in astronomcial imaging, Univerisity of Canterbury, 1999.

[33] A. W. Lohamann and G. Weigelt, "Speckle masking in astronomy," *Applied Optics*, vol. 22, pp. 4028-4037, 1983.

[34] E. Thiebaut, "Strict a priori constraints for maximum likelyhood blind deconvolution," *J. Opt. Soc. Ame.*, vol. 12, pp. 485-492, 1995.

[35] J. Primot and G. Rousset, "Deconvolution from wavefront sensing," *Jou. SOc. Ame.*, vol. 7, pp. 1598-1608, 1990.

[36] V. Korkiakoski, IMPROVING THE PERFORMANCE OF ADAPTIVE OPTICS SYSTEMS WITH OPTIMIZED CONTROL METHODS, TEKNILLINEN KORKEAKOULU HELSINKI UNIVERSITY OF TECHNOLOGY, 2008.

[37] F. Roddier, M. Northcott and J. E. Graves, "A simple low-order adaptive opticssystem for near-infrared application," *Pub. Astron. Soc. Pac.*, vol. 103, pp. 131-149, 1991.

[38] G. Yoon, N. Doble and D. . T. Miller, "Wavefront Sensing and Diagnostic Uses," in *Adaptive Optics for Vision Science Principles, Practices, Design, and Applications*, A JOHN WILEY & SONS, INC., PUBLICATION, 2006, p. 63.

[39] "Wavefront Correctors for Vision Science," in *Adaptive Optics for Vision*

science Principles, Practices, Design, and Applications, A JOHN WILEY & SONS, INC., PUBLICATION, 2006, p. 83.

[40] L. Chen, "Control Algorithms," in *Adaptive Optics for Vision Science*, A JOHN WILEY & SONS, INC., PUBLICATION, 2006, pp. Principles, Practices, Design, and Applications.

Chapter 3

EXPERIMENTAL EVALUATION OF AO SYSTEM

This chapter will discuss about the IAO Hanle site conditions. Theoretical value of Strehl ratio is calculated from fitting error and time error. A laboratory model for experimental evaluation of Adaptive optics system is presented here. Each component of AO system and its detail specification is described in this chapter.

3.1 IAO Hanle :

The Indian Astronomical Observatory (IAO), located near Leh in Ladakh, India, has one of the world's highest sites for optical & infrared regions. A 2-m aperture optical-infrared telescope, the Himalayan Chandra Telescope (HCT) is installed at IAO. The location of the 2-m HCT is to the east of the peak at an altitude of 4500 meters above mean sea level. The site has high number of spectroscopic and photometric nights approximately 250 and 180 respectively per annum [1]. The median seeing condition is < 1 arcsec. The median wind speed (υ) is 2.2m/s. The RMS seeing condition (r_0) of IAO Hanle is 12.7cm at 500 nm [2].

The theoretical value of Strehl ratio is calculated for IAO Hanle in IR band. Due to longer wavelength of IR compared to visible band Fried's coherence length (r_0) is bigger r_0 increases as (6/5) power of wavelength as given in Eq 28. So value of r_0 at IR band 1.1 μm is 32.7cm. Hence AO system design is less complex for larger r_0.

The Strehl ratio formula relating wavelength is $S = e^{-(\sigma^2_{fitting} + \sigma^2_{time})}$ [3]. The other errors like calibration error, isoplanatic and noise error are not considered so far.

3.1.1 Fitting error :

The fitting error [4] is defined to be the component of the wave aberration that the CDM cannot fit since phase is continuous and CDM is discrete in nature. This error depends on the spatial characteristics of the aberrations to be corrected and on the spatial characteristics of the CDM, such as the spacing, influence function, and stroke of the actuators.

$$\sigma^2_{fitting} = 0.335(\frac{D}{r_0})^{\frac{5}{3}} N^{\frac{-5}{6}} \quad (34)$$

N is called degree of freedom. It is the no of actuators used in phase correction. In laboratory

CDM has 144 actuators. Using N=144 and r_0 value 32.7cm at IR band $\sigma^2_{fitting}$ = 0.335 radian^2.

3.1.2 Time error:

Equation.31 describe the spatial distribution of wave-front distortions. It allows us to determine the number of parameters we need, to control the wavefront surface and the amplitude of the correction to be applied, but it does not tell us how fast this must be done. The mean square phase error σ^2_{time} associated with a pure delay τ in which the phase is measured at time t but the correction is applied at time t + τ [5].

$$\sigma^2_{time} = 6.88(\frac{v\tau}{r_0})^{\frac{5}{3}} \quad (35)$$

Where v is median wind speed 2.2 m/s. and time delay τ = 0.02 sec.

Putting these values we get

σ^2_{time} = 0.243 radian

Hence the Strehl ratio $S = e^{-(\sigma^2_{fitting} + \sigma^2_{time})}$ = 0.54

So the Adaptive Optics system at IR band 1.1 μm with Fried's coherence length r_0 have theoretical Strehl ratio S = 0.54. Here, other errors such as calibration and noise errors are neglected, as of now. Hence, the theoretical value of Strehl ratio in this AO system is 0.54.

3.2 Experimental Setup:

In order to understand the performance of Adaptive Optics system, a laboratory model has been proposed in AO lab of CREST campus. The components of the closed loop AO system are mounted on a Newport Optical Bench, which can be floated to isolate the components from external vibrations. Components including Shack-Hartmann (SH) wave-front sensor, continues membrane deformable mirror (CDM) and phase plate have been studied experimentally. The system has five parts:

- A light source
- Optical collimation part, which is composed of two 4f system
- Deformable mirror
- Shack-Hartmann wave-front sensor
- A PC with real-time control software

The lenses in the system are doublet with 250 mm focal length and triplet lens with 125 mm focal length. All the optical elements were lifted 120 mm above the optical table to aligning the optical axis of the system. This will make the assembly match with the height of the deformable mirror aperture. The experimental setup is shown in Figure 3.1 [6]. Brief description of each components is also given .

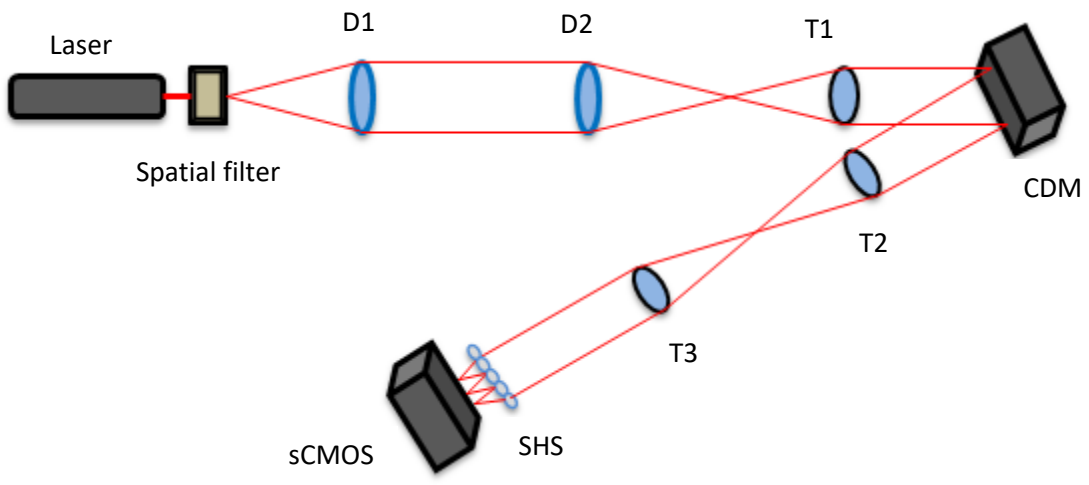

Figure 3. 1: Schematic setup for the closed loop AO system experiment

3.2.1 Laser: A He-Ne laser is a type of gas laser operating at a wavelength of 632.8 nm (red part of the visible spectrum) is used in the experiment. The narrow beam from the laser source was spatially filtered and expanded using a spatial filter setup.

3.2.2 Spatial filter: A spatial filter is essentially a beam converging device coupled with a filter. The filter, or pinhole, is used to remove interference patterns in a laser beam caused by diffraction from dust, lens imperfections, etc. that are part of any laser optical system. Diffraction interference degrades the laser beam by producing phase and amplitude variations, or modulation, on the otherwise uniphase laser output, leading to Fresnel zone patterns in the beam. The interference is removed from the beam and the laser output appears as a point source at infinity. Figure 3.2 shows spatial filtering of laser beam.

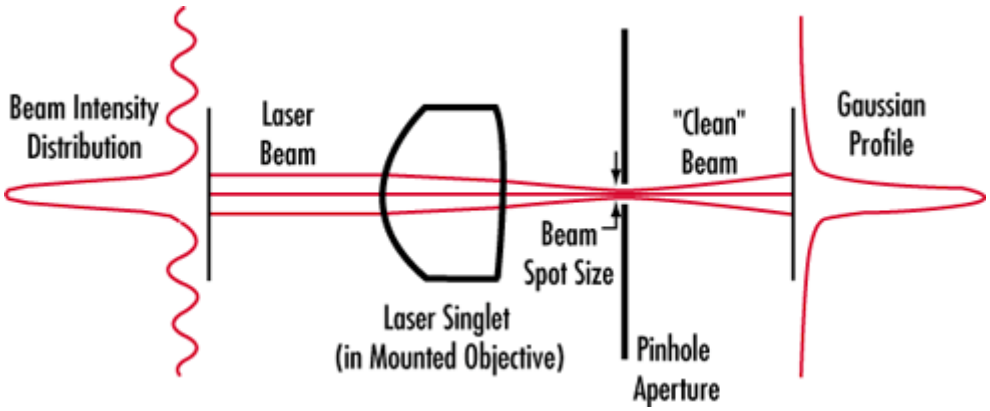

Figure 3. 2 : Spatial filtering of laser beam

The optimum pinhole diameter is a function of the laser wavelength, laser beam diameter, and focal length of the microscope objective used. They are related by

$$\text{Pinhole diameter} = \frac{8}{\pi} \times \frac{wavelength \times focal\ length}{diameter} \tag{36}$$

Applying the above formula, commercially available pinhole sizes and objectives for spatial filtering purposes can be matched. Common Helium-Neon (HeNe) lasers have a wavelength of 0.6328µm and a beam diameter of 1mm, and using these parameters gives the following selection table:

Pinhole diameter	Objective	Focal length
50 µm	5 x	25.5 mm
25 µm	10 x	14.8 mm
15 µm	20 x	8.3 mm
10 µm	40 x	4.3 mm
5 µm	60 x	2.9 mm

Table 1: Pinhole diameter with objective magnification and focal length

3.2.3 Lens: The divergent beam from the spatial filter is passed through achromatic doublet lens having focal length of 250 mm which is placed behind the spatial filter setup to make the beam collimated. Triplet lens having focal length of 125 mm is used in 4f geometry. It removes high frequency components. The beam from the microscope objective passes through a doublet lens and expands the beam to 10 mm beam in diameter. The doublet lenses are used to manage diameter of the beam as it travels through the testbed.

3.2.4 Wave-front sensor: The Shack–Hartmann wave-front sensor contains a lenslet array that consists of a two-dimensional array of a few hundred lenslets, all with the same diameter and the same focal length. The Shack-Hartmann wave-front sensor used in the experimental setup is an OKO Technologies Shack-Hartmann wave-front sensor made up of fused silica [7].

Dimension	61 x 61 mm
Lens	200 x 200
Diameter	200 μm
Pitch	200 μm
Focal length	40 mm
f-number	200

Table 2: Specification of SHS

The imaging camera is a high resolution low noise cooled sCMOS camera from Photonic Science [8] is placed at its focal length of SHWFS. Detail specification is given in the table 2.

Size	12.48mm x 7.02mm
Arrays	1920 (h) x 1080 (v)
Pixel size	6.5 x 6.5 μm
Fullwell capacity	>30,000 electrons
Readout noise	~1.2 electron
Dark current	< 0,5 electrons / pixel / second
Dynamic range	up to >20,000:1
Frame rate:	18 fps at full resolution

Table 3: Specification of sCMOS camera

This sCMOS camera connects the computer through GEV Player, part of the Pleora Technologies eBUS™ SDK software development kit. GEV Player also receives and allows to stream data. While viewing the image data, GEV Player can be used to adjust the image color and white balance, and save the images. This sCMOS camera requires a Cat5 network cable for GigE data interface.

3.2.5 Computer control: The desktop computer used in this experiment is a work station from DELL Corp. having a 64 bit INTEL Xeon processor and running window 64 bit operating system with RAM size of 16 Gb.

3.2.6 Deformable mirror: Since in most applications, the wave-fronts to be corrected by the CDM are continuous in nature, it is advantageous to use the CDM with precise calibration. In this experiment the Multi-DM, manufactured by Boston Micro-machine Corporation (BMC) was used [9]. Its specification is given in Table 4.

Aperture	4.9 mm^2
Actuators Count	140
Max. Stroke	5.5 µm
Actuator Pitch	450 µm
Mirror Coating	Aluminum
Avg step size	< 3 nm
Max voltage	300 V

Table 4: Specification of CDM

3.2.7 CDM software: The Multi-DM System comes with Demonstration Software called LinkUI. It is designed to allow the user to address the DM actuators, voltage patterns, and user-defined voltage maps. Data entered into the BMC LinkUI software corresponds to the 14 bit DACs that drive each mirror channel. Each data number corresponds to ~18mV applied to the mirror.

3.2.8 Data acquisition: The deformable mirrors are controlled using MATLAB. MATLAB interfaces to the deformable mirrors through a MATLAB executable (MEX) .dll developed by Baker Adaptive Optics. The individual mirror actuators can are addressed through MATLAB, and a control signal between 0 and 255 can be applied individually. The SHS is also interfaced with MATLAB image acquisition tool box. The continuous image capturing is done directly to the computer hard disk image acquisition tool box.

The He-Ne laser was pre-aligned. The spatially filtered beam is collimated using doublet lens D1 with focal length 250 mm is placed at the focal plane of the source. So it was a planar wave-front at the output of the D1 with a diameter of the beam 10 mm.

The collimation of the beam is checked using a sheer plate. The collimated beam is passed to another lens system which consist of a doublet lens D2 and a triplet lens T1 (focal length =125 mm). The output of the beam from T1 is collimated but reduced in size of 5 mm. This collimated beam is reflected by CDM and passed to a 4f system which consists of two triplet lens having focal length of 125 mm. The SHS is placed at the image plane of this 4f system where CDM acts as an object plane. Figure 3.3 shows the actual setup for wave-front compensation.

The collimated beam is required to calibrate the Shack-Hartmann wave-front sensors. The wave-front sensors operate based on the known positions of the lenslets on the Hartmann mask and their alignment with the CCD. To calibrate the wave-front sensor and remove any tip/tilt bias due to the optical components, a collimated beam was passed into the wave-front sensors and a reference image was captured. This reference image is used to measure the phase difference from a planar wave.

Figure 3. 3: Experimental setup for wave-front compensation

3.3 Calibration of sCMOS camera

sCMOS camera from Photonic science is calibrated before its use. The reason for calibration is to correct for unwanted data elements that are found in each raw data frame such as bias offset, dark current, uneven chip illumination etc. Generally the images captured by the camera and each of this pixel in the images will have a numeric value that includes the influences of light from the objects in the field of view, various types of noise generated by the camera and cosmic ray hits [10] [11].

This unwanted signal is called as noise, which doesn't improve the quality of the image. In fact, it will degrade it. The main problem with noise is that most noise is essentially random, and so cannot be completely removed from the image. Figure 3.4 gives a comparison of ideal case and noise presented in an well when electron is collected.

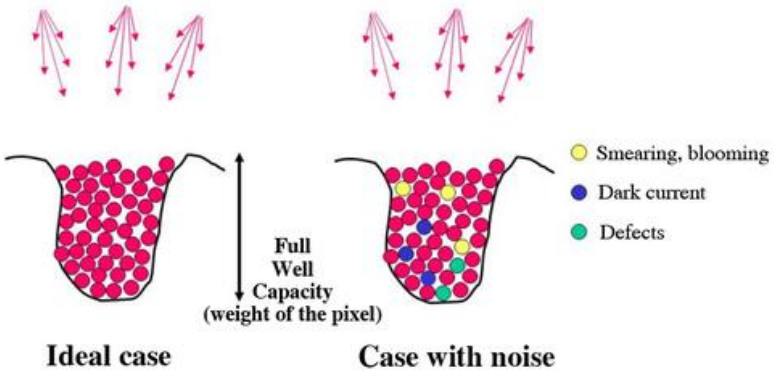

Figure 3. 4: A comparison of electron in ideal case and in presence of noise

3.4 Types of noise

In real image sensors, the voltages, currents, conductors and capacitances of the sensor are changes rapidly. As a result, the noise is not stationary. Temporal noise is the temporal variation in pixel output values under constant illumination. There are many sources that can cause temporal noise in CMOS image sensors. Shot noise occurs when photo-electron are generated. Additional noise is added when thermally

induced motion of electron as dark noise and reading out the pixel value as readout noise.

3.4.1 Shot noise

The dominant noise in an image by the camera is caused by statistical fluctuations, that is variation in the number of photons sensed at a given exposure level. This noise is known as photon shot noise. Shot noise has a root-mean-square value proportional to the square root of the image intensity. The deviation in intensity found for each image follows the well known Poisson distribution. The magnitude of shot noise increases according to the square root of the number of photons. Expression for shot noise is given by

If number of photon P falling on a camera pixel with a quantum efficiency D_{QE}, then the signal of N_e electron is given by

$$N_e = D_{QE} P \tag{37}$$

Then the shot noise is given by

$$\delta_{signal} = \sqrt{D_{QE} P} = \sqrt{N_e} \tag{38}$$

3.4.2 Thermally generated noise*:*

Additional electrons will be generated within the camera not by the absorption of photons (i.e the signal) but by physical processes within the camera itself. The number of electrons generated in a second will be dependent on the operating temperature of the camera and hence this noise is known as thermal noise (sometimes also known as dark noise). As with the detection of the signal, the same number of electrons will not be generated in equivalent periods of time as the thermal noise will also have a Poisson distribution. The simplest way to reduce the dark noise is to cool the camera as dark noise generation is temperature related.

3.4.3 Readout noise

The ultimate noise limit of the CCD is determined by the readout noise. The readout noise is the noise of the on-chip amplifier which converts the charge (i.e the electrons) into a change in analogue voltage using.

3.4.4 Pixel Non-Uniformity

Today's cameras are made to exacting standards, but they still are not perfect. Each pixel has a slightly different sensitivity to light, typically within 1% to 2% of the average signal. Pixel non-uniformity can be reduced by calibrating an image with a flat-field image.

Camera manufacturers measure and report noise as a number of electrons RMS (Root Mean Square). It is presented like $15e^-$ RMS, meaning that with this camera should expect to see *about* 15 electrons of noise per pixel. More precisely, $15e^-$ RMS is the standard deviation around the mean pixel value.

3.5 Calibration procedure

A calibration routine, if properly applied can effectively remove most of the unwanted effects of dark current and uneven field illumination. Calibration however does not correct for cosmic ray hits to the detector [12]. A basic camera calibration procedure is given.

Dark frames: It is also called "thermal frames", correct for dark current collected on the detector. The gradual accumulation of electrons (the dark current) in the pixels of the detector which depends on the temperature of the detector. Dark frames are images taken with no light falling on the CCD, so that the only values present in the pixel are due to bias and dark current. Dark frames are acquired by placing a lightproof cap over the sCMOS camera and a series of 5 frames with same exposure, temperature and gain are captured. All the 5 frames are averaged into a single master dark frame. This will minimize the noise in the master frames.

Bias frames: it removes the effects of the electrical charge applied to the detector prior to the exposure. “Bias” is the electric pre-charge applied to the chip by the camera electronics to activate its photon collecting ability. 5 no of such frames are taken with zero exposure time and by averaging it a master bias frames is taken. The master dark frame are to be subtracted from the reference frame in image processing.

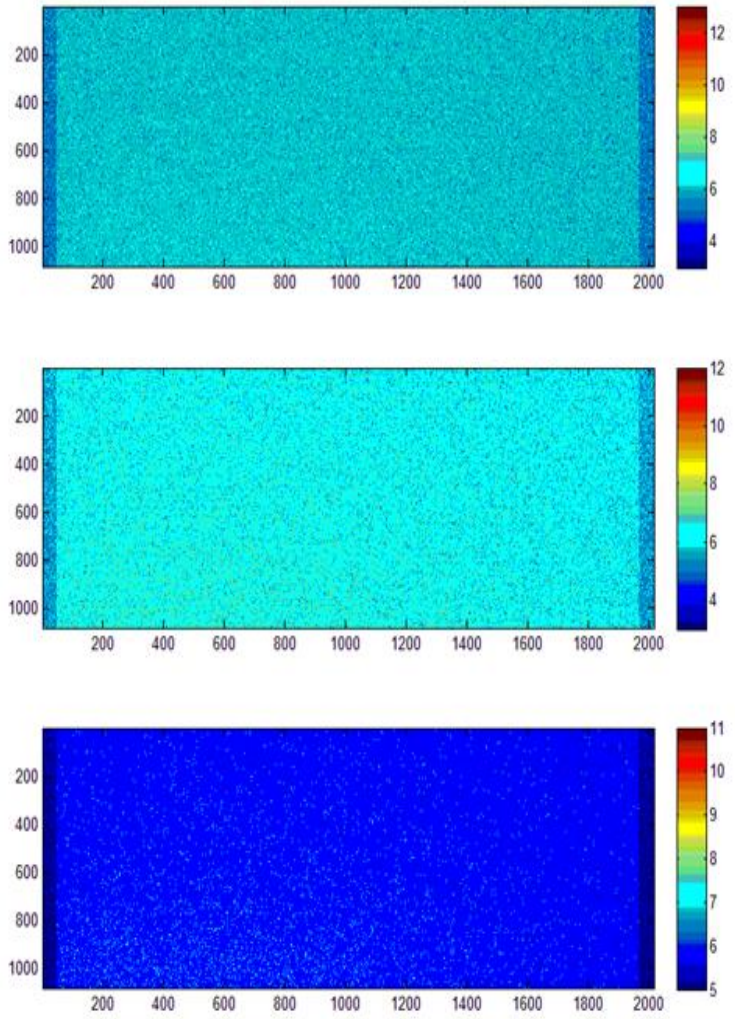

Figure 3. 5: (a) Shows 1st dark frame, (b) shows 5th dark frame, (c) shows average of 5 frames i.e master dark frame

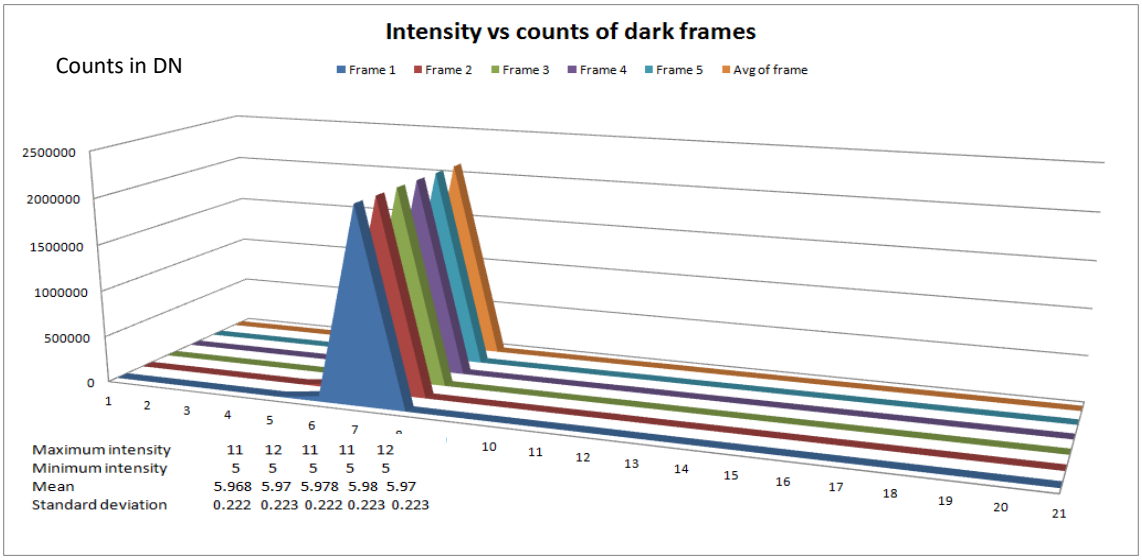

Figure 3. 6: Intensity vs no of counts in DN for all 5 frames including master frame

From Figure 3.5 and Figure 3.6 it is found that mean counts in dark frames are 5.98 DN i.e approximately 6 DN. A "Bias Frame" is a zero-length (dark) exposure intended to measure just the difference between the pixels. One common use of bias frames is for scaling dark frames. By subtracting a bias frame from a dark frame end up with a "thermal frame." A thermal frame contains pixel values showing just the effect of dark current. Because dark current in any given pixel accumulates at a constant rate, a thermal frame allows you to predict with reasonable accuracy how much dark current there would be for different length exposures. However, given the opportunity, you're always better off taking dark frames that match the exposure times of your light frames.

A series of master dark frames are taken with different temperature. The relationship between no of counts of master frame with temperature is given in Figure 3.7.

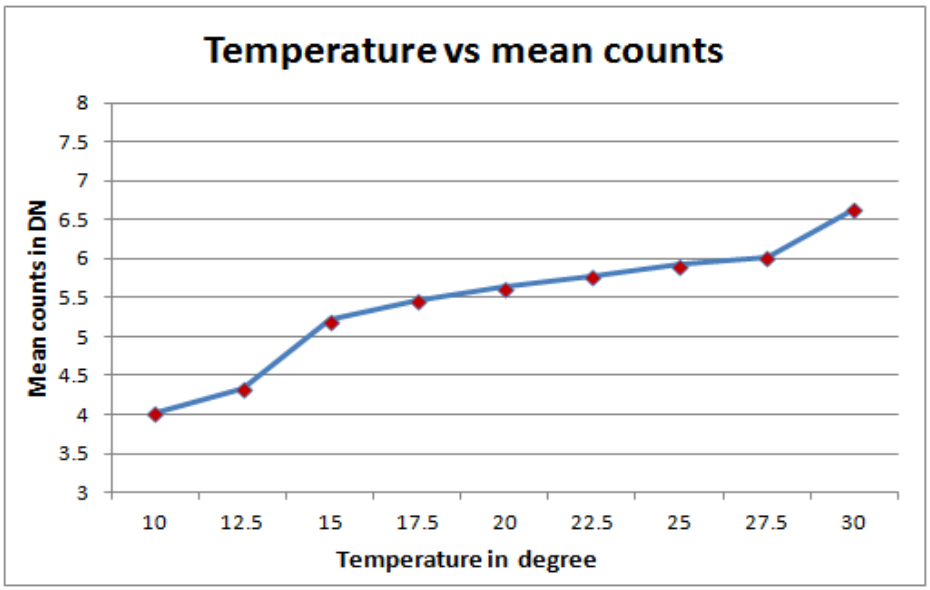

Figure 3. 7: Relationship between master dark frame and temperature.

Another series of dark frames by changing exposure time starting from 50 µs to 1sec are taken. Mean counts of dark frames are found out with different exposure time of the camera. Figure 3.8 Shows a relationship between mean counts of dark frame with different exposure time.

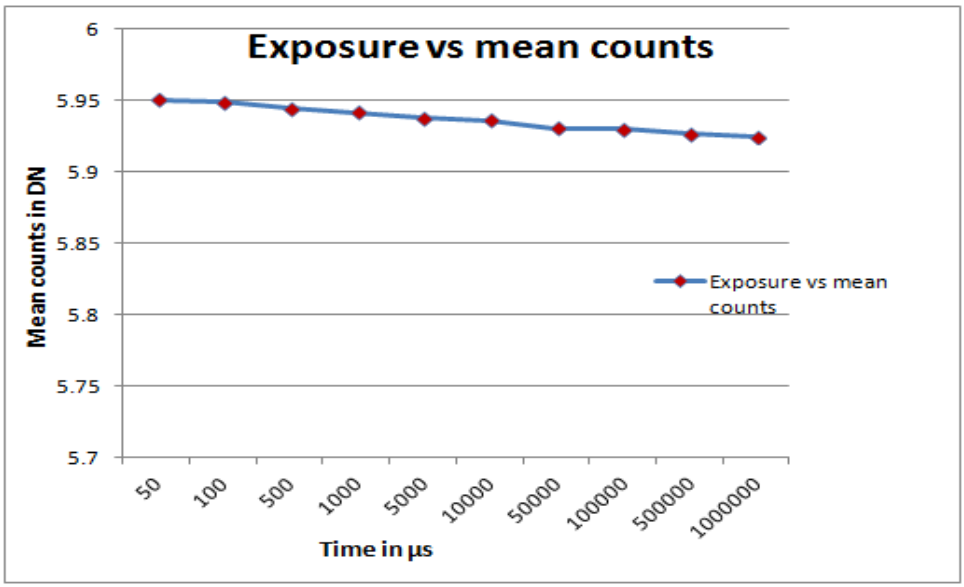

Figure 3. 8: Relationship between counts of dark frame and time in µs

3.6 Conclusions

The proposed laboratory model has been discussed to understand the Adaptive Optics system. Detail specifications of each optical components, SHS and CDM are given. A theoretical value of Strehl ratio is calculated taking fitting error and time error. sCMOS camera is calibrated before its use. The mean count of dark frames are calculated for various frames by changing exposure time of the camera and varying temperature. This dark frame is to be subtracted in real time depending in temperature and exposure of observation.

Bibliography

[1] T. P. Prabhu, "Indian Astrnomical Observatory, Leh- Hanle," *Proc Indian national sci academy*, vol. 80, pp. 887-912, 2014.

[2] B. C. Bhatt, D. k. Sahu, C. S. Stalin, T. P. Prabhu and G. C. Anupama, "Night sky at the Indian Astrnomical Observatory during 200-2008," *Bull. Asto. Soc. India*, 2008.

[3] J. Porter, K. Thorn and H. Queener, WAVEFRONT MEASUREMENT AND ABERRATION, Wiley Interscience, 2006, p. 119.

[4] F. Roddier, "Adaptive Optics in Astronomy," Cambridge University Press, 1999, p. 23.

[5] J. PORTER, H. . M. QUEENER and K. THORN, Adaptive Optics for Vision Science, A JOHN WILEY & SONS, INC., PUBLICATION, 2006.

[6] M. B. Roopshree, A. Vyas and B. R. Prasad, "Intensity Weighted Noise Reduction in MEMS Based Deformable Mirror Images," in *AIP Conf Proc.*, 2011.

[7] M. Loktev, O. Soloviev and G. Vdovin, "Flexible Optical BV (OKO Technologies)," April 2008. [Online]. Available: http://www.okotech.com/sensors.

[8] D. Brau , "info@photonic-science.co.uk," 2010. [Online]. Available: http://www.photonic-science.co.uk/products/SCMOS-camera.html.

[9] P. Zeng, "Boston Micromachines Corporation," 2009. [Online]. Available: http://www.bostonmicromachines.com/.

[10] B. Christian, CCD Astronomy: Construction and Use of an Astronomical CCD Camera, Willmann-Bell, 1991.

[11] P. Martinez and A. Klotz, A Practical Guide to CCD Astronomy, Cambridge University Press, 1998.

[12] S. B. Howell, Handbook of CCD Astronomy, Cambridge : Cambridge University Press, 2000.

Chapter 4

WAVE-FRONT SENSING

Wave-front sensing principles is discussed in this chapter. It starts with Shack-Hartmann wave-front sensor principles, centroding technique, sampling geometry, and least-square method for wave-front phase reconstruction. Control matrix 'A' is created using Matlab and its performance is checked using simulated Zernike polynomials and Kolmogorov polynomials.

4.1 Wave-front sensing principles:

Wave-front sensor measures the wave-front aberrations. This wave-front estimate is used to drive a corrector element, usually a deformable mirror. Direct sensing of a wave-front is not possible at optical frequencies, because the wave-front phase does not interact with matter in any measurable way. Instead the wave-front must be deduced from intensity measurements. There are two different types of wave-front sensing: geometric and interferometric. Geometric wave-front sensors rely on the fact that light travels in rays perpendicular to the wave-front. This encompasses Shack-Hartmann, curvature and pyramid wave-front sensors. Interferometric method consider the interference between different parts of the wave-fronts. The lateral shear interferometer and phase retrieval methods fall into this class [1].

The Shack-Hartmann wave-front sensor is mostly used wave-front sensor in astronomical adaptive optics. A slope in the wave-front displaces the image, and the measurement of this displacement forms the basis of the SHS [2]. Using a lenslet array, the exit pupil is divided into a square of sub-apertures and each sub-aperture is focused onto a different point in the focal plane. If the wave-front is planar, then the image are focused to a point directly below the centre of the lenslet, as illustrated in Figure 4.1. If, on the other hand, there is an overall mean wave-front slope over the extent of a sub-aperture, that image will be displaced from the centre as shown in Figure 4.1.

The relationship between wave-front slope (the first derivative of the wave-front) and the spot displacement, Δx and Δy with respect to the x and y directions, can be expressed as [3]:

$$\frac{\partial W(\mathrm{x},\mathrm{y})}{\partial x} = \frac{\Delta x}{F} \tag{39}$$

$$\frac{\partial W(\mathrm{x},\mathrm{y})}{\partial y} = \frac{\Delta y}{F} \tag{40}$$

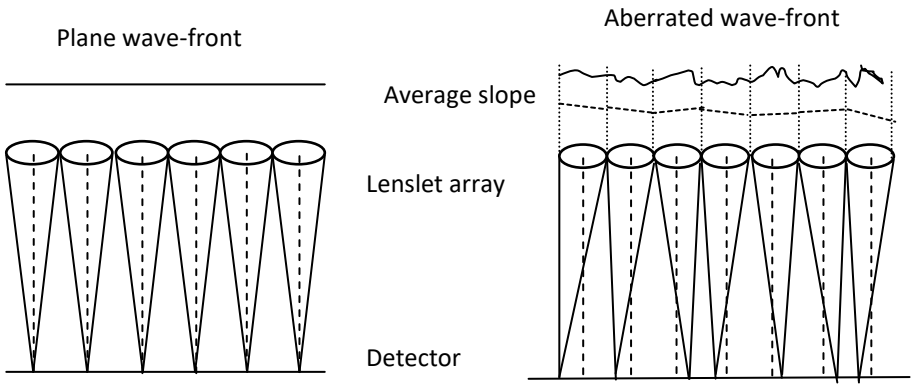

Figure 4. 1: Shack-Hartmann sensor with (a) a planar wave-front and (b) an aberrated wave-front. The dashed lines are the perpendicular bisectors of the lenslets

4.2 Sampling Geometry

Local gradients are measured at discrete locations of the wave-front. Depending on the position at which phase differences are estimated with reference to the location of slope measurements. Usually detector records the images of the spot. Center of gravity (CoG) method [4]is used to detect the location of spot on the detector. The CoG method defines centroid position (x_c, y_c) as

$$(x_c, y_c) = \frac{\sum_{ij} x_{ij} I_{ij}}{\sum_{ij} I_{ij}} \tag{41}$$

There exist three main classifications in wave-front sampling namely Fried's geometry, Hudgin geometry and Southwell geometry. These configurations that illustrate the relationship between positions of slope measurements (in x and y directions) as shown in Figure 4.2.

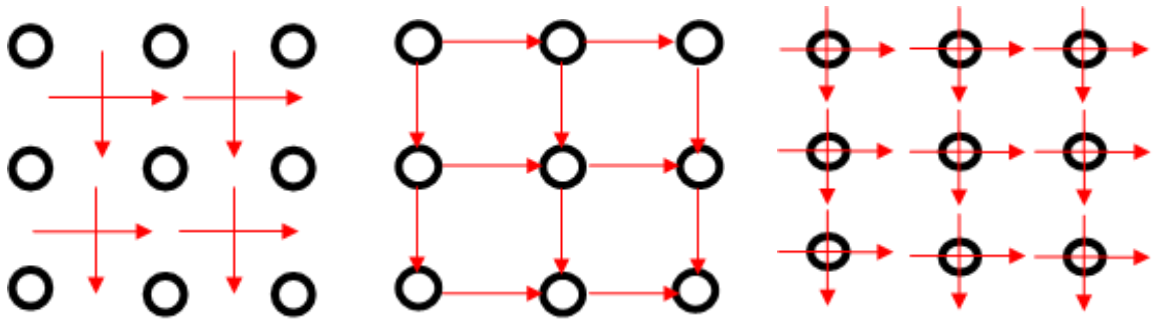

Figure 4. 2: (a) Fried's geometry, (b) Hudgin geometry, (c) Southwell geometry. Horizontal and vertical lines represent positions of slope measurements in x and y directions circle represent positions of phase estimation.

In Fried's configuration, phase evaluation grid is displaced by half the sensor pitch with respect to slope measurement grid. For Fried's geometry [5].

$$S^{x}_{ij} = \frac{[(\phi_{i+1,j} + \phi_{i+1,j+1})/2 - (\phi_{i,j} + \phi_{i,j+1})/2]}{h} \tag{42}$$

$$S^{y}_{ij} = \frac{[(\phi_{i,j+1} + \phi_{i+1,j+1})/2 - (\phi_{i,j} + \phi_{i+1,j})/2]}{h} \tag{43}$$

Where i=1,2 ....(N-1), and j=1,2….(N-1)

In Hudgin configuration, x and y slope measurement points are displaced from one another and phase is evaluated at the edges of the slopes [6].

$$S^{x}_{ij} = \frac{[(\phi_{i+1,j} - \phi_{i,j})/2]}{h} \tag{44}$$

$$S^{y}_{ij} = \frac{[(\phi_{i,j+1} - \phi_{i,j})/2]}{h} \tag{45}$$

Where i=1,2 ....N, and j=1,2….(N-1)

Slope measurement points coincide with the phase evaluation points in the Southwell configuration [7]

$$\frac{S^{x}_{i+1,j} + S^{x}_{i,j}}{2} = \frac{\phi_{i+1,j} - \phi_{i,j}}{h} \tag{46}$$

$$\frac{S^{y}_{i,j+1} + S^{y}_{i,j}}{2} = \frac{\phi_{i,j+1} - \phi_{i,j}}{h} \tag{47}$$

Where i=1,2 ....N, and j=1,2….(N-1)

4.3 Wave-front estimation from wave-front slope

Methods for determining the phase of the wave-front are described as either zonal or modal. The methods are simply two different models used to describe the local slope

measurements of a Shack-Hartmann wave-front sensor. A zonal method estimates a phase value in a local zone while the modal method is based on a coefficient of an aperture function. In both cases least-squares estimation is used for the phase reconstruction and wave-front estimation.

4.3.1 Zonal Estimation

Above equations can be represented in matrix formalism as over determined linear system of equations as follows [8]. This process is also known as ' Vector Multiplication Method'.

$$S = A * \phi \tag{48}$$

Where '*A*' is called interaction matrix associated with the phase difference vector. This matrix changes with the sampling geometry. The slope vector *S* contains x- and y-slopes for all valid sub-apertures in the pupil.

Eq.43 can be solved for 'ϕ' by computing the generalized inverse of 'A' and pre-multiplying the right hand side of the equation by it.

$$\phi = (A * A^T)^{-1} * A^T * S \tag{49}$$

Error is given by $\varepsilon_s = \|S - A\phi\|^2$

If N is the number of sampling point then dimension of S will be $2N^2$x1. Dimension of ϕ will be N^2x1 and dimension of coefficient of matrix A will be $2N^2$xN^2. Hence, computation involved in this Vector Multiplication Method is N^4. As the size N increases the computation time in this method also increases.

4.3.2 Modal Estimation

A wave-front that is described by coefficients of the modes of a polynomial expansion over the pupil is considered modal [9]. Using the slope measurements from

the Shack-Hartmann wave-front sensor a set of coefficients, a_k, can be obtained that fit the following phase expansion of orthogonal functions. In this case $Z_k(x,y)$is a set of Zernike polynomials [10] . Zernike polynomials are used as they are a set of orthogonal polynomials over the unit circle. Eq. 45 can be written as a matrix where the individual phase points that describe the wave-front are contained in the vector $\phi(x,y)$, the Zernike coefficients are contained in vector a , and matrix Z contains a matrix of the Zernike terms evaluated at the phase points x and y shown in Eq. 46 [11].

$$\phi(x,y) = \sum_{k=0}^{M} a_k z_k(x,y) \tag{50}$$

$$\phi(x,y) = aZ \tag{51}$$

The M phase expansion coefficients, a , is solved using a least squares estimation, by taking the pseudo-inverse of Z at the measured phase points from the Shack-Hartmann wave-front sensor and premultiplying both sides of Equation (4.15) resulting in Equation (4.16). This reduces the numerical complexity of the wave-front estimation, from the number of Shack-Hartmann lenslets to the number of expansion terms used.

$$a = Z^{\dagger}\phi \tag{52}$$

A slope model can be obtained by differentiating Eq. 45. The resulting relationship for the slope in the x and y direction are shown in Eq. 48 and 49, respectively. This allows the slopes, which are measured by the Shack-Hartmann wavefront sensor to be directly related to the partial derivatives of the Zernike polynomials. Eq. 48 and can be written in matrix form, as shown in Eq.50 , where S is a vector of x and y slopes with the dimensions 2N x 1 and dZ is a Matrix of the partial derivative of the Zernike terms evaluated at each lenslet, having 2N rows and M columns. The Zernike coefficients can be found by solving the least squares problem with the solution given in Eq. 51. The benefit of this model phase estimation is that it does not require a zonal phase estimation as Eq.47. However, by differentiating Eq.45, the piston component of the phase, coefficient a_0 , can not be determined [12].

$$S_x = \sum_{k=1}^{M} a_k \frac{\partial z_k(x,y)}{\partial x} \tag{53}$$

$$S_y = \sum_{k=1}^{M} a_k \frac{\partial z_k(x,y)}{\partial y} \tag{54}$$

$$S = [dZ]a \tag{55}$$

$$a = [dZ]^{\dagger} S \tag{56}$$

4.4 Simulation of Kolmogorov turbulence

Interaction matrix 'A' is created in Matlab platform using Fried's geometry. In order to test its performance simulated version of Kolmogorov turbulence is used. The Kolmogorov power spectrum was modified by Von Karman power spectrum which is given by [13].

$$\phi_N^k = 0.023 C_n^2 (k^2 + k_0^2)^{-11/6} \exp(-\frac{k^2}{k_i^2}) \tag{57}$$

Where $k_0 = \frac{2\pi}{L_0}$, $k_i = \frac{2\pi}{l_0}$

For infinite outer scale k_0 and zero inner scale k_i above equation reduces to

$$\phi_N^k = 0.023 (\frac{D}{r_0})^{5/3} (k)^{-11/3} \tag{58}$$

The Power spectral density (PSD) and phase screen *f(r)* are related as

$$\phi_n(k) = \left| \int_{\infty}^{\infty} f(r) e^{-ikr} dr \right|^2 \tag{59}$$

From the above equation phase screen is given by

$$f(r) = \int_{\infty}^{\infty} \sqrt{\phi_n(k)} e^{ikr} dk \tag{60}$$

Where, *f(r)* is 2D - Kolmogorov phase screen, can be obtained from inverse Fourier Transform of square root of Von Karman power spectrum of turbulent atmosphere . Low spatial frequencies represents large scale eddies of atmosphere, the main contribution from it is the beam to wander. These low spatial frequencies contribute more distortion to the wave-front. The large spatial frequencies represents small scale eddies of atmosphere; the main contribution is intensity fluctuation [14].

In Sub-Harmonics method, the phase screens were generated by the Fourier Transform method used. A simple technique for modelling the effects of these lower frequencies is to generate additional random frequencies and add their effects to the simple sampled frequencies given by Eq. 56. Then, a low frequency screen $\phi(x, y)$ is generated by sum of different phase screens(*Np*), as given by

$$\phi(x, y) = \sum_{p=1}^{N_p} \sum_{n=-1}^{1} \sum_{m=-1}^{1} C_{n,m} \exp[i2\pi(f_x + f_y)] \tag{61}$$

Where, the sums over *n* and *m* are over discrete frequencies and each value of the index *p* corresponds to a different grid. The first summation relies on the addition of sub harmonics of the aperture and gives a very accurate phase structure function. In this calculation, the phase screen values are derived by addition of two phase screens obtained with Fourier transform method and sub Harmonics method [15].

In Figure 4.3 simulated version of Kolmogorov phase screen is given in 3D. It shows the typical atmospheric phase screen simulated by FT method with $D/r_o = 2$, outer scale (L_0)=50 m, inner scale (l_0)=0.01m. In this case it is observed that low spatial frequencies are not sampled well (i.e., no tip / tilt).

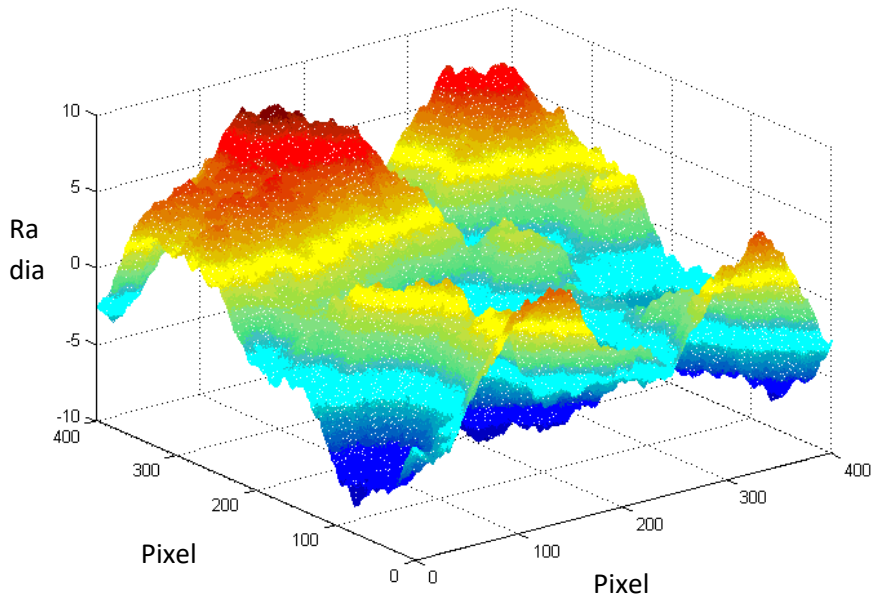

Figure 4. 3: Simulated Kolmogorov phase screen

Now Kolmogorov phase screen act as input and its corresponding shifted SH-spots pattern is recorded. Using least-square method from the shifted SH-spots pattern output phase screen is obtained. This is repeated for 100 times and correlation coefficients between input wave-front and output wave-front is recorded. The RMS error between input and output wave-front is also recorded. Figure 4.4 shows example of two cases where Kolmogorov as input wave-front and output from the shifted SH-spot pattern with their RMS wave-front error.

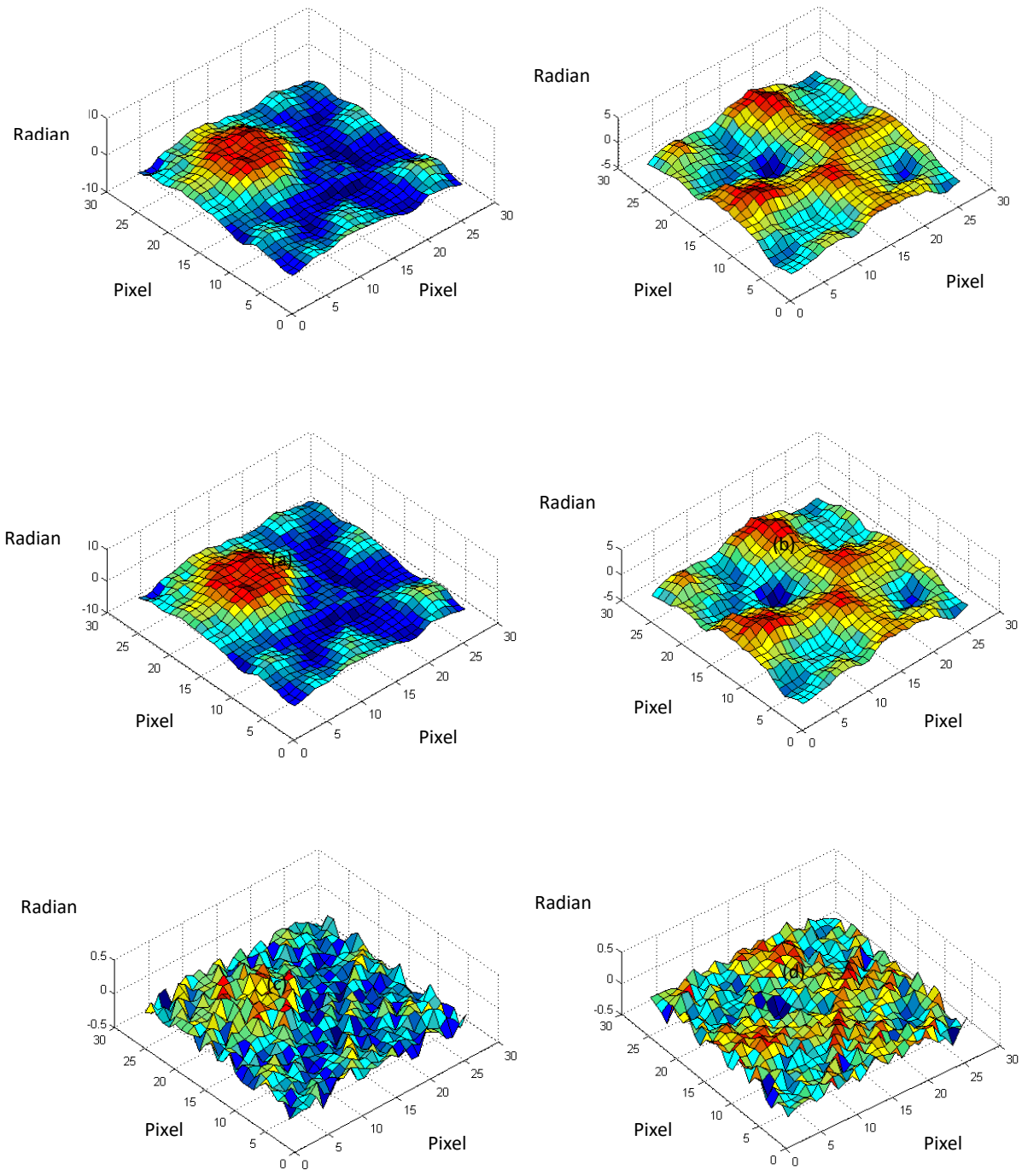

Figure 4. 4: (a) & (b) Input Kolmogorov phase screen, (c) & (d) output phase screen from SH-spots. (e) & (f) RMS wave-front error

The accuracy of wave-front reconstruction algorithm is tested for Kolmogorov phase screen 100 times. Each time correlation coefficients between input and output phase screen are determined. The relation between correlation coefficients and Kolmogorov phasescreen are plotted and given in Figure 4.5. The RMS wave-front error between input phase screen and output phase screen is given in Figure 4.6.

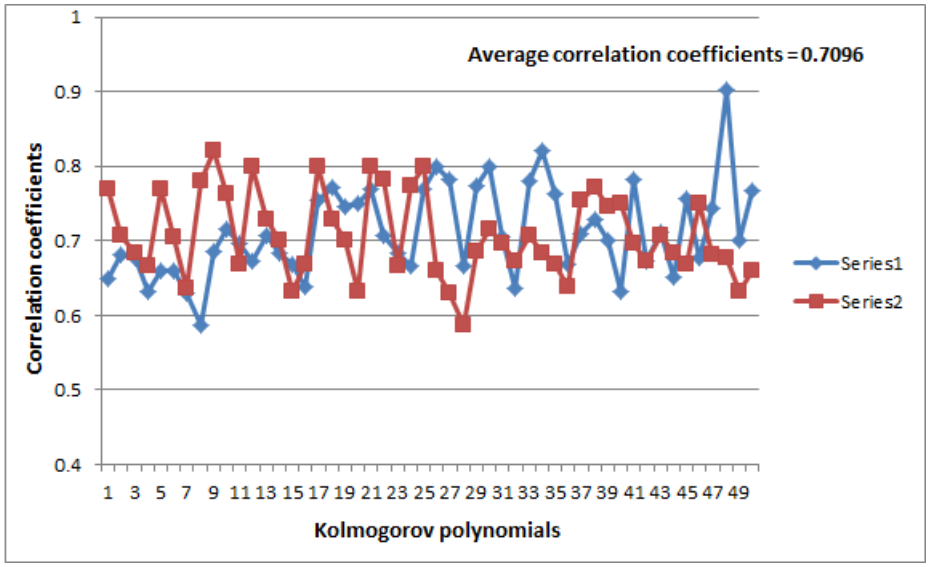

Figure 4. 5: Correlation coefficients between input and output phase screen of Kolmogorov polynomials.

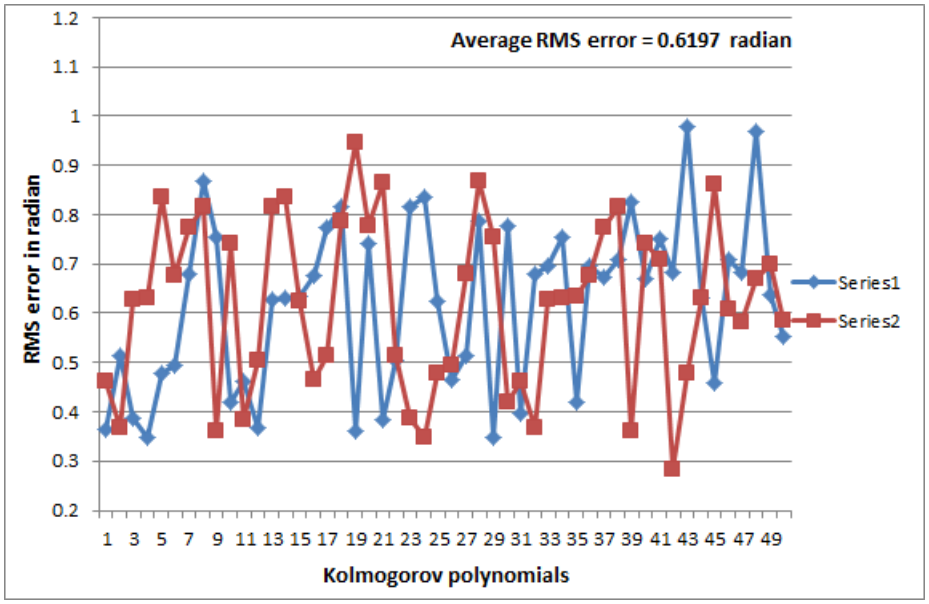

Figure 4. 6: RMS wave-front error between input and output phase screen of Kolmogorov polynomials.

4.5 Experimental Details of wave-front compensation

A 15 mW He-Ne laser (λ=632.8 nm) is used as a source of light. Neutral Density Filter (NDF) is used to control the light intensity. Spatial Filter (SF) which removes the laser speckle noise is used for beam cleaning. D1and D2 are two collimating lenses of focal length 25 cm. T1 imaging lenses of focal length 12.5 cm is used to reduce the size of collimated beam. The beams are incident on CDM which is a continuous MEMS Deformable Mirror (Multi-DM) from Boston Micromachines with 140 actuators. It has a maximum stroke of 5.5 μm having aperture area of 4.95mm with actuator pitch of 450 μm. This CDM acts as a turbulent wavefront generator. The reflected beam is allowed to pass T2 and T3 of focal length 12.5 cm which are in 4f geometry. The 4f geometry removes high frequency components. The reflected beam from the CDM is passed through SHS before it is imaged on sCMOS camera which is placed at the image plane [16]. The schematic setup for experimental measurement of wave-front compensation is shown in Figure 4.7.

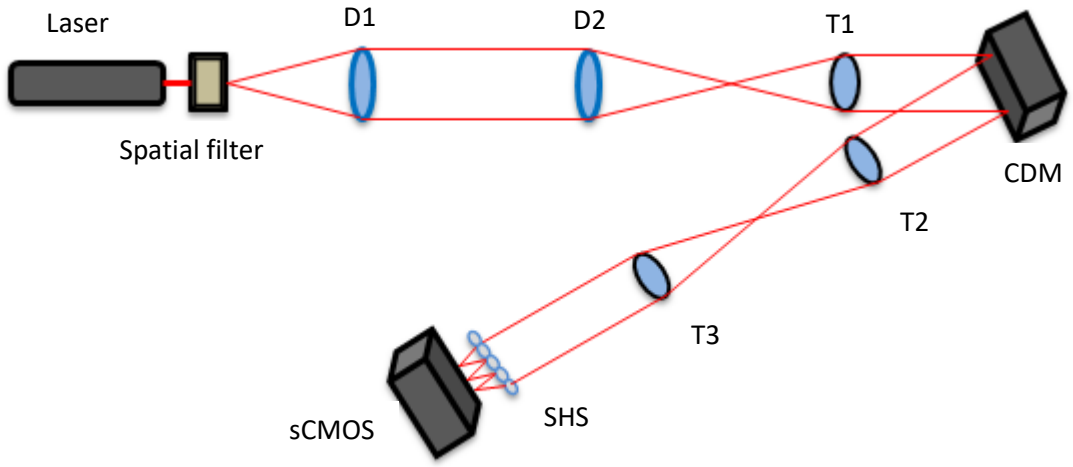

Figure 4. 7: Schematic setup for the experiment measurement of wave-front compensation

The SHS used in this experiment has 100x100 sub-apertures having equal diameter and pitch of 200 μm. The focal length of the SHS is 40mm. The SHS has f-number

200. It has theoretical full-width half maximum (FWHM) spot size of approximately 6x6 pixels on the detector. In order to sense the entire CDM active area, the minimum number of sub-apertures to be used must be greater than the ratio of beam diameter to pitch of microlens. Hence, a small portion of 25 x 25 sub-aperture are used for the SHS. This area corresponds to ≃ 775 x 775 pixels on the sCMOS. Each sub-aperture corresponds to ≈ 31 pixels on the sCMOS. To avoid sub-aperture cross talk, the maximum voltage applied to the actuators of the CDM is kept below 100V.

The sCMOS frames are acquired as matrices using the Matlab image acquisition toolbox in real-time. In the absence of the microlens array and with zero voltages on all the CDM actuators, a background image (BKD) is taken. Another reference pattern (REF) is taken by placing the mircolens array in front of the sCMOS. A low-resolution higher order Zernike mode (Z_6^2) is addressed on the CDM actuators. The shifted spot pattern (SP) is then recorded. The maximum grayscale in the image corresponds to 100V to avoid cross talk and minimum grayscale is 0V. Each of the matrices BKD, REF and SP are of size 775 x 775, since we are using a SHWS sensor with 25x25 sub-apertures and each sub-aperture corresponds to 31x31 pixels on the CMOS. BKD is subtracted from REF and SP. Simple CoG centroiding is performed on the resulting spot pattern images and the local wave-front tilts are determined. Figure 4.8 shows SH-spots pattern acquired from Matlab toolbox.

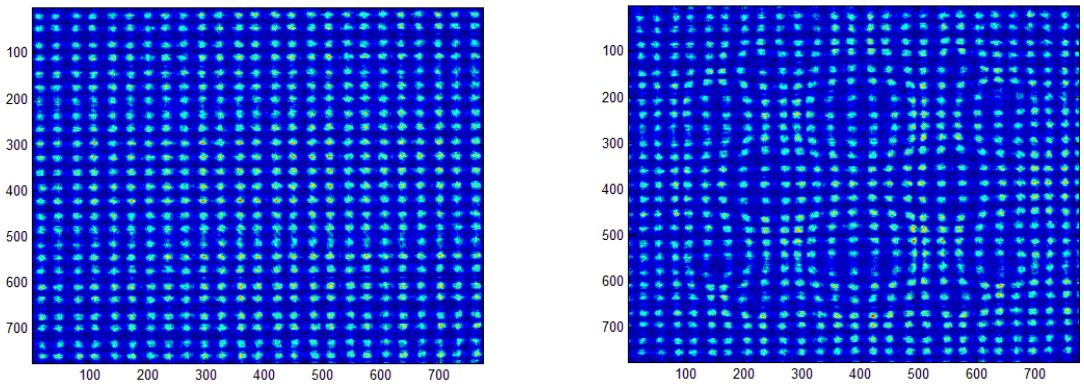

Figure 4. 8: (a) REF SH-spot pattern, (b) shifted SP pattern. Size 775 x 775 pixels, 25 x 25 no of SH-spots each size of 31 pixels

Low resolution Zernike polynomials are given to the CDM actuators and corresponding shifted SH-spots pattern is recorded. Using wave-front reconstruction algorithm, phase is reconstructed from the shifted SH-spots pattern. Figure 4.9 shows input Zernike polynomials and output from the SH-spots.

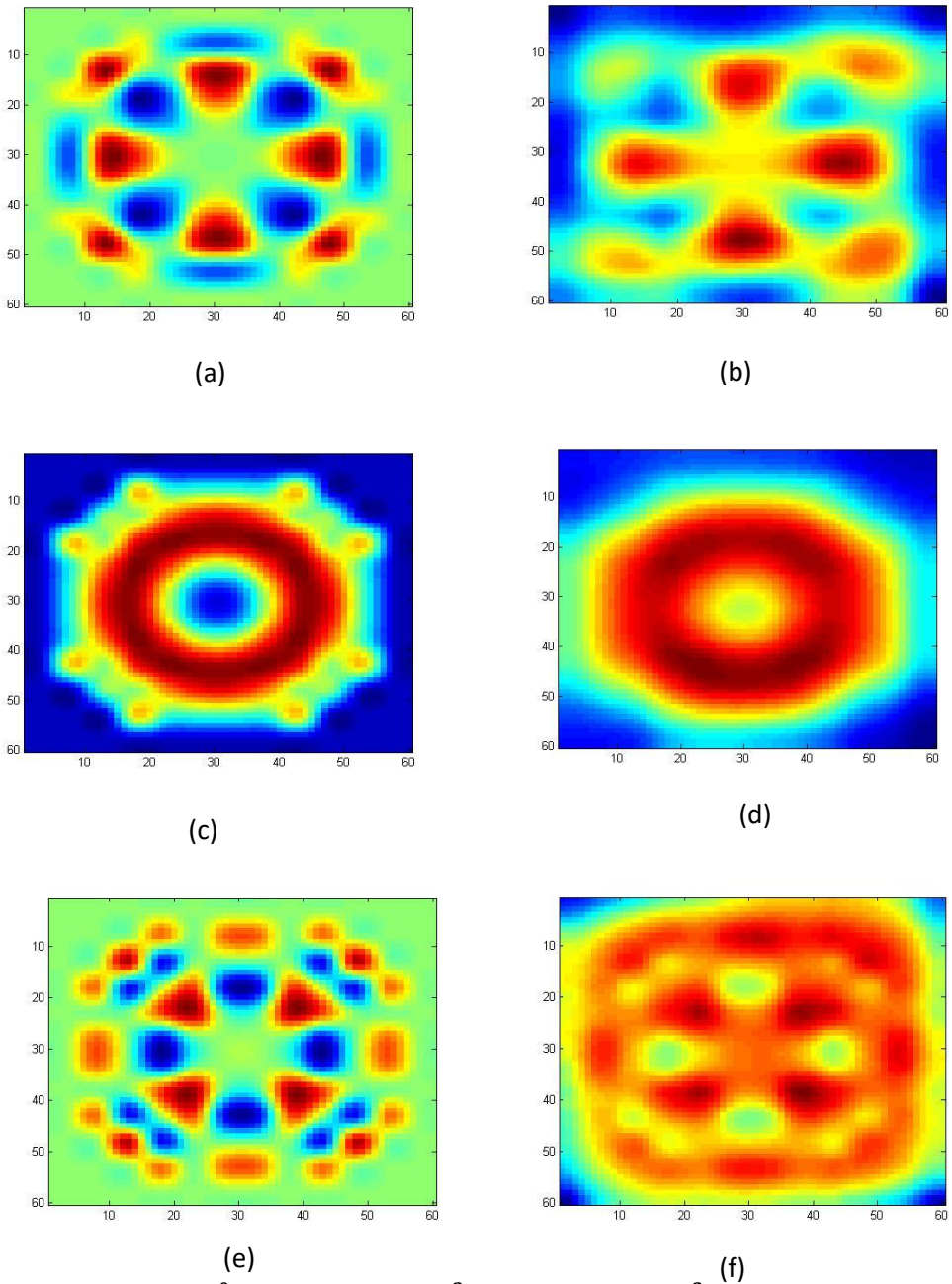

Figure 4. 9: (a) Zernike input Z_4^0 (c) Zernike input Z_4^2, (e) Zernike input Z_6^2, (b),(d),(f) corresponding output from shifted SH-spot pattern

Experiment for wave-front compensation is carried with 65 number of Zernike polynomials for 5 times. Correlation coefficient between input Zernike polynomials and reconstructed output Zernike polynomial is found that for all the cases. The average correlation coefficient found to be 0.74. RMS wave-front error of input and output in phase is below 0.3 radian. Figure 4.10 shows the relation between correlation coefficients between input Zernike polynomials and output Zernike polynomials with corresponding polynomials.

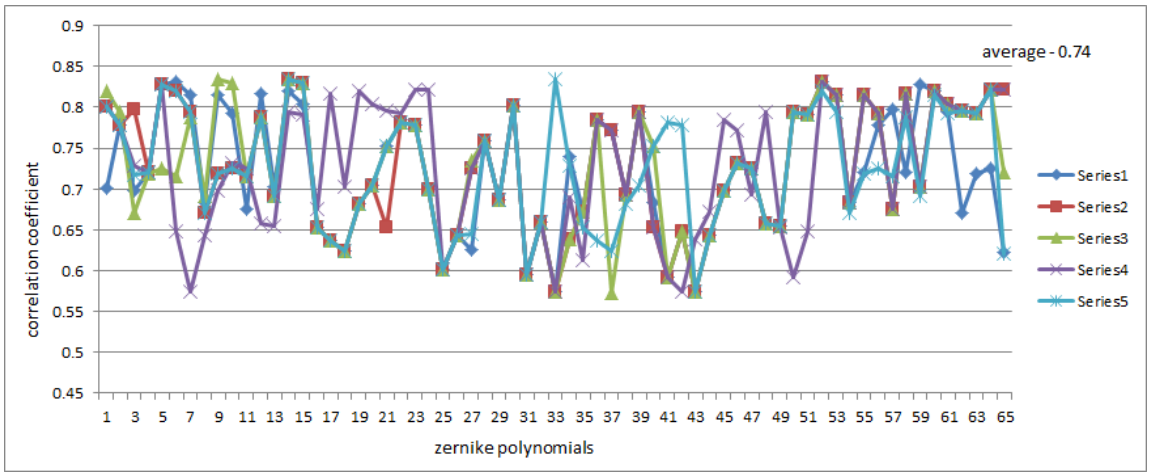

Figure 4. 10: Correlation coefficient for Zernike polynomials

4.6 Conclusions

In this chapter, wave-front sensing principle with Shack Hart-mann wave-front sensor is discussed. A control matrix ‘A’ is created in Matlab platform. This matrix is the heart of wave-front reconstruction algorithm. Its performance is tested with simulated Kolmogorov phase screen. Average correlation coefficients between input and output Kolmogorov phase screen is found to be 0.71. The average RMS wave-front errors between input and output Kolmogorov phase screen are also below 1 radian. Hence wave-front reconstructed algorithm is performing well for simulated phase screen. Its performance is tested using SHS in real time. The average correlation coefficients between input Zernike polynomials and output Zernike polynomials from SH-spots are found to be 0.74.

Bibliography

[1] M. A. Vandam, "Wave-front sensing for Adaptive Optics in Astronomy," University of Canterbury, 2002.

[2] F. Roddier and G. Rousset, "Wave-front sensor," in *Adaptive Optics in Astronomy*, Cambridge, Cambridge University press, 1999, pp. 91-130.

[3] G. Yoon, "Wavefront Sensing and Diagnostic Uses," in *Adaptive Optics for Vision Science Principles, Practices Design, and Applications*, JOHN WILEY & SONS, INC., PUBLICATION, 2006, pp. 63-79.

[4] A. Vyas, M. . B. Roopashree and B. R. Prasad, "Performance of centroiding algorithms at low light level conditions in adaptive optics," in *International Conference on Advances in Recent Technologies in Communication and Computing*, 2009.

[5] D. L. Fried's, "Least square fitting a wave-front distortion estimate to an array of phase difference measurements," *J. Opt. Soc. Am,* vol. 37, p. 370, 1977.

[6] R. H. Hudgin, ""“Wave-front reconstruction for compensated imaging"," *J. Opt. Soc. Am,* vol. 67, p. 375, 1977.

[7] W. H. Southwell, "Wave-front estimation from wave-front slope measurements," *J. Opt. Soc. Am.,* vol. 70, p. 998, 1980.

[8] J. Herrmann, "Least-squares wave front errors of minimum norm," *J. Opt. Soc. Am,* vol. 70, pp. 28-35, 1980.

[9] K. R. Freischald and C. Koliopoulos, "Modal Estimation of a Wave Front from Difference Measurements Using the Discrete Fourier Transform," *J. Opt. Soc. Am,* vol. A 3, p. 1852 , (1986).

[10] R. J. Noll, "Zernike polynomials and atmospheric turbulence," *J. OP. Soc. Am.,* vol. 66,

pp. 207-211, 1976.

[11] R. Tyson, "Representing the Wavefront," in *Principles of Adaptive Optics*, Charlotte, USA, CRC Press, 2011, pp. 12-15.

[12] G. Yoon, "Wavefront Sensing and Diagnostic Uses," in *Adaptive Optics for Vision Science Principles, Practices,Design, and Applications*, A JOHN WILEY & SONS, INC., PUBLICATION, 2006, pp. 63-79.

[13] A. N. Kolmogorov, "The local structure of turbulence in incompressible viscous fluid for very large Reynolds number," in *Proceedings of the Royal Society of London*, 1991.

[14] F. Roddier, "The effects of atmospheric turbulence in optical astronomy," Cambridge Univerisity press, 1991, pp. 281-376.

[15] C. Rao, W. Jiang and N. Ling, "Spatial and temporal characterization of phase fluctuations in non kolmogorov atmospheric turbulence," *Journal of Modern Optics*, vol. 47, pp. 1111–1126,, 2000.

[16] M. B. Roopashree, A. Vyas and B. R. Prasad, "Influence Function Measurement of Continuous Membrane Deformable Mirror Actuators Using Shack Hartmann sensor," *AIP Conf. Proc.*, vol. 1391, pp. 453-455, 2011.

Chapter 5

WAVE-FRONT CORRECTIONS

This chapter discusses the concepts of deformable mirrors. It also discusses actuation principles of DM and Micro Electro-Mechanical System (MEMS) technology. The requirements set to the DM of an Adaptive Optics (AO) system come from the overall AO error budget is also calculated. DM is also characterized by evaluating its influence function and its performance with different wave-front is determined from its influence matrix.

5.1 Description of Deformable Mirrors

The resolution of ground based astronomical telescopes is severely limited by the aberrations introduced by the atmosphere during optical beam propagation. To overcome this problem, H. W. Babcock first proposes in 1953 the concept of adaptive optics. It consists in placing an optical corrector in a pupil image plane and in controlling in real time its shape to compensate for the aberrations introduced by the atmosphere. This was the first proposal of Deformable Mirror (DM). This component was slow, chromatic and very sensitive to environment.

To characterize the different concepts it is useful to discuss the main parameters of a DM. In particular, the Number of Actuators, the Stroke, the Size and the Temporal Bandwidth. The Linearity and Hysteresis and the shape of the Influence Function (IF) of each actuator have only a second order impact on performance.

Number of actuators: The fitting error is defined to be the component of the wave aberration that the DM cannot fit since phase is continuous and DM is discrete in nature. The fitting error is given by the equation

$$\sigma^2_{fitting} = k(\frac{D}{r_0})^{\frac{5}{3}} N^{\frac{-5}{6}} \quad (62)$$

with D the pupil diameter and r_0 the so-called Fried's parameter. N is the maximum number of DM actuators and k is a factor which depends on the shape of the DM influence function.

Stroke: The maximum deformation of a DM defines its stroke. The required stroke is independent of the wavelength of observation and increases with the size of the primary mirror of the telescope. The maximum relative displacement than can be imposed between two actuators is called the inter-actuator stroke and determines the maximum amplitude of correction to the optical mode with the highest spatial order.

Size: The optical telescope transforms a collimated beam of light with the diameter of a primary mirror D, on a collimated beam of light with the diameter of a DM, D_{ap}

Temporal Bandwidth: The bandwidth of correction required by atmospheric turbulence depends solely on the wavelength of observation and on the speed of the wind. In the visible, it can attain about 400 Hz and in the NIR 60 Hz.

5.2 Actuation Principles

The development of DMs for AO systems started in the early 1970s mainly driven by military contracts. Many different concepts were proposed and studied at that time; the most popular ones were based on the use of piezoelectric materials. Latter in the 1990s a new category of DMs appeared following the advent of MEMS technology: very compact, light weighted, low drive voltage hardware which can take advantage of economies-of-scale to bring significant cost reductions. Different kinds of DM and its actuation principle are given in Figure.5.1

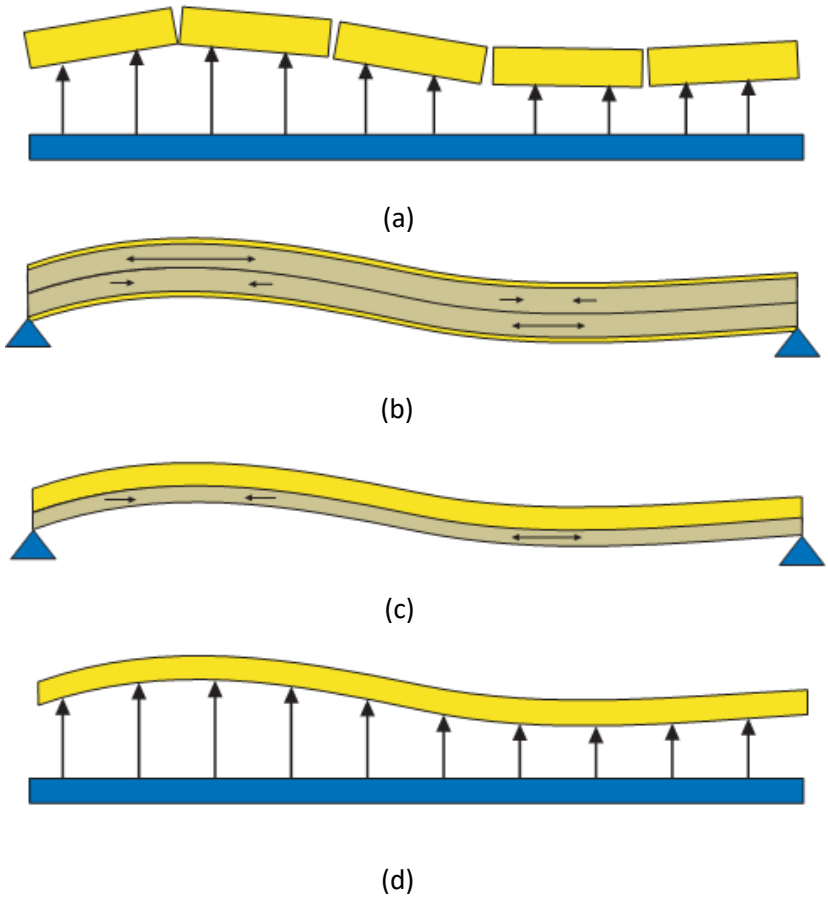

Figure 5. 1: Actuation principles of deformable mirrors (a) Segmented mirror, (b)Bimorph , (c) Monomorph and (d) Piston Actuated.

A brief description of DMs type are given below.

5.2.1 Segmented Mirrors*:* One way of adjusting the shape of a mirror consists of discretizing it into independent segments for which position and orientation are actively controlled.

5.2.2 Bimorph Mirrors: The bimorph principle of actuation is two active layers, each coated by electrodes on both faces, are bonded together, and an electrical field E is applied through them in the direction perpendicular to the plane of the mirror.

5.2.3 Monomorph Mirrors: The out-of-plane bending of the mirror originating from in-plane actuation can also be effectively achieved by utilizing one active layer adherent to a passive substrate Fig. 5.1(c). This configuration preserves the advantages of simplicity, low-cost, robustness and low weight of bimorph mirrors.

5.2.4 Piston Actuated Mirrors: Figure 5.1 (d) presents the concept of an optical surface deformed under the action of out-of-plane forces. This type of actuation can be achieved through different physical principles like Piezo-stacked actuators, Voice-coil magnetic actuators, Electrostatic membrane mirrors, and Contact MEMS mirrors.

5.2.5 MEMS : During the 1990s, the advent of the Micro Electro-Mechanical System (MEMS) technology accelerated the development of a new generation of DMs. MEMS DM manufacturing process is based on silicon computer industry technology which allows reducing the manufacturing cost. Most of these concepts are based on the use of a thin mirror membrane attached to an intermediate flexible support actuated by electrostatic or electromagnetic fields. They all share the characteristics of sub millimeter pitch, low power consumption, capabilities to very high number of actuators and low mass.

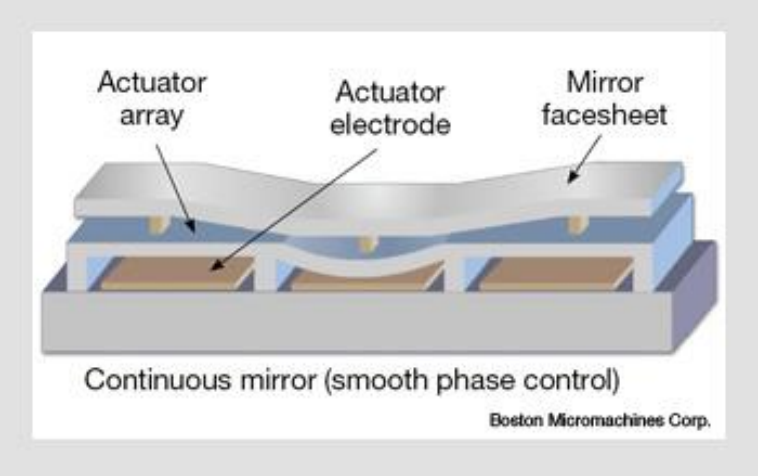

Figure 5. 2: This cross-section displays the elements of a 1×3 actuator array within an electrostatically actuated microelectromechanical systems (MEMS) deformable mirror.

Depending on the electro-mechanical concept at play, the internal features of the DM can be different. When actuation is based on electrostatic fields, the displacement of the membrane is proportional to the square of the applied voltage and requires applying up to 200 V to get a 5 to 8 µm stroke.

The Boston Micromachines Corporations Multi-DM deformable mirror (BMC DM) used in this setup has a continuous gold plated membrane, operated by piston actuators (with one degree of freedom). A close-up of the mirror's surface is shown in Figure 5.3 and the interface box is shown in Figure 5.4.

Figure 5. 3: Packaged DM Front with protective window (left) and Back with electrodes (right)

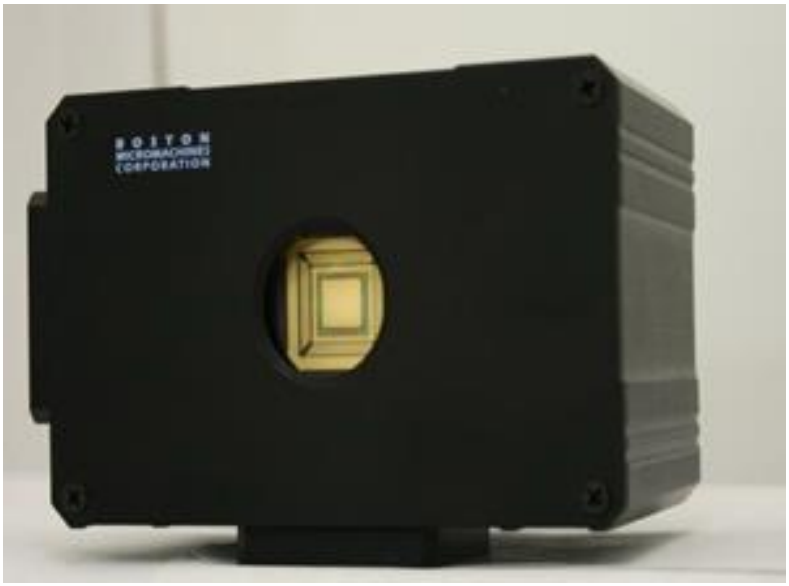

Figure 5. 4: DM Interface Box

5.3 Applied voltage to actuator response

The DM which is a continuous MEMS Deformable Mirror (Multi-DM) from Boston Micro-machines with 140 actuators. The actuators having pitch of 450μm with aperture area of 4.95mm^2. It has a maximum stroke of 5.5μm with maximum voltage of 300V. 16-bit Hexadecimal data is entered into DM through LinkUI software as voltages to the actuators. Each data number as a single stroke corresponds to 18mv being applied to the CDM. The stroke of actuator doesn't follow a linear relationship with applied voltage. It follows a square relationship by the following Eq. 63.

$$y = 5.1853x^2 - 17.61x + 20.128 \tag{63}$$

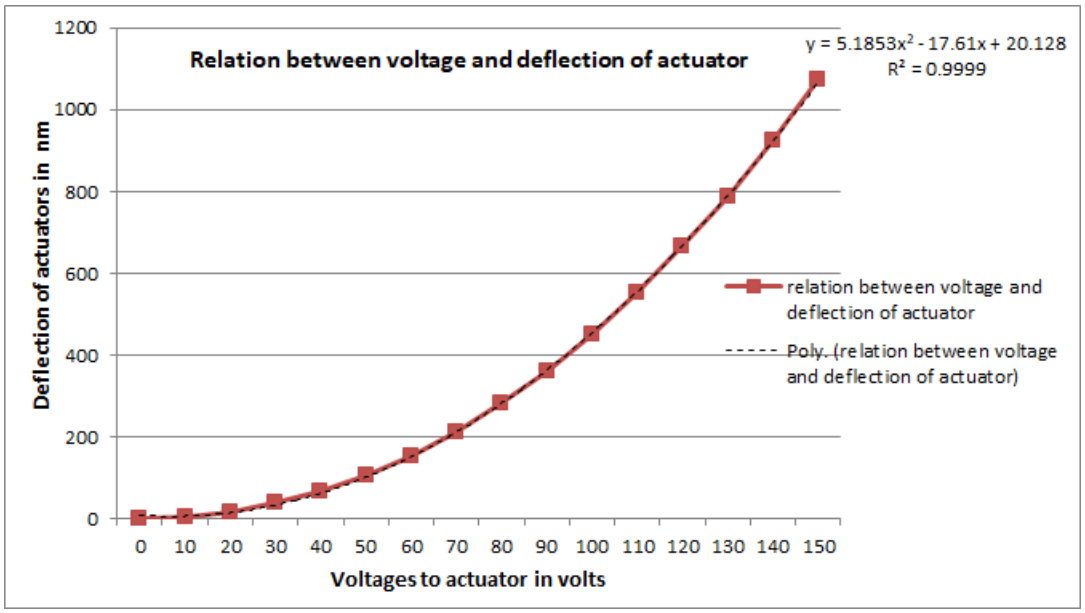

Figure 5. 5: The square relation between voltage and deflection of actuator.

5.4 Influence Function measurement

Wave-front correctors alter the phase profile of the incident wave-front by changing the physical length over which the wave-front propagates or the refractive index of the medium through which the wave-front passes. Most wave-front correctors are based on mirror technology and impart phase changes by adjusting their surface shape (i.e., change their physical length while keeping the refractive index constant) [1]. DM of this type have a continuous mirror surface whose profile is controlled by an underlying array of actuators [2]. Pushing one actuator produces a localized Gaussian-like deflection of the mirror surface, termed the influence function. The deflection extends to adjacent actuators, where it typically changes the surface height by 10 to 15% of the peak deflection. This deflection is commonly referred to as the coupling coefficient, as it describes the degree of cross-coupling between actuators. A Continuous Membrane Deformable Mirror (CDM) has minimal edge diffraction. Since in most applications, the wave-fronts to be corrected by the DM are continuous in nature, it is advantageous to use the CDM with precise calibration. [3].

5.5 Experimental Details for Influence function

In order to find the influence function an experimental setup is shown in Figure 5.6. A 15 mW He-Ne laser (λ=632.8 nm) is used as a source of light. Neutral Density Filter (NDF) is used to control the light intensity. Spatial Filter (SF) which removes the laser speckle noise is used for beam cleaning. D1and D2 are two collimating lenses of focal length 25 cm. T1 imaging lenses of focal length 12.5 cm is used to reduce the size of collimated beam. The beams are incident on CDM which is a continuous MEMS Deformable Mirror (Multi-DM) from Boston Micro-machines with 140 actuators. This CDM acts as a turbulent wave-front generator. The reflected beam is allowed to pass T2 and T3 of focal length 12.5 cm which are in 4f geometry. 4f geometry removes high frequency components. The reflected beam from the CDM is passed through SHS before it is imaged on SCMOS camera which is placed at the image plane [5]

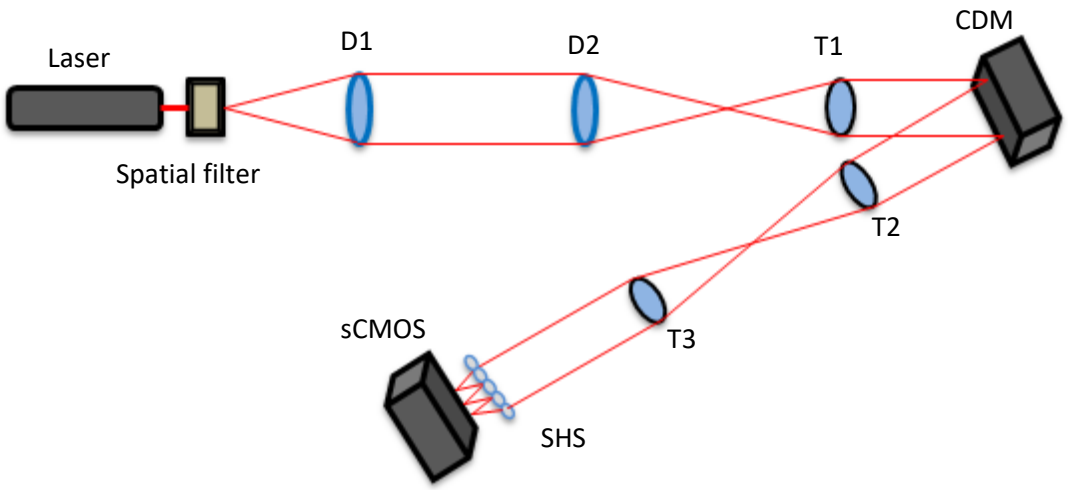

Figure 5. 6: Schematic setup for the experiment measurement of CDM influence function.

The experimental setup used here is shown in Figure 5.7. The imaging camera is a high resolution low noise CMOS camera from Photonic Science having sensor size of 1920 x 1080 with each pixel 6.5 µm. The experiment is carried out in a dark room keeping the surrounding temperature as minimum as possible. The dark noise in found out to be 8e-. The dark noise is subtracted from an image using dark frames (BKD). The experiment is carried out with an exposer time of 100ms. Average value of SNR of SH-spots is 10, which is sufficient to reduce the photon noise. The camera features high-speed read-out of the sCMOS sensor at 50 MHz. In most applications, 50 MHz is the best choice as it gives slightly lower readout noise. This results in a maximum frame rate of approximately 16 Hz at 50 MHz with readout noise as low as 1.2e-.

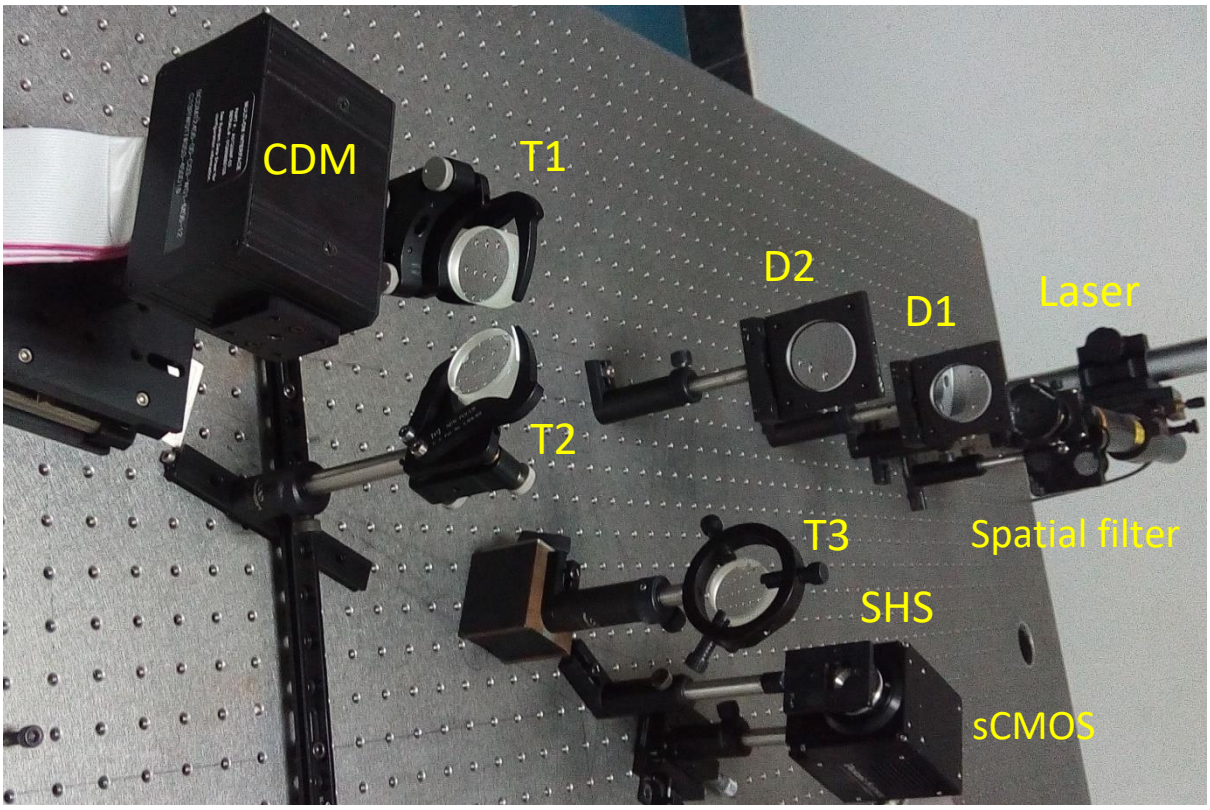

Figure 5. 7: Experimental setup for measurement of CDM influence function.

The SHS used in this experiment has 100x100 sub-apertures having equal diameter and pitch of 200 µm. The focal length of the SHS is 40mm. The SHS has f-number 200. It has theoretical full-width half maximum (FWHM) spot size of approximately 10x10 pixels on the detector. In order to sense the entire CDM active area, the minimum number of sub-apertures to be used must be greater than the ratio of beam diameter to pitch of microlens. Hence, a small portion of 25 x 25 sub-apertures are used for the SHS. This area corresponds to ≃ 775 x 775 pixels on the sCMOS having a dimension of 4.9mm^2. Each sub-aperture corresponds to ≈ 31 pixels on the sCMOS [6].

Influence function is a measure of the response of the CDM surface when a known voltage is applied to a single CDM actuator and a constant bias voltage is applied to all the other actuators. A specific voltage to actuator of interest(p) and reference voltage

of 0V applied to other actuators. The influence function is calculated from the SHS slopes with Fried's geometry. When a voltage of less than 30 V is given to any actuators, the corresponding shift in the SH-spots is very less. Since the deflection in the actuators are less than 20nm the wave-front reconstructed from the SH-spots is less than 0.3 radian. Figure 5.8(a) shows the wave-front reconstructed from SH-spots. When a voltage of more than 110 V is applied to any actuator, the cross talk among SH-spots increases in the image plane which makes it difficult to reconstruct wave-front from SH-spots. A voltage of more than 110 V when given to any actuator, the SH-spots cross talk in the image plane. Which results difficult for reconstruction of wave-front from the SH-spots Figure 5.8(b) shows the section of SH-spots pattern when 110 V applied to an actuator.

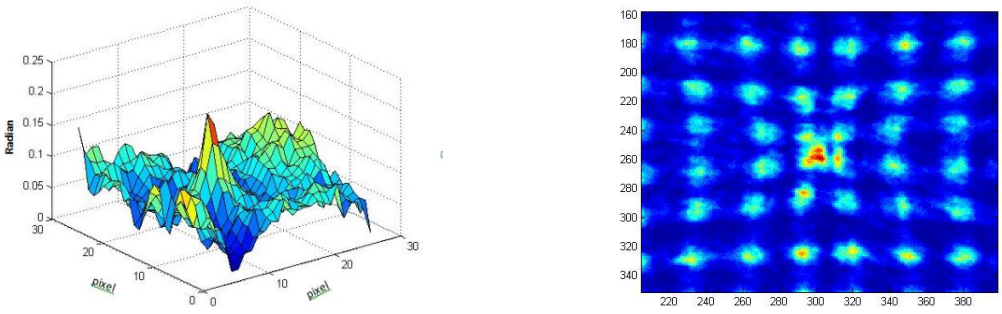

Figure 5. 8: (a) Reconstructed wave-front when 30 V is applied to an actuator. (b) SH-spot pattern for 110 V

Hence, the influence function has to be chosen at a voltage lying between 30 V and 110 V to avoid cross talk in the SH-spots in the image plane. Three sections of the square relation between voltage applied to actuator and deflection with centre voltages 45 V, 65 V, 85 V are plotted in Figure 5.9.

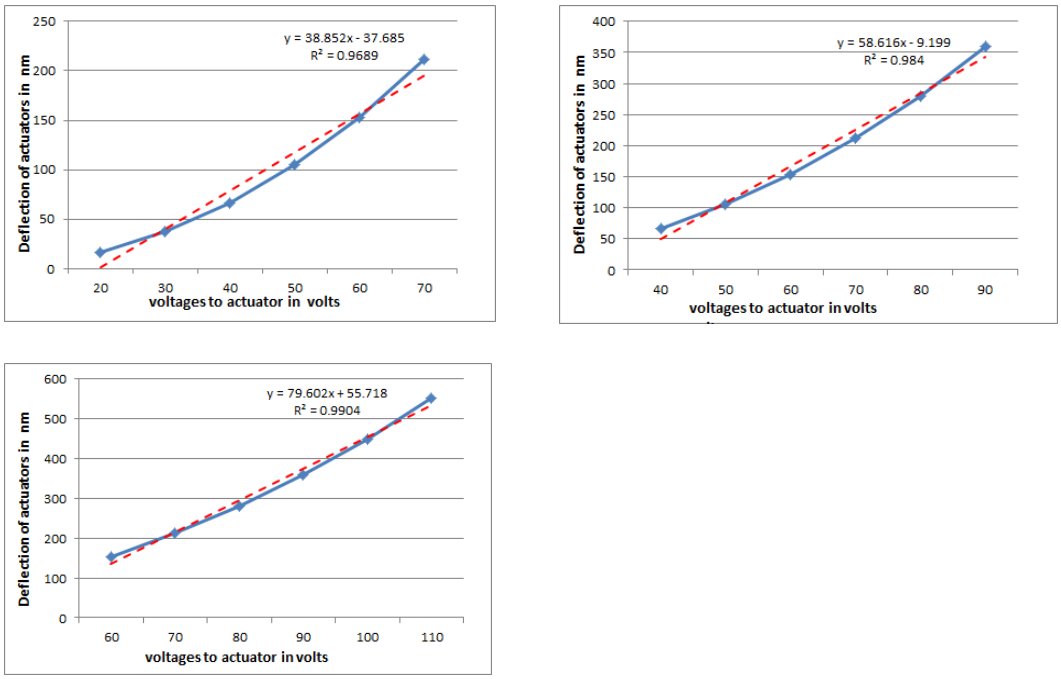

Figure 5. 9: Shows curve between voltage applied to actuator and deflection in nm with voltage centred at (a) 45V, (b) 65V, (c) 85V

A straight line is fitted in each of the curve. The R-squared value increases at the tail end of the square curve. i.e R-squared value is more for centre voltage 85 V and minimum for centre voltage of 45 V. Influence function for 45 V will not be feasible since the R-squared value is less compared to the other two voltages and the minimum voltage is 20 V. The reconstruction of wave-front from the SH-spots will be negligible. Though influence function at 85 V will give better R-squared value compare to other two, due to cross talks of SH-spots at higher voltages its too not feasible. Hence influence function at 65 V gives a better result compared to other two. The R-squared value covers a range of voltage values beginning from 40 V to maximum voltage of 90 V.

5.6 Influence function calculation from SHS slopes

The CDM actuators are numbered by using an index ‘p’. Influence function of a single CDM actuator is measured by applying a specific voltage to actuator of interest(p) and reference voltage of 0V applied to other actuators. The influence function is calculated from the SHS slopes with Fried’s geometry. Comparative performance of different geometry is done initially. The SHS slope represented by a column vector S_p (x slopes followed by y slopes). The CDM surface deformation matrix W_p is evaluated. This is repeated for all possible values of ‘p’ i.e. for all 140 actuators. For SHS a specific voltage of 65 V is given. The maximum voltage is limited to 110 V as beyond this voltage leads to SH spot cross talk. Since 25×25 subapertures were used, the length of the measured slope vector S_p is 1876. The measured influence functions for the edge, penultimate and central actuators for SHS1 are shown in Figure 5.10. Influence functions for 45 V and 85 V is also determined.

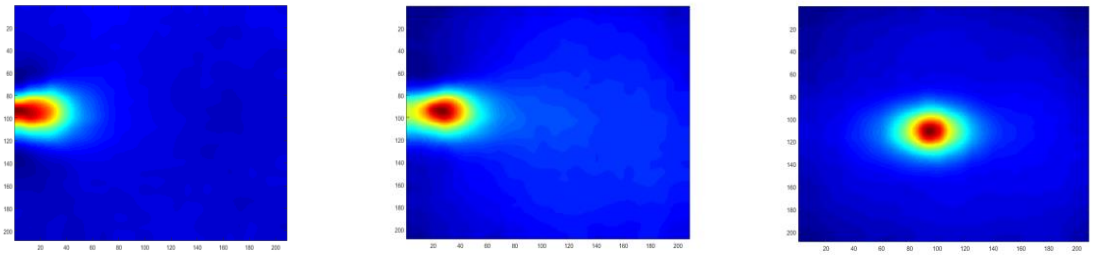

(a) (b) (c)

Figure 5. 10: Reference voltage = 0 V, Voltage applied = 65 V, size in pixels: 200×200, number of subapertures - 25×25. Measured Influence function for (a) edge actuator 70, (b) penultimate actuator 71, (c) centre actuator no 65 and its reconstruction from SHspots.

5.7 Measurement of Slope Influence Matrix

The slope influence matrix is the convergence of all actuators influence function. This matrix 'I_{65}' relates the measured slopes (S) and the voltages applied to the actuators as per the below equation.

$$S = I_{65}\phi \tag{64}$$

where, ϕ is a column vector containing the applied voltages to the CDM actuators and S is the slope vector. A single column of the interaction matrix is given by the ratio, $\frac{S_p}{V}$ for an actuator 'p' and hence the slope influence matrix,

$$I_{65} = \left[\frac{S_1}{V} \frac{S_2}{V} \frac{S_3}{V} \ldots \frac{S_{144}}{V} \right] \tag{65}$$

In order to efficiently address a wave-front on the CDM, the voltages that must be applied to the actuators are given by the formula.

$$\phi = I_{65}^{-1} S = CS \tag{66}$$

'C' is called control matrix which is determined by taking pseudo inverse of the matrix I [6]. For SHS the first term of the Eq. (61) is obtained by giving a voltage of 65 V to actuator 1. Corresponding shift pattern of SH spots is recorded using sCMOS camera. The first column vector length is 1876x1 which is repeated for all 144 actuators. Hence, the size of 'I_{65}' matrix is 1876x144. Similarly I_{45} , I_{85} , matrices are also determined.

A low-resolution higher order Zernike mode (Z_6^2) is addressed on the CDM actuators and it's shifted spot pattern (SP) is recorded. The wave-front is reconstructed from this

shifted SP. The RMS wave-front error between input wave-front and output wave-front is determined. Figure 5.11 shows for all the cases. The correlation coefficients between input Zernike polynomial and output wave-front from the SH-spots pattern is found to be 0.745. The RMS wave-front error between input and output Zernike polynomial is found to be 0.48 radian.

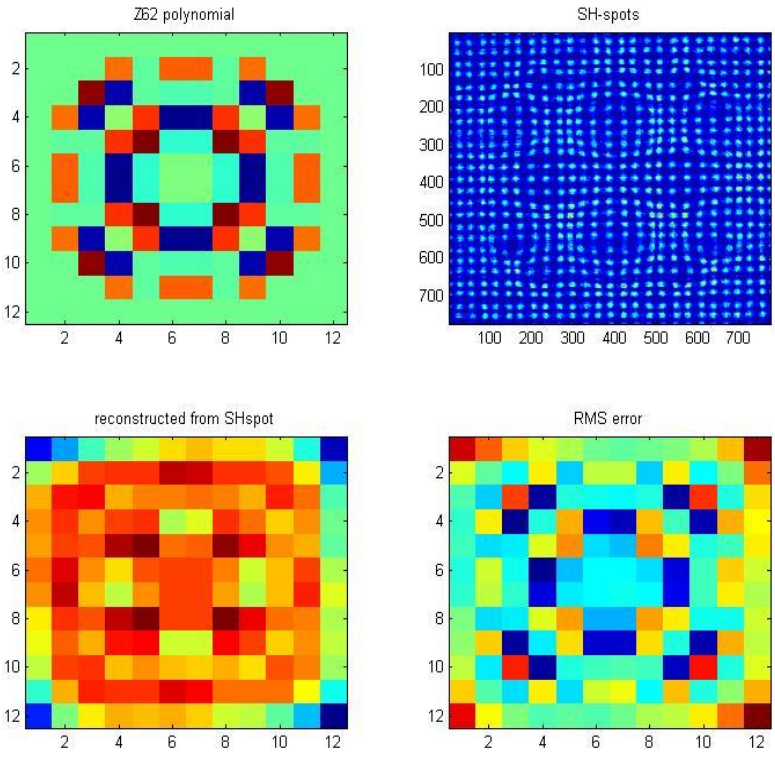

Figure 5. 11: (a) Input Zernike polynomial (Z_6^2), (b) Corresponding SH-spot pattern, (c) Output from SH-spot, (d) RMS wavefront error

It is repeated for other higher order Zernike polynomials too. Correlation coefficients between input Zernike and output wavefront are also calculated for higher order Zernike polynomials. This process is repeated for 3 times and found that the average correlation coefficients is 0.712 between input and output wavefronts at I_{65} as shown in Figure 5.12.

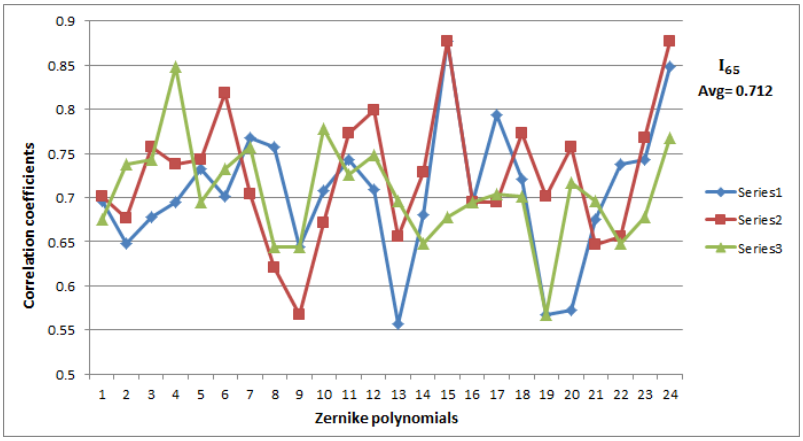

Figure 5. 12: Correlation coefficients between input and output wave-front for various Zernike polynomials.

The correlation coefficients between input and output wave-fronts for higher order Zernike polynomials are found out for I_{45}, I_{85} also shown in Figure 5.13.

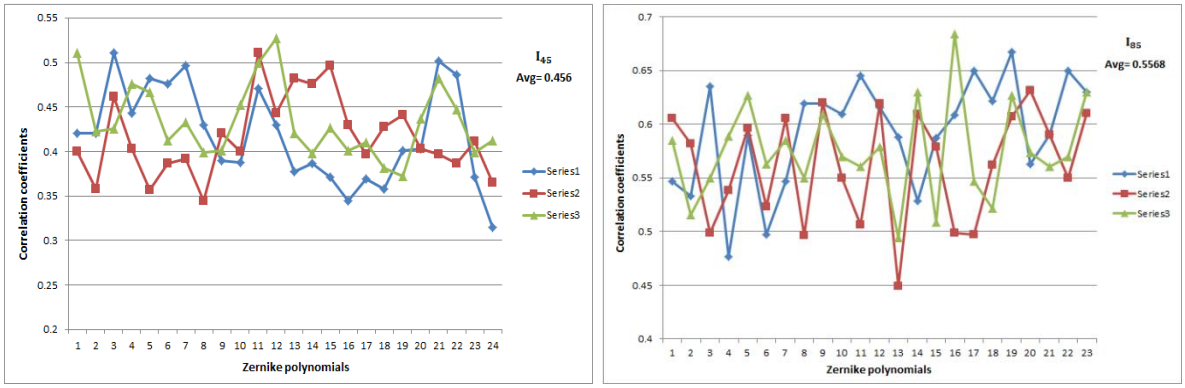

Figure 5. 13: Correlation coefficients between input and output wave-front for various Zernike polynomials at (a) I_{45}, (b) I_{85}

From Figure 5.13 it is observed that, the average correlation coefficients between input and output wave-fronts for higher order polynomials are less at I_{45}, I_{85} as compare to I_{65}. Hence, I_{65} is found to be the best influence matrix for wave-front reconstruction.

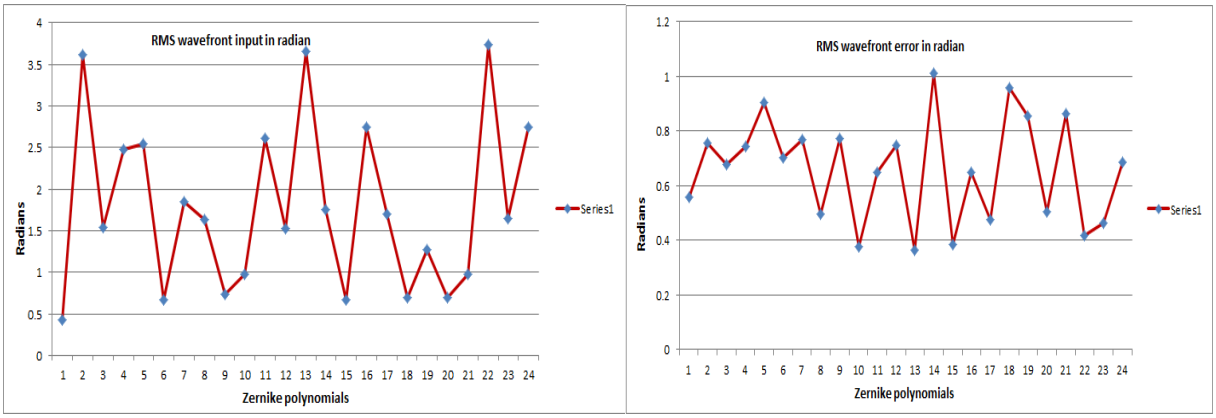

Figure 5. 14: (a) Shows the input Zernike polynomials in radian, (b) wave-front error between input and output wave-front of Zernike polynomials in radian.

The higher order Zernike polynomials which are given as input to the CDM, are in the range of 0.5 radian to 4 radian. The RMS wave-front error between input Zernike polynomial and output reconstructed from the SH-spots are found to be less than 1 radian.

Performance of slope influence matrix (I_{65}) is also verified with Kolmogorov polynomials. The Fried's parameter (r_0) is set to 15 cm which determines the seeing cell size. The outer scale L_0 is set to 20 m that corresponds to the size of the largest turbulence cell and the pupil diameter D is set to 2 m.

The input Kolmogorov polynomial having amplitue in the order of 3 radian is created using Matlab. It is then projected to the CDM actuators as voltages. The corresponding SH-spot pattern is recorded. From the shifted SH-spot pattern the wave-front is reconstructed. Correlation between input and output wave-front is found to be 0.712.

The RMS wave-front error between input and output wave-front is 0.782 radian. An example of Kolmogorov polynomial with input and output phase screen is given in Figure 5.15 with its stroke map and RMS error.

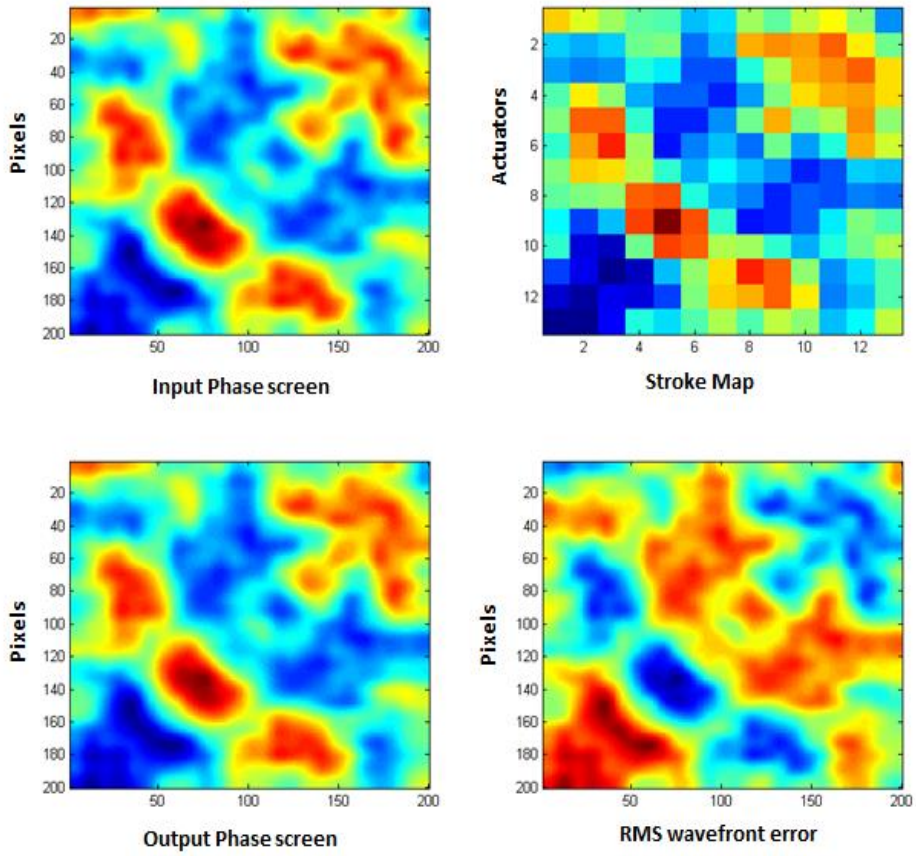

Figure 5. 15: (a) Original sample phase screen ϕ generated with Matlab, (b) stroke map obtained by projection of the original phase ϕ onto the influence functions,(c) projection of the original phase screen ϕ onto the CDM, (d) Closed-loop RMS error measurement.

5.8 Conclusions

Influence function for the CDM actuators are calculated for all the three portions of the non-linear curve between voltages and its actuator. Influence function is determined for voltage values lying in the range 20-70 V, the reconstruction from SH-spots is not suitable since shift in SH-spots is less and for the voltage values in the range of 60-110 V SH-spots reconstruction is not feasible due to crosstalk between neighbouring SH-spots. Performance of influence function at 65 V is tested with several higher order Zernike polynomials and its average cross correlation coefficients found to be 0.7, where input of polynomials are in the range of 0.5 to 4 radians. The RMS wave-front error between input wave-front and output wave-front reconstructed from the SH-spots is found out to be below 1 radian for all Zernike polynomials as well as for Kolmogorov polynomials.

Bibliography

[1] J. PORTER, H. M. QUEENER, J. E. LIN and K. THORN, Adaptive Optics for Vision Science, A JOHN WILEY & SONS, INC., PUBLICATION, 2006.

[2] M. A. Dam, "Wavefront sensing for Adaptive Optics in Astronomy," 2002.

[3] R. Tyson, Principles of Adaptive Optics, New york: CRC Press, 2011.

[4] M. B. Roopashree, A. Vyas and B. . R. Prasad, "Influence Function Measurement of Continuous Membrane Deformable Mirror Actuators Using Shack Hartmann sensor," in *AIP Conf. Proc.*, 2011.

[5] M. B. Roopashree, A. Vyas and B. R. Prasad, "A Novel Model of Influence Function: Calibration of a Continuous Membrane Deformable Mirror," *ACEEE Int. J. on Control System and Instrumentation,* vol. 03, no. 02, March 2012.

[6] M. Booth, T. Wilson, T. Ota and S. Kawata, "Methods for the characterization of deformable membrane mirrors," in *APPLIED OPTICS,*, 2005, p. 44(24)..

Chapter 6

TEMPORAL BEHAVIOUR OF ATMOSPHERIC TURBULENCE

Simulation of the dynamic effects of atmospheric turbulence is essential in understanding, testing and effective implementation of adaptive optics systems. In this chapter, a small portion from a large wave-front is selected as the initial phase screen in the temporal evolution of a particular layer. The subsequent phase screens at later times are formed by translating the initially selected portion on the very large wave-front in a definite direction and well defined velocity. Wave-fronts are reconstructed dynamically and its correlation coefficients are determined with input wave-fronts. RMS wave-front errors are determined dynamically between input and output wave-fronts. A single layered turbulent medium is modelled in laboratory by using a trans-missive phase plate. The real-time wave-front measurements using the SHWS are used for turbulence characterization. In this chapter, the experimental evaluation of the wind speed measurement and its strength in radian from the phase plate is evaluated.

6.1 Introduction

Ground based telescopes produce images which are degraded by the refractive index fluctuations in the Earth's atmosphere. Several technologies were developed to read the shape of atmospheric wave-fronts that degrade the image quality in telescopes and compensate it in real time to obtain high resolution images. Adaptive optics has proved to be one of the most effective technologies to improve image quality in real time [1] [2]. Statistics of the refractive index fluctuations are modelled through the calculation of spatial and temporal correlations of atmospheric wave-fronts [3]. Image degradation can be understood by taking a close look at the degree of wave-front

distortion. Development of atmospheric aberration correction technologies require a good understanding of atmospheric turbulence statistics for device optimization [4] [5]. Therefore, wave-fronts following these atmospheric statistics are simulated and used in the evaluation of telescope optics.

Atmospheric turbulence is defined through the refractive index structure constant (C_h^2) and wind profile (wind velocity, v as a function of altitude, h). The performance of an adaptive optics system is dictated by a large number of atmospheric factors derived from C_h^2 and $v(h)$ including Fried's parameter (r_0), isoplanatic angle (θ_0), coherence time (τ_0) and instrumentational constraints like wave-front sensor induced error, wave-front corrector residual error and servo bandwidth (f) [6]. The complex correlation between these parameters makes the design of an adaptive optics system a challenging optimization problem [7].There exists significant temporal variability of Fried's's parameter and wind velocity which is also site dependent [8]. Hence, it is important to continuously monitor the turbulence parameters to maintain the consistency of performance in an adaptive optics system. In this chapter, concentration on fluctuations in wind velocity and its effects on adaptive optics system performance. It was shown that atmospheric wind velocity profile has a complex relationship with other adaptive optics parameters [9]. Wind velocity controls intensity variations and temporal frequency of wave-front fluctuations. Atmospheric statistics are determined by two important parameters, turbulence strength $C_h^2(h)$ and wind velocity $v(h)$. These metrics are a function of altitude from the surface of the Earth, 'h'. Hence it can be viewed as if the atmosphere is made up of infinite number of turbulence layers.

In most situations, it is enough to consider a finite number of discrete layers to closely depict the atmosphere [10]. Hence, few layers of simulating atmospheric wave-fronts are discussed. Fast Fourier techniques are used for the generation of large two-dimensional phase screens [11] [12]. The simulated phase screens are made up of a finite number of pixels.

To simulate temporally evolving wave-fronts, frozen in turbulence approximation is applied on individual layers. A very large wave-front (X_l of size $\boldsymbol{M}$ **x** $\boldsymbol{M}$ square pixels corresponding to layer *l*) with turbulence strength defined for a single layer is simulated as a first step. A small portion of this very large wave-front is selected as the initial phase screen (P_1^l (t = 0), 't' represents time) in the temporal evolution of this particular layer. The subsequent phase screens (P_1^l (t), i=2,3,...n) at later times are formed by translating the initially selected portion on the very large wave-front X_l in a definite direction and well defined velocity read from the wind velocity profile. The number of such phase screens generated is limited by the number of pixels on the large wave-front, X_l. If the size of $P_1^l(t)$ is $\boldsymbol{N}$ **x** $\boldsymbol{N}$ square pixels, then the maximum value 'n' can take is equal to ($\boldsymbol{M} - \boldsymbol{N}$ + 1). The time interval between two temporally adjacent phase screens is defined as: $\boldsymbol{\Delta T} = \frac{dl}{v}$, where v is the layer velocity and dl is the distance moved on the phase screen in a time $\boldsymbol{\Delta T}$. In the simulation of temporally evolving phase screens, $\boldsymbol{\Delta T}$ is kept a constant for all the layers and dl (representative of the number of pixels moved within $\boldsymbol{\Delta T}$ in accordance with the wind velocity of the layer 'l') is varied for different layers. The phase screens representing the evolution of atmospheric turbulence are finally obtained by superposing different evolving layers.

Figure 6.1 shows an evolving phase screen simulated using fourier technique by using a single layer with average wind speed = 5 m/s. Adjacent phase screen are temporally separated by 10 ms.

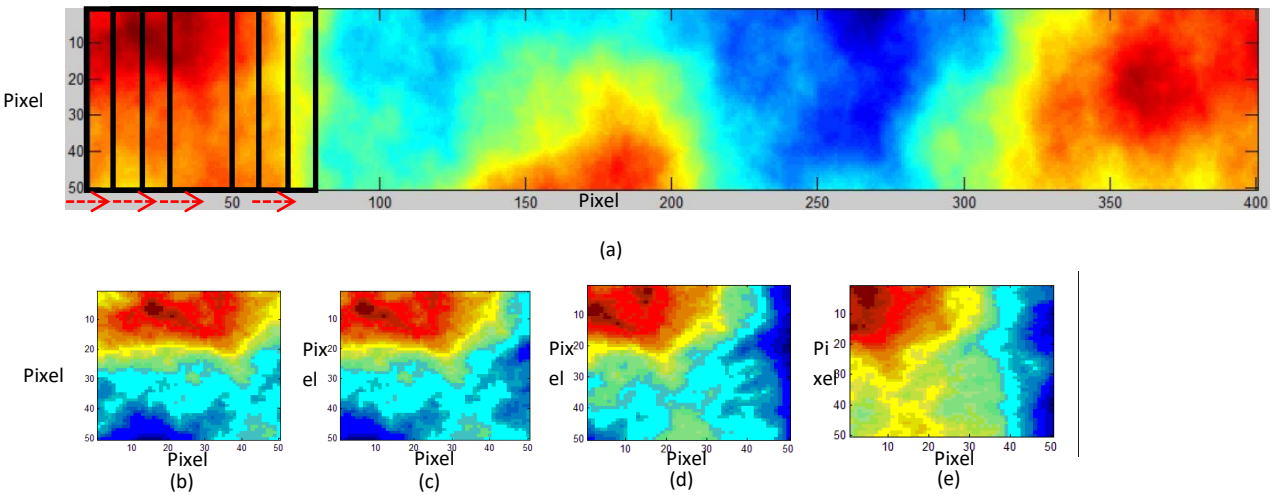

Figure 6. 1: Evolving Phase screens (1-8) simulated using Fourier technique by using a single layer with average wind speed = 5 m/s. Phase screen resolution : 50 × 50 pixels; r_0 = 0.1 m; Phase screen dimension :2 × 2 m^2; L_0 = 12 m. Adjacent phase screens shown above are ∼63 % correlated and temporally separated by ∼10 ms.

Each frame from the large wave-front is applied to the SH-spots as an input. From the shifted SH-spot patterns output wave-front is reconstructed continuously. The RMS wave-front errors are also obtained from the difference between input and output wave-fronts dynamically. A large Kolmogorov phase screen 200 x 200 is simulated using FFT method in Matlab platform. A section of 50 x 200 is chosen from the large Kolmogorov screen. 3-D representation of the cropped section of size 50 x 200 is given in Figure 6.2.

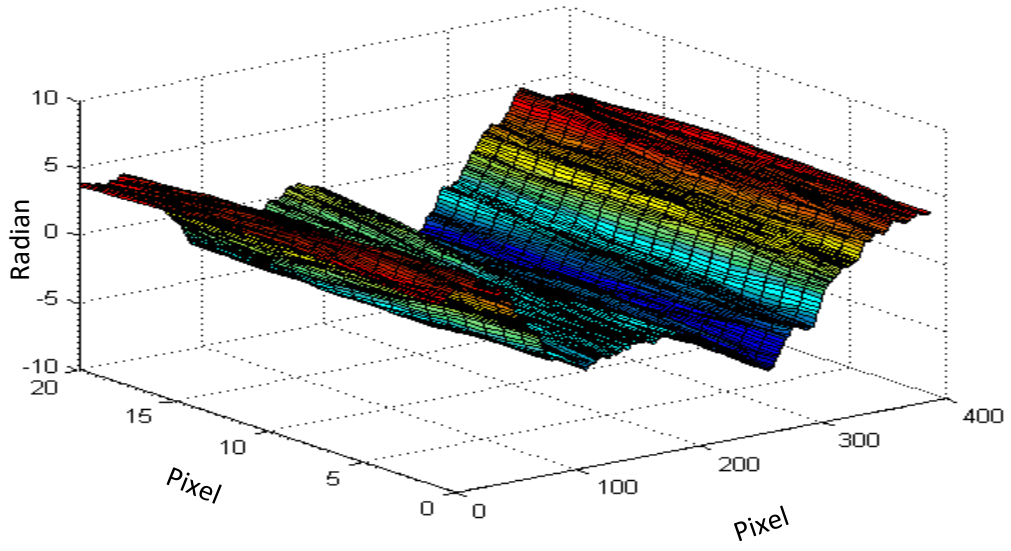

Figure 6. 2 A cropped section of 50 x 200 is chosen from a 200 x 200 phase screen

Each sub-frame of size 50 x 50 is taken from the cropped section and subsequent frames are formed by translating the initially selected portion on the very large wave-front X_l in a definite direction and well defined velocity read from the wind velocity profile. For each cropped section of 50 x 200 phase screen, total no of sub-frames of size 50 x 50 are 151 (*M-N+1*) can be formed. RMS wave-front error for each input and reconstructed wave-front is found out for sub-frames. Figure 6.3 shows snap shots of dynamic wave-front sensing for 3 random sub-frames from the cropped frame. Input wave-fronts and its output wave-fronts are shown with their RMS wave-front error for each sub-frames. This is repeated for 3 different Kolmogorov screen to check the accuracy of wave-front reconstruction algorithm in dynamic condition. The average RMS wave-front error is 0.42 radian is found. Figure 6.4 shows the plot between RMS in radian vs no of sub-frames.

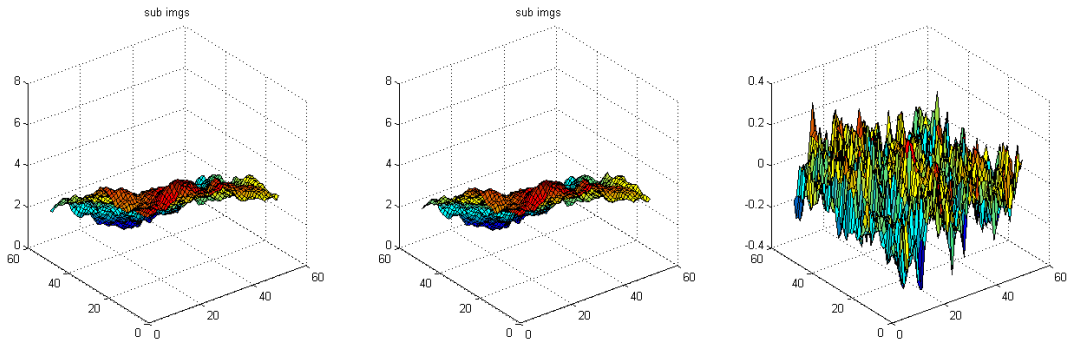

Sub-frame 1: (a) input wave-front,(b) output wave-front,(c)RMS error

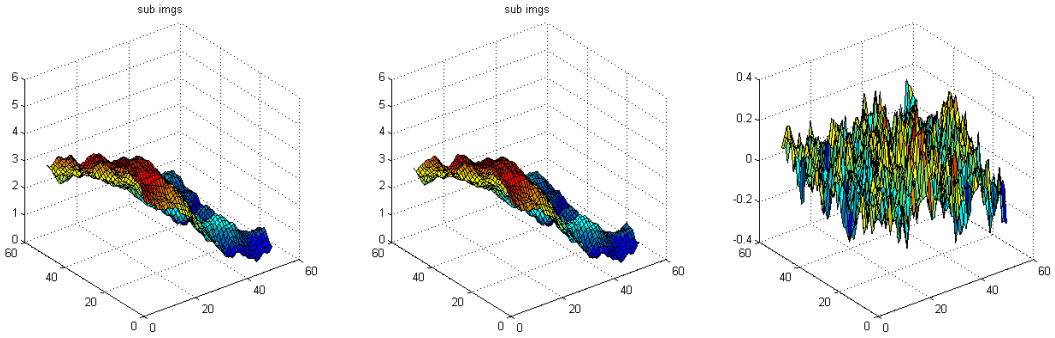

Sub-frame 2: (a) input wave-front,(b) output wave-front,(c)RMS error

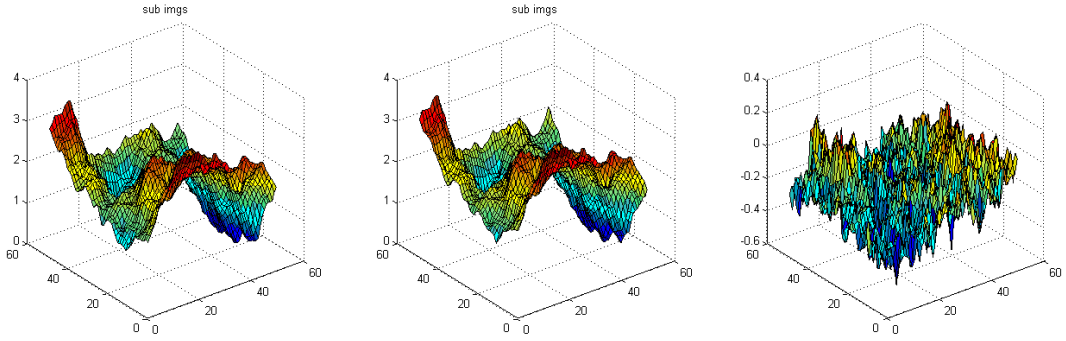

Sub-frame 3: (a) input wave-front,(b) output wave-front,(c)RMS error

Figure 6. 3: A snapshot of wave-front sensing of dynamic phase screen. (a) Dynamic phase, (b)Single frame input, (c) Output wave-front, (d) RMS wave-front error

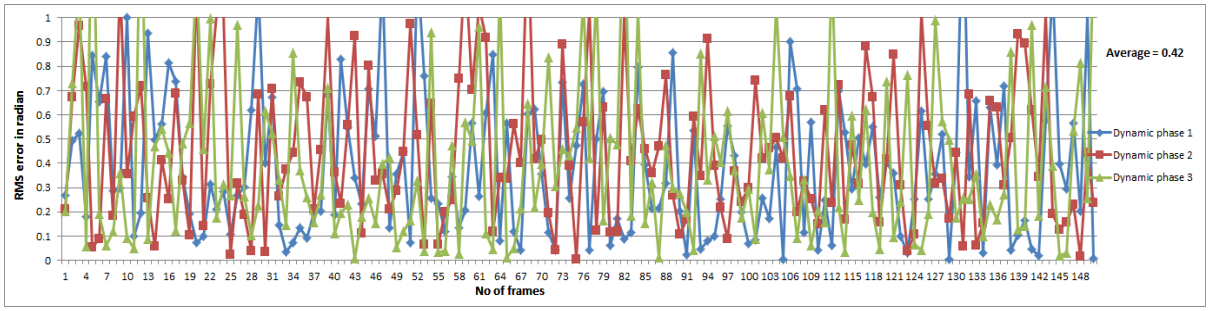

Figure 6. 4: RMS wave-front errors between input and output wave-fronts for different dynamic phase screen

6.2 Atmospheric turbulence simulator

Atmospheric turbulence simulator consists of random phase plate with a motorized mount. Random phase plates are optical component that change the phase of an incident beam in a stochastic fashion but do not appreciably absorb energy. Several phase plate design approaches have been reported including those based on glass etching, photolithography [13]. Characterization of laboratory generated turbulence is generally based on wave-front sensing that measure phase distribution of a wave-front or by measuring the angle-of arrival fluctuations.

The random phase plate is made by a near-index-matching (NIM) approach. After comparing the cost and spectral characteristics of the available techniques, this approach appears to be an excellent choice. Although active devices such as SLM and DM are being used to generate atmosphere like turbulence in laboratory, but have certain limitations. The advantage of these devices over active devices are that they do not generate much heat, can be compact, the exact shape of the turbulence can be determined rapidly and turbulence sequence can be repeated. Once phase plate is fabricated, a motorized assembly can be used to rotate the plate across a light path to

simulate temporal evolution of the turbulence. Furthermore, the resolution of static phase plates is much better than the active devices.

6.3 Principle of Near-Index-Match

The principle behind the NIM optics is illustrated in Figure 6.5. Two different materials with similar but unequal refractive indices η_1 and η_2 form a sandwich with the interfacial surface profile $h(x)$. If the exterior surface of both materials are planer, then the optical path difference (OPD) impressed upon a plane wave incident on the phase plate is given by

$$\begin{aligned} \mathrm{OPD}(x) &= h(x)\ [\ \eta_1(\lambda) - \eta_2(\lambda)\ ] \\ &= h(x)\,\Delta\eta(\lambda) \end{aligned} \qquad (67)$$

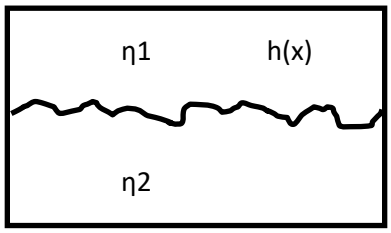

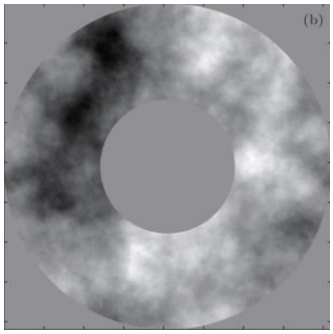

Figure 6. 5: Schematic diagram of a phase plate consisting of a sandwich of two materials (a) NIM principle, (b) Encoded phase in random phase plate

The pseudo random phase screen, made by Lexitek, used in this experiment has a flat transmission profile in the wavelength region 400-1600 nm. Its optical path difference is defined over an annular region of 4096 × 4096 array. The phase map was made with a Near-Index-Match^{TM} optic. The OPD, with a plane wave-front on the phase plate, is given by the difference of refractive indices $\Delta\eta$. Atmospheric turbulence induced variations in OPD are in few microns peak-to-valley. When two plates are chosen for which $\Delta\eta \approx 0.02$ the scale of OPD variations that can be produced is 5μm, at a wave-

length of 633nm. The $\frac{D}{r_0}$ corresponding to 5μm OPD is 15 which imply that the value of Fried's parameter is 400μm in a beam of diameter 0.5mm.

The phase profile of the encoded information in random phase plate is shown in Figure 6.6

Glass	**BK7 window**
Diameter	**100 mm, 83 mm active area**
Thickness	**22mm**
Phase matrix	**4096 x 4096 array**
Pitch	**20 μm phase grid**
Surface flatness	**λ/10 external surface**
OPD range	**5-30 μm**
Δη	**0.01 – 0.05**
Coating	**Broadband AR**
Spectral band	**400 – 1600 nm**

Table 5: Lexitek Phase plate specification

Figure 6. 6 : Phase plate with its specification

Initially the Kolomogorv model of phase screen has been simulated, with $\frac{D}{r_0}$ of 15 at 633 nm which gives peak-to-valley of 5μm. Hence the phase map design of the phase plate is assumed to follow Kolmogorov model of atmospheric turbulence.

6.4 Experimental setup for phase plate calibration

A 15 mW He-Ne laser with a wavelength of λ=632.8 nm is used as a source of light. A continuously variable Neutral Density Filter (NDF) is used to control the light intensity. The laser beam is spatially filtered using a 40x objective lens and 5 µm pinhole to remove the laser speckle noise. The spatially filtered beam is collimated using a doublet lens D1 of focal length f = 25 cm. The collimated beam is phase distorted by passing through the phase plate and is sensed using SHWS by using two more doublet lens D2 and D3 which are in 4f geometry. The phase plate is the object plane of the 4f geometry and the sCMOS camera is the image plane. The distorted beam passes through SHS before it is imaged on sCMOS camera which is placed at the image plane [14]. The imaging camera is a high resolution and low noise sCMOS camera from Photonic Science having sensor size 1920 x 1080 with a pixel size of 6.5 µm. The SHS used in this experiment has 100x100 sub-apertures having equal diameter and pitch of 150 µm. The focal length of SHS is 10 mm and the f-number is 66.7. The full-width half maximum (FWHM) spot size covers approximately 5x5 pixels on the detector.

The phase plate has 2-axis stepper motor control 12.5 - 25,000 pps each axis. The micro-stepping is 400 step (0.9° per step). The Fried's parameter of the phase plate is 400µm at a wavelength of 633 nm [15]. The phase map design of the phase plate assumes the Kolmogorov model of atmospheric turbulence. The optical beam size is 5 × 5 mm^2. Hence, the active detector area is 762 x 762 pixels. Only a small portion of the phase screen is seen by the SHWS at a given instant. This corresponds to a smaller portion of the microlens array of 33 × 33 lenses. The experimental setup is as shown in Figure 6.7.

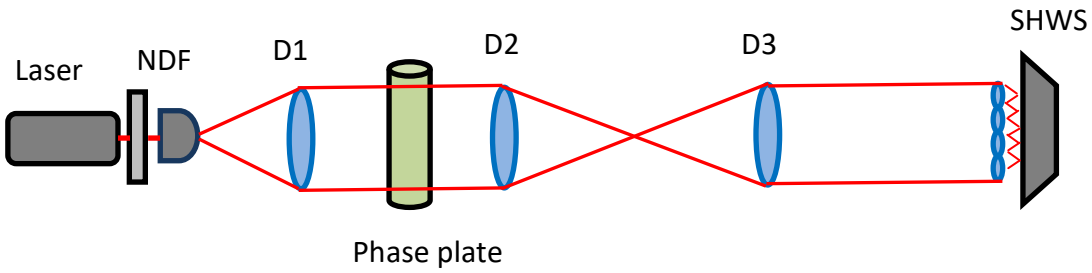

Figure 6. 7: Schematic setup for the experiment measurement of phase plate.

The sCMOS frames are acquired as matrices using the Matlab image acquisition toolbox in real-time. A background image (BKD) is taken without the microlens array and the phase plate as a reference. A reference pattern (REF) is taken by placing the mircolens array in front of the sCMOS without phase plate being in the beam path. The shifted spot pattern (SP) is recorded in the presence of phase plate in the beam path. Each of the matrices BKD, REF and SP are of size 762x762, since the SHWS sensor with 32x32 sub-apertures is used and each sub-aperture corresponds to 24x24 pixels on the sCMOS. BKD is subtracted from REF and SP [16]. Centre of gravity (CoG) centroiding method is used on the resulting spot pattern images and the local wave-front tilts are determined. This is the simplest of all the centroiding technique and is best suited for high light intensity level and good signal-to- noise ratio (SNR) with spots assumed to be Gaussian pattern. The wave-front are reconstructed using Fried's geometry with vector multiplication method (VMM). The comparative performance of different geometries with various reconstruction methods has been done initially for wavefront reconstruction.

6.5 Phase plate speed calibration

The dynamic behaviour of atmospheric turbulence is realized in the laboratory by using a phase plate. The experimental conditions correspond to a single layer atmospheric turbulence model with a fixed wind speed. The phase plate is mounted on

a rotary stage assembly. Rotation of the phase plate is steered by a stepper motor which is regulated by a Lexitek stepper controller. The controller which is capable of standalone operation, is used for changing the rotation speed. The move speed command (MVS) sets the phase plate to rotate. MVS values are quantized in multiples of 12.5, 25, 50, or 100 pulses per second (pps). A simple calibration procedure is carried out to measure the speed of the phase plate and test its linearity with changing move speed (MVS). Time taken for a single rotation of the phase plate is measured for different rotation speeds starting from 12.5 pps to 600 pps is given in Table 5.

MVS	Time in sec for one rotation	Speed in (mm/s)	Effective translation velocity(m/s)
12.5	767.98	0.245	0.122
25	384.44	0.49	0.245
37.5	255.97	0.736	0.368
50	191.51	0.984	0.492
62.5	153.61	1.226	0.613
75	127.83	1.474	0.737
87.5	109.83	1.716	0.858
100	95.88	1.965	0.982
112.5	85.47	2.204	1.102
125	77.31	2.437	1.218
137.5	69.63	2.706	1.353
150	63.91	2.948	1.474
162.5	59.18	3.1851	1.592
175	54.95	3.4301	1.715
187.5	51.29	3.6751	1.835
200	47.88	3.9201	1.961
300	32.15	5.8801	2.94
400	24.01	7.8401	3.96
500	19.23	9.8001	4.91
600	16.02	11.7601	5.88

Table 6: Speed measurement of the rotary stage motion

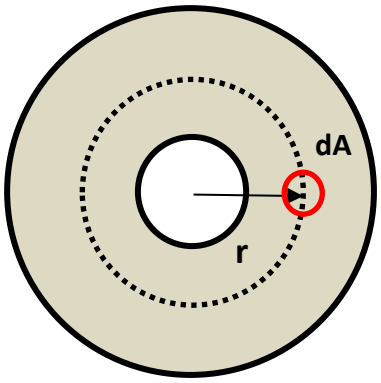

Figure 6. 8: Small area approximation: Distance travelled in one rotation is equal to the perimeter of the dotted circle

The phase plate has an annular region as shown in Figure 6.8. The beam which crosses the phase plate occupies a small area dA = 5 mm^2 as seen in Figure 6.8. The approximation is that the distance moved by the dA in a single rotation is equal to the perimeter of the dotted circle. The radius **r** that is equal to the length of the line joining the center of the phase plate and the center of the dA. In this case of phase plate, **r** =30 mm and hence a one rotation distance of 188.4 mm. The time taken for a single rotation is measured for various MVS. Hence, the speed of movement of the phase screen is calculated for all MVS.

6.6 Scaling up to the actual dimension

It is important to scale the simulated turbulence which is generated using a phase plate to actual turbulence at IAO. The rms seeing condition (r_0) of IAO Hanle is 13.7 cm at 500 nm. r_0 at 633 nm is 20 cm since it follows power of $\lambda^{\frac{6}{5}}$ with wavelength. r_0 of phase plate is 400 μm. Hence, the beam downscaling of 500:1 in the experiment by comparing the two values of r_0. The ROI of the detector is of the size 5x5 mm^2 and the same is used for experiments. This is equivalent to 2.5 m diameter of telescope.

Last column of Table 5 gives the effective translation velocity of the phase plate corresponding to wind velocity is given for each MVS speed. From Table 5, it can be seen that with MVS = 400, the effective translation velocity of the phase plate across the detector is 7.84 mm/s which corresponds to 3.96 m/s of wind velocity. For MVS = 12.5, minimum speed is 1.2 cm/s. Beyond MVS 400, the correlation coefficient between frames rapidly falls to zero. Hence, beyond MVS 400, due to the high speed of phase plate, wave-front reconstruction is almost impossible. Figure 6.9 shows snapshot of SH-spots with MVS 25, MVS 300 and MVS 500. Higher order aberrations are averaged out due to higher rotation speed of the phase plate and lower frame rate of camera. This results in presence of lower order aberration only.

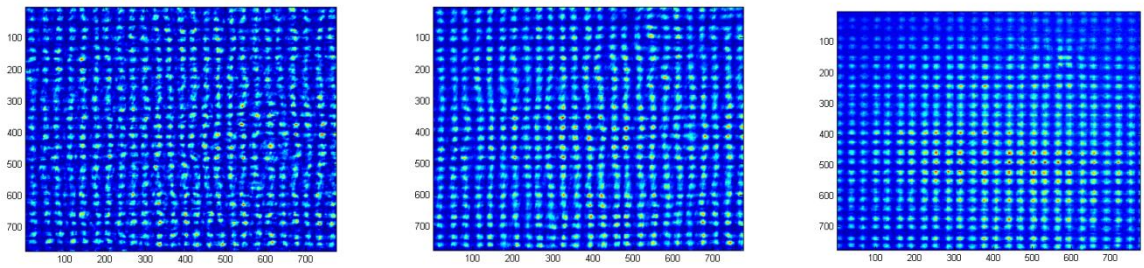

Figure 6. 9: SH-spot pattern of (a)MVS 25, (b) MVS 300 and (c)MVS 500

6.7 Phase plate to SHWS compatibility

The collimated beam from D1 passes through the rotating phase plate. The experiment uses a 4f geometry in which the phase plate is located at object plane and the sCMOS camera at the image plane. The wave-front sensing experiment is carried out in such a way that the SHWS and the wave-front sensing algorithm can efficiently detect the distortions introduced by the phase plate. The phase plate has a coherence length of (r_0 , Fried's parameter) 400 µm. SHWS used in this experiment has a pitch of

150 µm. Hence, the spatial sampling of the wave-front has done at double the spatial frequency of phase plate distortions.

The sCMOS camera acquires each SH spot with an exposure time of 150 ms. A sequence of 30 images are captured for a given MVS of the phase plate. The frames are of size of 762 x 762 pixels covering 32 x 32 SH spots. By using CoG method, the difference in the centroid locations of the spot pattern and reference spot pattern is determined. Fried's geometry gives the local slopes of the distorted wave-front across each microlens of the lenslet array. The wave-front is reconstructed from the local slopes of the wave-front sensor. Iterative least square method used for wave-front reconstruction. The reconstructed wave-front phase maps are 33 × 33 in sized matrices. Bilinear interpolation is used to re-size these phase maps to 100 × 100 matrices for each distorted frame captured by the sCMOS camera.

The correlation coefficient C^1_k is determined between time evolving reconstructed wave-fronts [17].

$$C_k^1 = \frac{E[(A^1 - \mu^1)(A_k - \mu_k)]}{\sigma^1 \sigma^k} \tag{68}$$

where, 'μ' stands for mean and 'σ' stands for standard deviation. 'k' represents the time index which lies between $1 \leq k \leq 30$. '1' in the superscript suggests that the first wave-front is compared with the subsequent wave-front in the time sequence.

For MVS = 50, a sequence of 30 frames are taken. The temporal correlation coefficients between first reconstructed wavefront and subsequent wave-front for MVS 50 are determined. Its repeated multiple times to check any error budget. The correlation coefficient between the 1st reconstructed wavefront and 30th reconstructed wavefront reduces to 0.3. Same steps are repeated for MVS = 100. In this case, its correlation coefficient falls to 0.2 since MVS 100 revolves at a faster rate compared to MVS 50 and it sweeps a greater area across the annular region of the phase plate. Figure 6.10 & 6.11 shows a comparison of the temporal correlation coefficient for MVS 50 & 100.

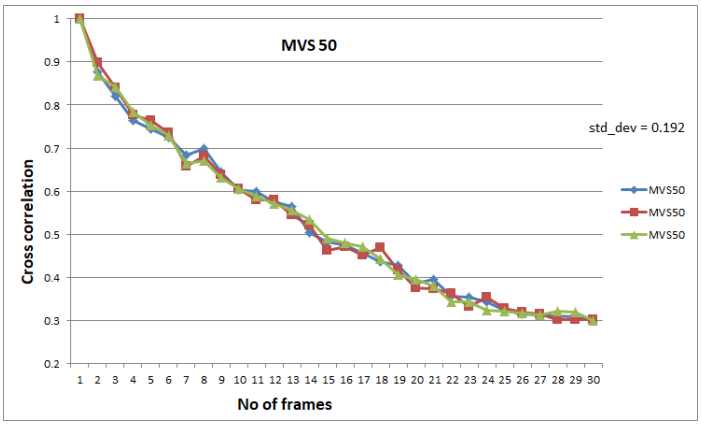

Figure 6. 10: Correlation coefficients between reconstructed wave-fronts at MVS=50

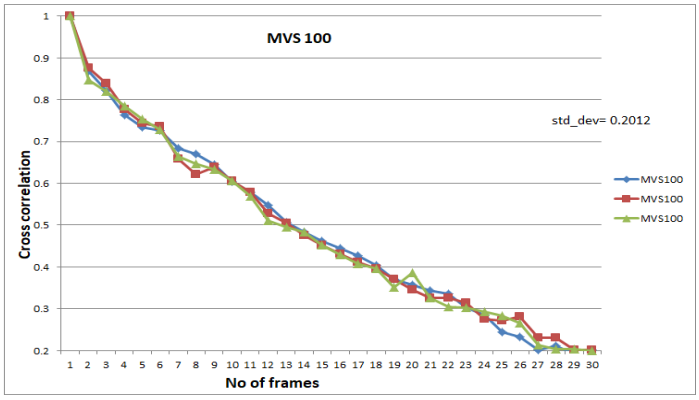

Figure 6. 11: Correlation coefficients between reconstructed wave-fronts at MVS=100

Experiments are carried out for all MVS between 25 to 400 with a step size of 12.5. The cross correlation coefficients between 1st frame and its subsequent frames are determined. Figure 6.11 shows the cross correlation coefficients and number of frames for selected number of MVS.

Figure 6.12 shows a comparison of the temporal correlation coefficient for different MVS. The temporal correlation coefficient decays slowly in the case of MVS = 25 and very fast in the case of MVS = 400. Since, as the speed of the phase plate increases the area occupied in the annular region increases by the beam in a specific time. Also, it

should be noted that the decay rate of the temporal correlation coefficient increases with increasing move speed.

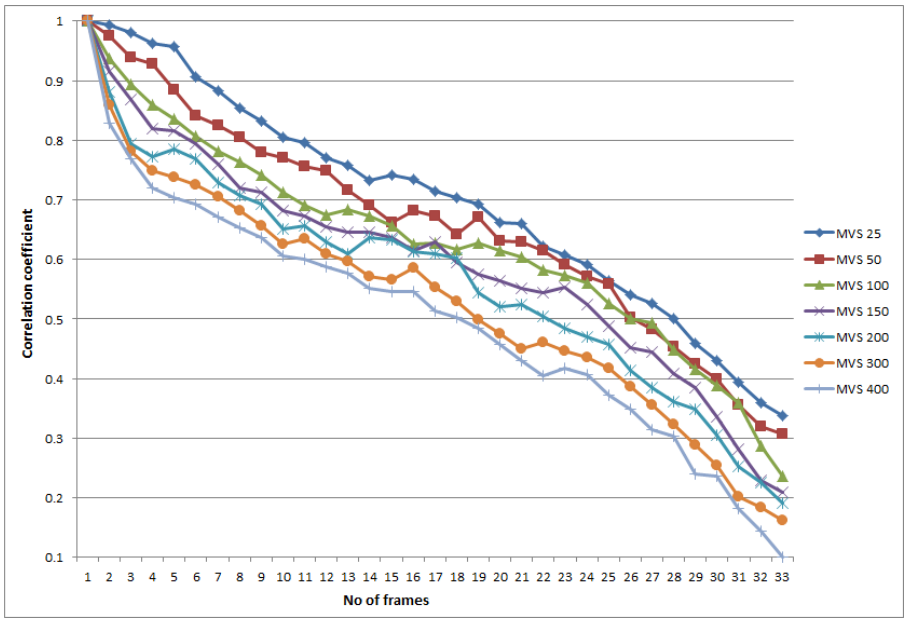

Figure 6. 12: Correlation coefficients between different frames for various MVS speed

6.8 Varying exposure time of the sCMOS

Wind speeds are estimated with a constant exposure time within the MVS range of 25 to 400. By varying the exposure time of the sCMOS camera, the range of exposure times where wind speed can be measured is estimated. The imaging camera is a high resolution low noise sCMOS camera from Photonic Science having sensor size of 1920 x 1080 with each pixel of size 6.5 x 6.5 μm^2. The experiment is carried out in a dark room keeping the thermal noise at minimal. The camera features high-speed read-out of the sCMOS sensor at 50 MHz. In most applications 50 MHz is the best choice as it gives slightly lower readout noise. This results in a maximum frame rate of approximately 16 fps at 50 MHz with readout noise as low as 1.2e-. Due to Peltier cooling of the sensor, very long exposures are also possible with the camera, to allow the imaging of very faint signals. A short exposure time of 10ms is taken for SH spots.

Reconstruction of wave-front becomes difficult below 10 ms due to the dominance of photon shot noise. At first, a sequence of SH-spots with different exposure times starting from 10 ms to 500 ms with an interval of 30 ms are taken as beyond 500 ms detector goes into saturation. Average value of SNR are determined for each frame. The relation between average SNR of SH-spots with their corresponding exposure time is determined as shown in Figure 6.13, which shows there exists a square relationship between SNR of SH-spots and exposure time.

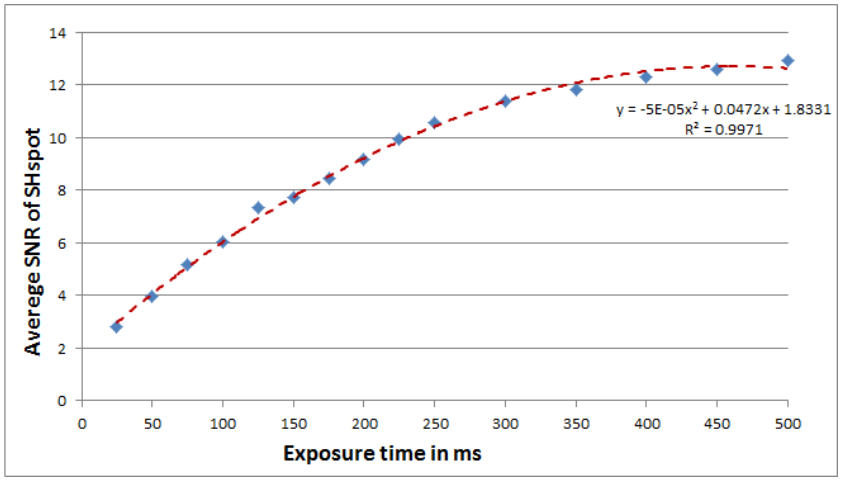

Figure 6. 13: Square relation between exposure time and SNR of SHspot

A sequence of 20 SH-spots with different exposure time starting from 10 ms to 500 ms with an interval of 30 ms are taken for MVS 50. The corresponding SNR values for the above mentioned exposure times are determined. The correlation coefficients between 1st frame and subsequent frames are determined for all these SNR values. Figure 6.14. shows the relation between cross correlation coefficients and number of frames for selected value of SNR.

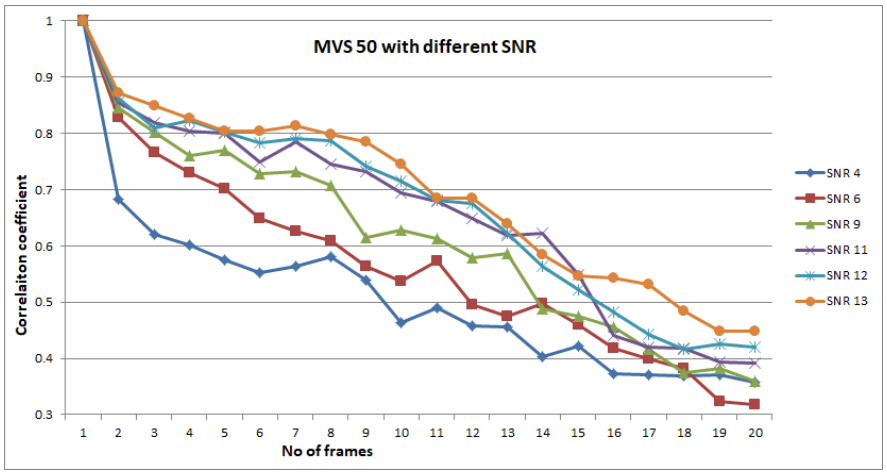

Figure 6. 14: Correlation coefficient between frames at MVS=50 with increasing exposure time

It is seen that for low values of SNR the curve decays quickly leading to low correlation coefficients that's why it's difficult to detect centroid to reconstruct the wave-front. However as the SNR value increases the correlation between 1st and subsequent frames increases.

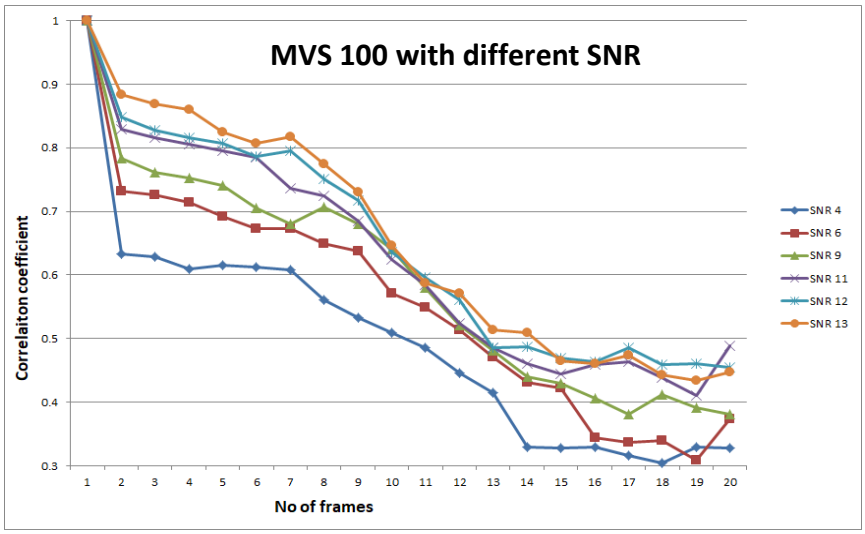

Figure 6. 15: Correlation coefficient between frames at MVS=100 with increasing exposure time

Another sequence of 20 frames are taken for MVS 100 with different exposure times starting from 10ms to 600 ms at an interval of 30 ms. The correlation coefficients between 1st frame and subsequent frames are determined for different exposure times. It has been seen that the decay of the above shown curve is quick for low exposure frames compared to higher exposure frames. Therefore the same kind of decay in the curve between correlation coefficient and number of frames has been observed for both MVS 50 as well as MVS 100.

By keeping exposure time at 50 ms i.e at a SNR value of 4, a sequence of 20 frames is taken with different MVS speeds of phase plate. Correlation coefficient between 1st frame with subsequent frames are found out for all MVS speeds of the phase plate. Figure 6.16 shows the plot between correlation coefficients and number of frames with different MVS of phase plate at 50 ms exposure time. It has been observed that as the MVS speed of the phase plate increases the decay of the curve also increases. For lower speed of phase plate correlation is better compare to higher speed at 50 ms exposure time.

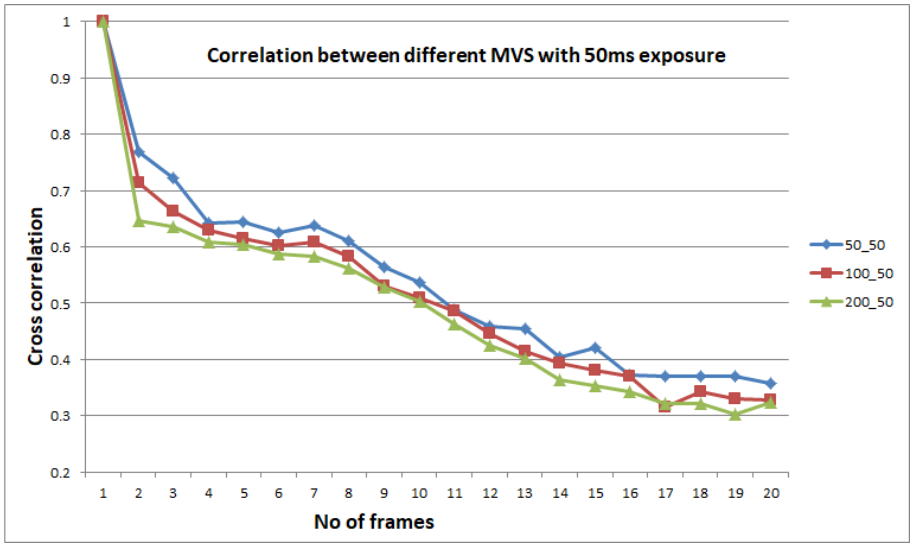

Figure 6. 16:Correlation coefficient between frames at exposure of time 50ms with different MVS of phase plate.

Same procedure is repeated for higher exposure time of 500 ms (SNR 13) with different MVS of phase plate. A sequence of 20 frames are taken with different MVS. Figure 6.17 Correlation coefficient between 1st frame and subsequent frames for selected MVS. With increasing MVS speed of the phase plate the decay of the curve decreases. For higher MVS speed correlation is better compare to lower MVS speed at high exposure time.

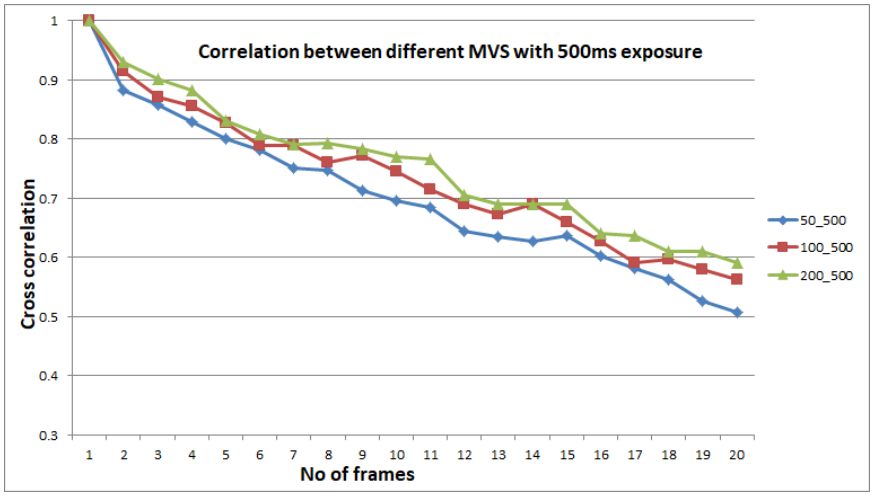

Figure 6. 17:Correlation coefficient between frames at exposure time 500ms with different MVS of phase plate.

In order to determine the range of SNR value where wave-front is effectively reconstructed with different MVS speed, a plot between SNR with cross correlation coefficients of wave-front for various MVS speeds are plotted. Figure 6.18 shows the relation between various SNR and correlation coefficients for selected MVS speeds of the phase plate.

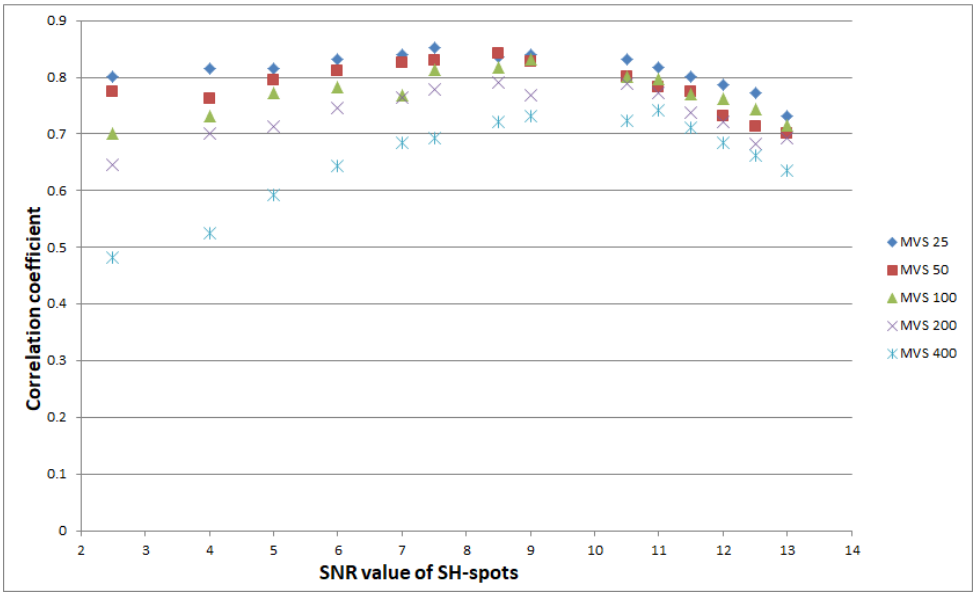

Figure 6. 18: Relation between correlation coefficient and exposure times with MVS.

From Figure 6.18, it can be concluded that below SNR of 5 the correlation coefficients between frames are low due to the dominance of photon noise in low exposure time. As the speed of MVS increases in this range, the slope of the correlation coefficient vs SNR curve further increases. Correlation coefficients also decreases gradually for all MVS in the range of 25 to 400pps when SNR value is above 11. Wave-front reconstruction is difficult at high exposure time as the centroiding technique are not accurate. It can be seen that correlation coefficients between frames are good between exposure time of 100ms to 400ms. as the SNR values are good.

6.9 Conclusions

In this chapter, a small portion from a large wave-front is selected as the initial phase screen in the temporal evolution of a single layer. Wave-fronts are reconstructed dynamically and its correlation coefficients are found with input wave-fronts. The average correlation coefficients between input and output wave-fronts are in the range of 0.6-0.8. The average value of RMS wave-front errors is 0.42 radian found out dynamically between input and output wave-fronts. Using phase plate the maximum speed at which wave-fronts can be reconstructed is found to be MVS 400. Which is equivalent to 5 m/s wind speed at IAO Hanle and minimum speed at MVS 25 is 1.22 cm/s.

Bibliography

[1] J. W. Hardy, Adaptive optics for astronomical telescopes, Newyork: Oxford University Press, New York, 1998.

[2] M. Hart, "“Recent advances in astronomical adaptive optics,”," *Appl. Optics,* vol. 49, p. D17–D29, 2010.

[3] M. C. Roggemann and B. Welse, Imaging through turbulence, New york: CRC press, 1996.

[4] T. Fusco, "“Naos on-line characterization of turbulence parameters and adaptive optics performance,”," *Journal of Optics A: Pure and Applied Optics 6,,* vol. 12, p. 585–596(12), (June 2004)..

[5] B. L. Ellerbroek, "“First-order performance evaluation of adaptive-optics systems for atmospheric-turbulence compensation in extended-field-of-view astronomical telescopes,”," *J. Opt. Soc. Am,* vol. A 11(2), pp. 783-805, 1994.

[6] J. W. Hardy, Adaptive Optics for Astronomical Telescopes, New York: Oxford University Press, New York , (1998).

[7] R. Racine, "Temporal fluctuations of atmospheric seeing," *Publications of the Astronomical Society of the Pacific,* vol. 108, p. 372–374, (1996)..

[8] J. Vernin and . C. Muoz-Tun,, "“The temporal behaviour of seeing,”," *New Astronomy Reviews,* vol. 42, no. (6-8), pp. 451-454, 1998.

[9] B. Garca-Lorenzo, A. Eff-Darwich, J. J. Fuensalida and J. Castro-Almazn, "“Adaptive opticsparameters connection to wind speed at the teide observatory"," *Monthly Notices of the Royal Astronomical Society*, vol. 397(3), p. 1633–1646, (2009).

[10] A. Rocca , F. Roddier and J. Vernin, "Detection of atmospheric turbulent layers by spatiotemporal and spatioangular correlation measurements of stellar-light scintillation,"

J. Opt. Soc. Am, vol. 64(7), pp. 1000-1004, 1974.

[11] R. G. Lane, A. Glindermann and J. C. Dainty, ""Simulation of a kolmogorov phase screen"," *Waves in Random Media,* vol. 2(3), p. 209–224, (1992).

[12] G. Sedmak, "“Performance analysis of and compensation for aspect-ratio effects of fast-fourier-transform transformbased"," *Appl. Opt.,* vol. 37(21), p. 4605–4613, (1998).

[13] "“Low-cost broadband static phase for generating atmospheric like turbulence"," *Appl. optics,* vol. 40, pp. pp. 2946-2955, 2001.

[14] M. B. Roopashree, V. Ankodi and B. . R. Prasad, ""A Novel Model of Influence Function: Calibration of a Continuous Membrane Deformable Mirror,"," *ACEEE Int. J. on Control System and Instrumentation,* Vols. vol. 03,, no. no. 02,, 2012.

[15] M. B. Roopashree, V. Ankodi and B. . R. Prasad, ""Wind speed measurement from Shack Hartmann Wavefront Sensor data: An experimental review of cross-correlation peak detection,"," *Int. J. on Recent Trends in Engineering and Technology,* vol. vol. 6, no. no. 2,, 2011.

[16] A. Vyas, M. B. Roopashree and B. R. Prasad, ""Intensity Weighted Noise Reduction in MEMS Based Deformable Mirror Images,"," in *AIP Conf Proceeding,* 2011.

[17] T. I. Wang, G. R. Ochs and R. S. Lawrence, "Wind measurements by the temporal cross-correlation of the optical scintillations," *Appl. Opt,* vol. 20, no. 23, pp. 4073-4081, december 1981.

Chapter 7

CONTROL TECHNIQUES OF ADAPTIVE OPTICS SYSTEM

The input and the output of a closed-loop system are the wave front phase perturbations and the residual phase after correction. The design and the optimization of an AOS is a complex problem. It involves many scientific and engineering topics, such as understanding of atmospheric turbulence, image formation through turbulence, optics, mechanics, electronics, real time computers, and control theory. The goal of this chapter is to provide the basis of spatial and temporal controls.In first part, the control matrix determination and the modal control analysis of an AOS are described. Then the AOS temporal behaviour is described by means of a transfer function representation. The AOS closed-loop optimization is discussed. Finally, general considerations on the RTC are given.

7.1 Adaptive Optics system: a servo loop

An adaptive optics system (AOS) contains three key components, the wave-front sensors (WFS), the wave-front corrector (WFC) and the real time computer (RTC). The goal of this system is to compensate for an incoming wave-front distorted by atmospheric turbulence. It is designed to minimize the residual phase variance in the imaging path, i.e. to improve the overall telescope point-spread function (PSF). The wave-front, after being aberrated by atmospheric turbulence, passes through reflective telescope and instrumentation optics. Each optical surface will contribute to the total wave-front aberration. The wave-front is reflected through the WFC. Part of the light enters the scientific instrument, commonly either an imager or spectrograph, whereas the other portion enters the WFS. The wave-front is measured and data electronically

processed by the RTC, which calculates and generates signals used to apply the phase conjugate to the corrector [1] [2].

Figure 7.1 gives a schematic view of an AOS, using classical block diagram representation, with the control computer (CC), the digital to analog converters (DAC), and the high voltage amplifiers (HVA). As shown, the input of this servo is the uncompensated wave front, whose value at a point (x, y) and at a time t is denoted by $\varphi_{tur}(x,y,t)$. The correction introduced by the DM is denoted by $\varphi_{corr}(x,y,t)$. $\varphi_{res}(x,y,t)$ is the value of the residual phase after correction, so that

$$\varphi_{res}(x,y,t) = \varphi_{tur}(x,y,t) - \varphi_{corr}(x,y,t)$$

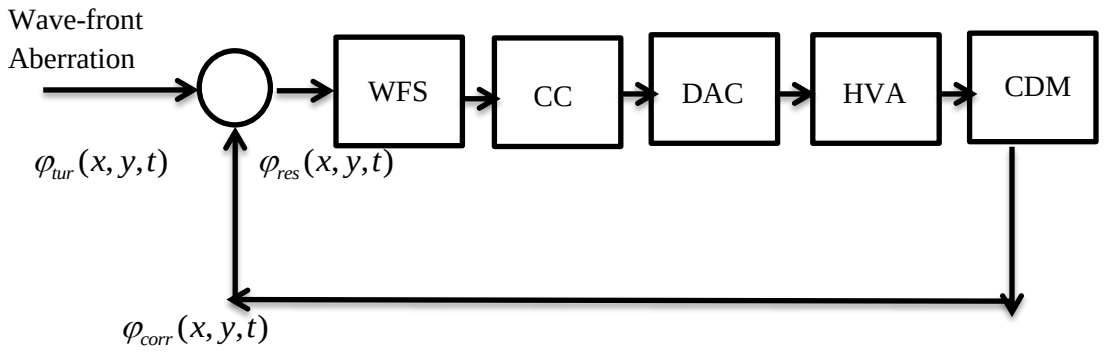

Figure 7. 1: Closed-loop control system for correcting the wave aberration

In closed-loop operation, the AOS minimizes $\varphi_{res}(x,y,t)$ with the finite spatial and temporal resolution given by the local measurements of the wave-front. To achieve this minimization, the WFS must be placed in the optical path after the DM in such a way it measures $\varphi_{res}(x,y,t)$. The WFS spatial resolution is given by its number of useful sub-apertures. Its temporal resolution is determined by the sampling frequency of its detector, which is generally set by the exposure time T [3] [4].

The WFS measurements φ_{res} is represented by '*S*' which is called the measurement vector. This is an *m*-dimensional vector where *m* is the number of WFS measurements. The control voltages to be applied to the DM are deduced from '*S*'. They can be described by a vector called the control vector, and denoted by '*V*'. This is an *n*-dimensional vector, where *n* is the number of DM actuators. When applied to the DM, these voltages control the shape of its reflecting surface, described by the corrected phase φ_{corr}. It could be noticed that the control of the DM from the WFS measurements is a physical way to reconstruct a wave front. In an AOS, the control voltages are determined from the WFS measurements through a control law which can be split into two parts: a static part, which mainly deals with the reconstruction of the WFS measurements on the basis of the DM actuators, and a dynamic part which ensures the stability and the accuracy of the closed loop. The first part, the static part, estimates the control vector '*V*' containing the control voltages that, if they were sent to the DM, would give the best fit of the WFS measurements '*S*'. This estimation is performed through the multiplication of '*S*' by a control matrix denoted by 'D^*'. The dynamic part evaluates the control vector '*V*' which will correct for φ_{corr}.

7.2 Control matrix determination

The control matrix *C* is used in the reconstruction operation, which takes a vector of WFS signals, *S* and produces a vector of actuator RTC signals V. This can be written as the matrix operation given in equation .The determination of this control matrix assumes that the AOS is a linear system. The control matrix *C* is inverse of influence matrix 'I' as shown in Equation 59.

$$V = CS \tag{69}$$

If there were the same number of signals as actuators, the inversion of I would be relatively easy, providing the square matrix isn't singular, which isn't normally the case. This leads to the most common method of reconstructing used in AO, the least squares.

$$V = [I^T I]^{-1} I^T S = CS \tag{70}$$

Thus the method of least squares has produced a new matrix called the pseudoinverse of ***I,*** this makes the control matrix *C*. where '^{T} ' is the transposition operator. Eq (6.7) shows that the control matrix C exists only if the square symmetric matrix $[I^T I]$ is invertible. $[I^T I]$ is a covariance matrix characterizing the coupling between the DM actuators through the WFS measurements. The diagonalization of this matrix provides a set of independent modes in the WFS space. They define an orthonormalized basis for the vector space of the DM actuators.

7.3 Adaptive optics temporal behaviour

Figure 6.1 gives a classical block-diagram representation of an AOS controlloop. The WFS gives measurements of the residual optical phase. Whatever the principle of the WFS, the associated detector integrates the photons coming from the guide star during a time T, then delivers an intensity measurement. The WFS measurements, derived from this analog signal, are then available only at sampling times whose period is T. Consequently an AOS is a servo using both continuous and sampled data.

The wave-front computer (WFC) derives the WFS measurements from the analog signal of the detector. The CC calculates the DM control voltages from the WFS measurements and DACs are used to drive the DM HVAs

7.3.1 Transfer Function of an Adaptive Optics System element

An AO system is a multiple input/output system in which the inputs are the control commands of the wave-front corrector and the outputs are the wave-front measurements from the wave-front sensor. With the appropriate choice of controller, the AO system's control loop can be split into multiple independent single servo systems. We can analyse the temporal behaviour of each system independently. Figure 7.2 shows a block diagram representation of an AO control system, in which $X(s)$ is the input wave aberration, $R(s)$ is the residual wave aberration, $N(s)$ is the noise from the wave-front sensor, and $M(s)$ is the control signal for wave-front compensation. To study the overall temporal behaviour of an AO system, a transfer function approach is used to model each of the components in the block diagram [5] [6].

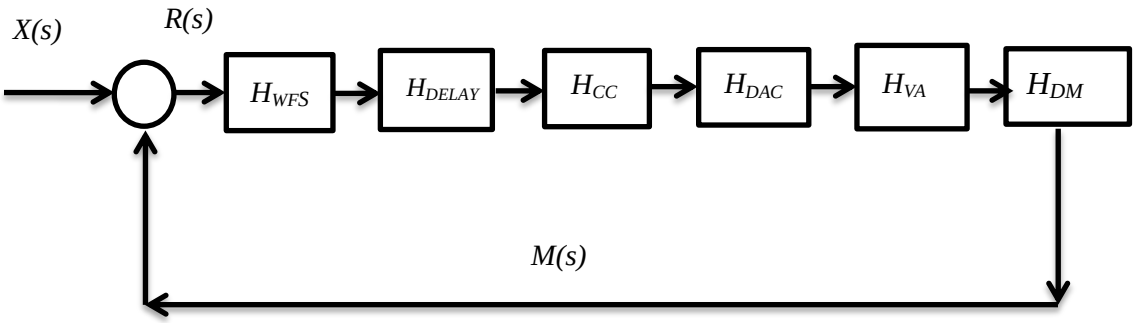

Figure 7. 2: **Block diagram of an adaptive optical control system for the eye.*T* = integration time; t = readout and computation delay time; WC = wavefront computer;CC = control computer; ZOH = zero-order hold; HVA = high-voltage amplifier s;DM = deformable mirror.**

7.3.1.1 Transfer Function of Wave-front Sensor, H_{WFS}

No matter what kind of principle the wavefront sensor uses it requires a detector to accumulate photons coming from the eye for measuring the wave aberration. The detector is characterized by its integration time, T (or exposure time). Then the transfer function of the wavefront sensor (WFS) is

$$H_{WFS}(s) = \frac{1 - e^{-Ts}}{Ts} \tag{71}$$

7.3.1.2 Transfer Function of Wave-front Sensor Computer Delay, H_{DELAY}

The temporal characteristic of the wave-front sensor computer is the time lag, τ, due to the readout of the detector and the computing of the wave-front measurements (such as the centroid calculation in the case of a Shack–Hartmann wave-front sensor), and the voltage deduced from the wave-front measurements.

$$H_{DELAY}(s) = e^{-\tau s} \tag{72}$$

7.3.1.3 Transfer Function of Computer control, H_{CC}

The main task of the control computer is to apply a control law to the voltages used for updating the wave-front corrector, allowing the AO system to perform the real-time compensation required to optimize the AO closed-loop response. Here we use HCC(s) to represent the temporal characteristic of the control computer

$$H_{CC}(s) = 1 \tag{73}$$

7.3.1.4 Transfer Function of Digital-to-Analog Converters, H_{DAC}

Digital-to-analog converters (DACs) convert the control voltage from a digital-to-analog signal for driving the wave-front corrector. A DAC usually holds the current control voltage during the exposure time until the next voltages are available from the control computer, so this transfer function is designated as the zero-order hold (ZOH). The transfer function can be written as:

$$H_{DAC}(s) = \frac{1 - e^{-\tau s}}{s} \tag{74}$$

7.3.1.5 Transfer Function of High-voltage amplifier, H_{VA}

The high-voltage amplifiers (HVAs) amplify the low control voltage from the DACs to drive the actuators of the wave-front corrector. Since the bandwidth of the HVAs is much greater than the sampling frequency of the AO system, we use a simple model for the transfer function of the HVAs:

$$H_{VA}(s) = 1 \tag{75}$$

7.3.1.6 Deformable Mirror, H_{DM}

Generally, the resonant frequency of the wave-front corrector is much greater than the sampling frequency of the wave-front detector. The transfer function of the DM can also be simply modelled as:

$$H_{DM}(s) = 1 \tag{76}$$

7.4.2 Overall adaptive optics system transfer function

Continuous Laplace models can be used to analyze the AO control system. Assuming the linearity of the system, its open-loop transfer function can be written as the overall product of the previously defined transfer functions. Figure 7.3 shows the block diagram of an AO control system modelled with transfer functions. The open-loop transfer function of the AO control loop is

$$H_{OPEN}(s) = \frac{M(s)}{R(s)} \tag{77}$$

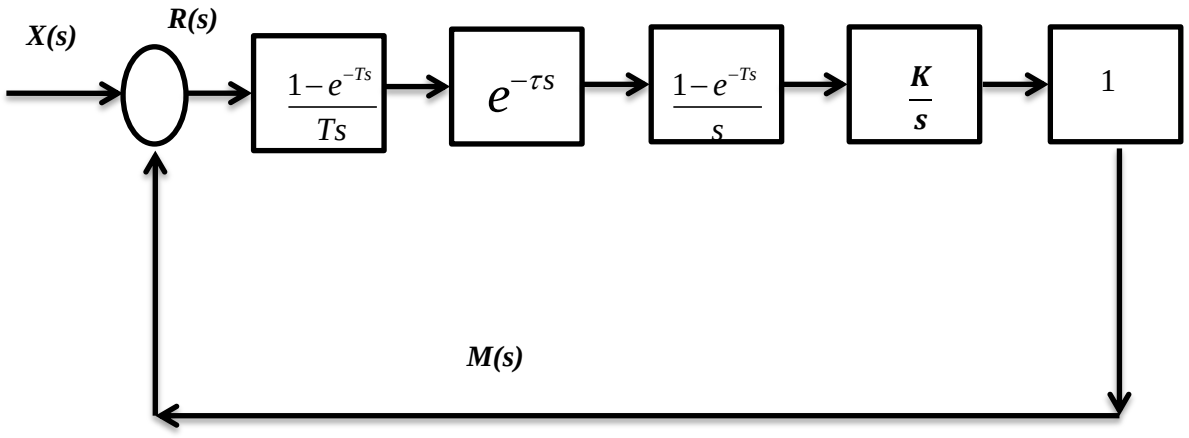

Figure 7. 3: Block diagram of the AO control system using transfer functions

And the closed-loop transfer function is is defined as the transfer function between the residual phase and the turbulent wave front fluctuations. It represents the ability of the AOS to compensate for phase perturbations as a function of frequency. It is the most important feature of such a servo since it characterizes its correction efficiency. It is related to the open-loop transfer function by

$$H_{CLOSED}(s) = \frac{M(s)}{X(s)} = \frac{H_{OPEN}(s)}{1 + H_{OPEN}(s)} \tag{78}$$

The error transfer function is

$$H_{ERROR}(s) = \frac{R(s)}{X(s)} = \frac{1}{1 + H_{OPEN}(s)} \tag{79}$$

From these three transfer functions, three criteria of control bandwidths are used when analyzing an AO control system .

1. *Open-Loop Bandwidth* The open-loop bandwidth is defined as the 0-dB cut-off frequency, f_{OPEN} of the open-loop transfer function:

$$\left|H_{OPEN}(i2\pi f_{OPEN})\right|^2 = 1 \tag{80}$$

2. *Closed-Loop Bandwidth* The closed-loop bandwidth, f_{3dB}, is the 3-dB closed-loop cut-off frequency of the closed-loop transfer function:

$$\left|H_{CLOSED}(i2\pi f_{3dB})\right|^2 = \frac{1}{2} \tag{81}$$

The closed-loop bandwidth determines the frequency range over which the controller rejects the temporal variations.

3. *Error Transfer Function Bandwidth* The error transfer function bandwidth, *fe*, is the 0-dB closed-loop error cut-off frequency of the error transfer function:

$$\left|H_{ERROR}(i2\pi f_e)\right|^2 = 1 \tag{82}$$

The error transfer function determines the frequencies over which the closed-loop system responds to the wave-front sensor measurement noise.

The theoretical transfer functions of an AO closed-loop system are now

$$H_{OPEN}(s) = \frac{M(s)}{R(s)} = K\frac{(1-e^{-Ts})^2 e^{-\tau s}}{Ts^3} \tag{83}$$

the closed-loop transfer function and error transfer function

$$H_{CLOSED}(s) = \frac{K(1-e^{-Ts})^2 e^{-\tau s}}{Ts^3 + K(1-e^{-Ts})^2 e^{-\tau s}} \tag{84}$$

$$H_{ERROR}(s) = \frac{Ts^3}{Ts^3 + K(1-e^{-Ts})^2 e^{-\tau s}} \tag{85}$$

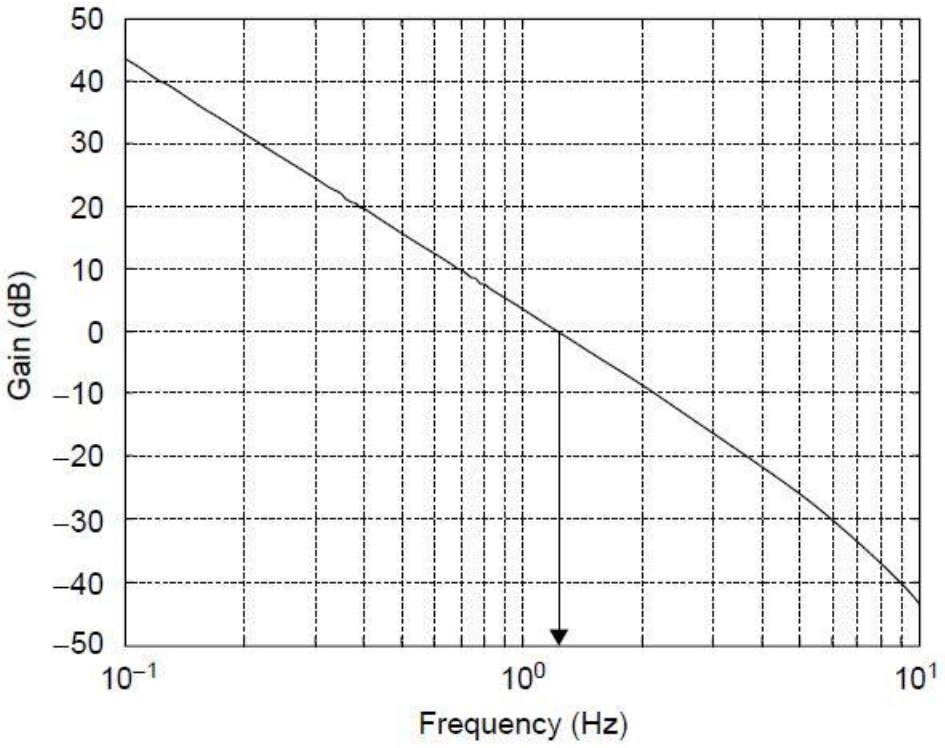

Figure 7. 4: Gain of the open-loop transfer function

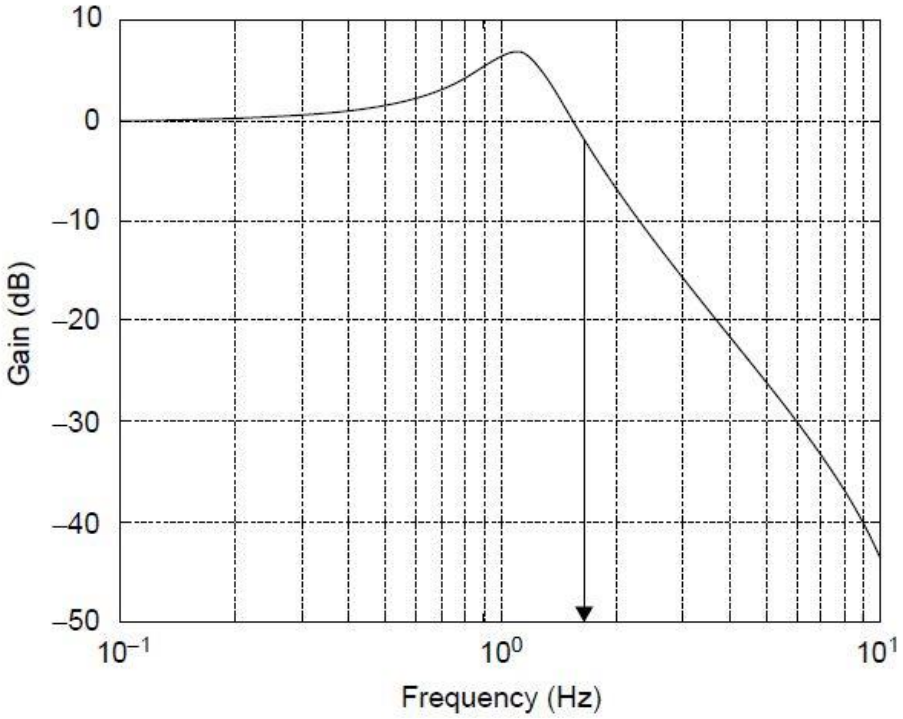

Figure 7. 5: Gain of the closed-loop transfer function

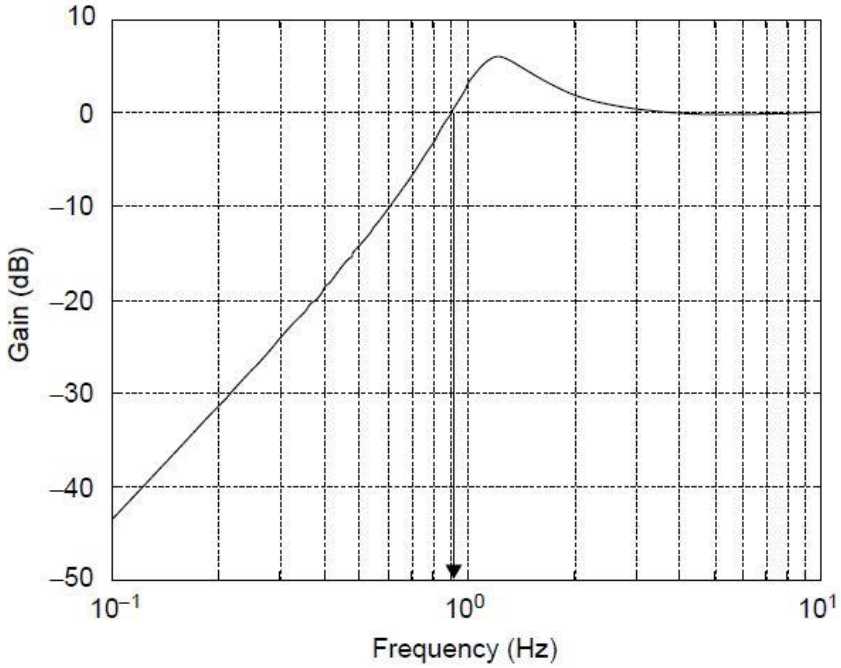

Figure 7. 6: Gain of the error transfer function

7.5 Conclusions

The gain of the open-loop transfer function H_{OPEN} of an AO system with a 30-Hz wave-front sensor sampling rate and time lag $\tau = T$. The open-loop bandwidth is 7.3 Hz with a feedback control loop gain of $K = 30$. Figure 6.5 is the gain of the closed-loop transfer function H_{CLOSED} with $K = 30$. The closed-loop bandwidth is 18 Hz. Figure 6.6 gives the gain of the error transfer function H_{ERROR} in which the bandwidth of the error transfer function is 6.9 Hz.

Bibliography

[1] G. F. Franklin , J. D. Powell and M. Workman, in *Digital Control of Dynamic Systems*, New York, Addison-Wesley, 1997.

[2] W. Jiang and X. Li, "Control Bandwidth Analysis of Adaptive Optical Systems in Adaptive Optics and Applications. Proceedings of SPIE," in *SPIE 3126: 447–454*, 1997.

[3] B. L. Ellerbroek and T. A. Rhoadarmer , "Optimizing the Performance of Closed-Loop Adaptive-Optics Control Systems on the Basis of Experimentally Measured Performance Data.," *J. Opt. Soc. America*, vol. 14, p. 1975–1987., 1997.

[4] C. Dessenne and T. A. Rhoadarmer , "Optimization of a Predictive Controller for Closed-Loop Adaptive Optics," *Appl. Optics*, vol. 37:, p. 4623–4633., 1998.

[5] J. P. Gafford, and . G. Ledanois, "Adaptive Optical Transfer Function Modeling," in *Proc. SPIE 1542*, 1991.

[6] J. P. Gafford and C. Boyer, "'Adaptive Optics: Effect of sampling rate and time lags on the closed-loop bandwidth'," in *Proc. SPIE 1271, p33-50,*, (1991)..